Measurement of the $D^{*\pm}$ Meson Production Cross Section at Low and Medium Q^2 with the H1 Detector at HERA

Dissertation

zur Erlangung des Doktorgrades

des Fachbereich Physik

der Universität Hamburg

vorgelegt von

Monica Dobre

aus Bukarest

Hamburg
2012

Gutachter der Dissertation:	Prof. Dr. Robert Klanner Dr. Katerina Lipka
Gutachter der Disputation:	Dr. Katerina Lipka Prof. Dr. Sven-Olaf Moch
Datum der Disputation:	19. November 2012
Vorsitzender des Prüfungsausschusses:	Dr. Georg Steinbrück
Vorsitzender des Promotionsausschusses:	Prof. Dr. Peter Hauschildt
Leiterin des Fachbereichs Physik:	Prof. Dr. Daniela Pfannkuche
Dekan der MIN Fakultät:	Prof. Dr. Heinrich Graener

Abstract

The inclusive production of $D^{\pm}(2010)$ mesons in deep inelastic scattering is studied using data recorded by the H1 experiment in the years 1999 to 2000 and corresponding to an integrated luminosity of 47.66 pb^{-1}. The measurement covers the region $2 < Q^2 < 100$ GeV^2 in photon virtuality and the region $0.02 < y < 0.7$ in the inelasticity of the scattering process. The visible range of the $D^{*\pm}$ meson production is restricted in transverse momentum to $p_T(D^*) > 1.25$ GeV and in pseudorapidity to $|\eta(D^*)| < 1.8$. Single and double differential cross sections are compared to leading order and next-to-leading order perturbative QCD predictions.

Zusammenfassung

Es wird der inklusive Erzeugungswirkungsquerschnitt von $D^{*\pm}(2010)$ Mesonen in tief-unelastischer *ep*-Streuung gemessen. Hierzu werden Daten ausgewertet, die vom H1-Experiment in den Jahren 1999 bis 2000 entsprechend einer integrierten Luminosität von 47.66 pb^{-1} aufgezeichnet wurden. Die Messung findet in einem kinematischen Bereich statt, der durch die Virtualität des Photon $2 < Q^2 < 100$ GeV^2 und die Unelastizität $0.02 < y < 0.7$ definiert ist. Der sichtbarer Bereich für $D^{*\pm}$ Meson Erzeugung ist durch den transversalen Impuls $p_{\perp}(D^*) > 1.25$ GeV und die Pseudorapidität $|\eta(D^*)| < 1.8$ gegeben. Die einfach und doppelt differentiell gemessenen inklusive Wirkungsquerschnitte werden verglichen mit Vorhersagen der perturbative Quantenchromodynamik in führender und nächstführender Ordnung.

Contents

Introduction **1**

1 Open Charm Production in DIS **3**
1.1 Electron-Proton Scattering and the Quark Parton Model 4
1.1.1 The Kinematics of the Deep Inelastic Scattering 4
1.1.2 The Parton Model and the Inclusive DIS Cross Section 6
1.2 The DIS Formalism in Quantum Chromodynamics 7
1.2.1 Renormalization and the Running of the Strong Coupling Constant 8
1.2.2 Scaling Violations in QCD 10
1.2.3 QCD Factorization 10
1.2.4 Parton Evolution Models 11
1.3 Heavy Quark Production in ep Scattering 16
1.3.1 Charm Production 16
1.3.2 Charm Fragmentation 19
1.3.3 Properties of the D^* Meson 20
1.4 NLO Calculations 21
1.5 Event Generators and Detector Simulation 22

2 HERA and the H1 Detector **24**
2.1 HERA 24
2.2 The H1 Detector 25
2.3 Central Tracking Detectors 27
2.4 Track Reconstruction 29
2.5 Calorimeters 31
2.6 The Trigger 32
2.7 The Luminosity System 33

3 Event Selection **36**
3.1 General Event Selection 36
3.2 Online Selection 36
3.3 Offline Reconstruction of the DIS Events 37
3.3.1 Reconstruction of the Kinematics 37
3.3.2 Scattered Electron Selection 42
3.4 Selection of $D^{*\pm}$ candidates 46
3.4.1 Track selection 47
3.4.2 The reconstruction of the D^* meson 52

3.4.3 Additional Reduction of the Background 54

4 Cross Section Determination and Systematic Uncertainties 59
4.1 Determination of the Cross Section 59
4.1.1 Signal Extraction 59
4.1.2 Reconstruction Efficiencies 62
4.1.3 Radiative Corrections 68
4.1.4 Contribution from Reflections 70
4.1.5 Trigger Efficiencies 70
4.2 Experimental Systematic Uncertainties 72
4.2.1 Uncorrelated Uncertainties 72
4.2.2 Correlated Uncertainties 73
4.3 Cross Sections 82
4.3.1 Total Cross Section 82
4.3.2 Single Differential Cross Sections 82
4.3.3 Double Differential Cross Sections 91
4.4 Comparison with Other Measurements 98

Conclusions 102

Introduction

The present understanding of the structure and dynamics of the Universe at the smallest experimentally accessible scales is represented by the Standard Model (SM) of elementary particles and interactions. In this theoretical framework, the elementary particles are grouped in gauge bosons and three families of fermions. The photon (γ), $W^{\pm}$ and Z^0 carry the electroweak interaction and the gluons mediate the strong interaction. Each family of fermions contains two quarks and two leptons, the former interacting both strongly and electroweakly and the latter participating just in the electroweak force. The Standard Model was and still is extensively tested and improved, its ultimate precision being one of the goals of modern particle physics research.

The Standard Model uses quantum field theory to describe the dynamics of the elementary particles: electroweak theory for the electroweak interactions and quantum chromodynamics (QCD) for the strong interactions. A good testing ground for these theories is represented by deep inelastic scattering of leptons on nucleons, where the exchanged boson (photon, Z^0, $W^{\pm}$) is utilized to probe the nucleon. Deep inelastic scattering experiments had a crucial role in the measurement of the nucleon structure. The HERA[1] accelerator at DESY[2] in Hamburg, where electron and proton beams have been collided, allowed the access to much higher energies than realized at fixed target experiments. At HERA many aspects of the Standard Model, in particular of QCD, have been confirmed with high experimental precision. At present, HERA results represent the ultimate knowledge of nucleon structure.

The mass of the charm quark, m_c, provides a sufficiently high scale to apply perturbative QCD (pQCD) to the cross section calculations. However charm production is a multi-scale problem since additional scales are involved, e.g. the virtuality Q^2 of the exchanged photon and the transverse momentum $p_\perp$ of the outgoing quarks. Depending on the details of the treatment of m_c, Q^2 and $p_\perp$, different approaches in pQCD have been formulated. Fixed-order QCD calculations are reliable to calculate total and differential charm quark production cross section and are used in the present work.

At HERA, different techniques have been used to measure open charm production cross sections in deep inelastic scattering. Beside the full reconstruction of the charmed mesons, the long lifetime of the heavy flavoured

[1]Hadron-Elektron-Ring-Anlage.

[2]Deutsches-Elektronen-Synchrotron.

hadrons or their semileptonic decays are exploited. These different methods of charm tagging have advantages and disadvantages. In general, the best signal-to-background ratio of the charm samples can be achieved by the measurement of fully reconstructed $D^{*\pm}(2010)$ mesons, this method being used in the present work.

The charm production represents a particular challenge at low virtualities of the exchanged photon, where the mass of the charm quark is of the same order as Q^2. The precision of the measurements in this region is very important, as it impacts the parton distribution functions at the starting scale. The visible phase space of charm production accesible with D^* mesons is limited by the constraint of measuring all products from the D^* meson decay. Improvements in the detector understanding allowed access to an extended phase space of the charm production in the Q^2 range between 2 and 100 GeV^2 and inelasticity y between 0.02 and 0.7.

The thesis is structured in four chapters. In the first chapter, the theoretical framework of the deep inelastic scattering is presented. Also, the Monte Carlo program and the next-to-leading order calculation used are reviewed. The second chapter is devoted to the H1 detector, with a focus on the components relevant to this analysis and the general event reconstruction algorithm. In the third chapter, the event selection of the D^* sample is described. The fourth chapter covers the cross section measurement and the comparison with the leading order and next to leading order QCD predictions. The results are summarized in the last chapter.

Chapter 1: Open Charm Production in DIS

The present understanding of the structure and dynamics of the matter at the smallest experimentally accessible scales is summarised by the Standard Model (SM) of elementary particles and interactions. In this SU(3) $\times$ SU(2) $\times$ U(1) gauge theory, the elementary particles are grouped in gauge bosons and three families of fermions. The photon (γ), $W^{\pm}$ and Z^0 carry the electroweak interaction and the gluons mediate the strong interaction. Each family of fermions contains two quarks and two leptons.

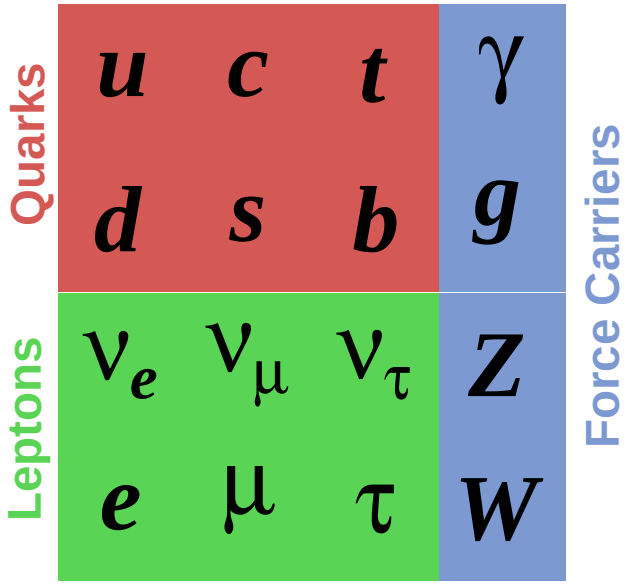

Figure 1.1: Elementary particles in the Standard Model. The picture was obtained using a code from [BR97].

The quarks come in six flavours: up (u), down (d), strange (d), charm (c), beauty (b) and top (t), and in three colors: red (r), green (g) and blue (b). The u, d and s flavours are considered 'light flavours', whereas the other three, c, b and t, are called 'heavy flavours'. This distinction is made

with respect to the mass of the proton - the light flavored ones have masses up to 130 MeV, while the c, the lightest of the heavy quarks, has a mass[1] [N$^+$10] of 1.27 GeV. There are two leptons in each family, one negatively charged (electrons, muons and taus) and one electrically neutral (associated neutrinos). Although the exact values of the neutrino masses are not known, there are upper limits set [N$^+$10] and they are definitely not massless.

The main theoretical aspects of the Standard Model, with a focus on those relevant in the case of DIS and heavy flavour production are detailed in the following sections. Also, an overview of the detector simulation and event generators used in this analysis are given.

1.1. Electron-Proton Scattering and the Quark Parton Model

1.1.1. The Kinematics of the Deep Inelastic Scattering

The interaction between the lepton and the nucleon is mediated by the exchange of a virtual vector boson, γ, Z^0 or $W^{\pm}$. A graphic representation of an neutral current process (in which a γ or Z^0 is exchanged) is shown in Figure 1.2.

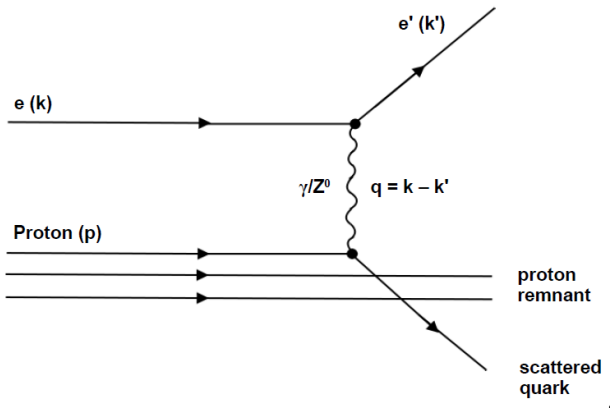

Figure 1.2: Schematic representation of lepton-proton scattering.

Starting from the 4-momenta notations introduced above, the kinematics of a DIS process[2] is characterized using the following notations:

- the virtuality of the exchange boson:

$$Q^2 = -q^2 = -(k - k')^2 \tag{1.1}$$

[1] The masses quoted are estimated in the $\overline{\text{MS}}$ scheme, which will be presented in section 1.2

[2] A scattering process is considered 'deeply inelastic' if it takes place at large momentum transfer $(k - k')^2 \gg M_T^2$ and $M_{\text{final state}} \gg M_T^2$, where M_T is the mass of the target.

- the centre-of-mass energy squared:

$$s = (k + p)^2 \tag{1.2}$$

- the invariant mass squared of the hadronic final state (the proton remnant plus the scattered quark) is given by:

$$W^2 = (q + p)^2 \tag{1.3}$$

- the Bjørken-x variable:

$$x = \frac{Q^2}{2p \cdot q} \tag{1.4}$$

- the inelasticity, or the fraction of energy transferred from the lepton to the hadronic system in the nucleon's rest frame:

$$y = \frac{p \cdot q}{p \cdot k} \tag{1.5}$$

  The range for x and y are:

$$0 \leq x, y \leq 1 \tag{1.6}$$

In the proton rest frame, the expression for y is reduced to:

$$y = 1 - \frac{E'_l}{E_l}$$

The expression for Q^2 can then be written:

$$Q^2 = 2E_l E'_l(1 - cos\ \theta)$$

where θ is the angle between the incoming and the scattered lepton. This expression holds in all reference frames.

In the data analysed, positrons are scattered on protons. Only the case of one photon exchange is considered. The reason is that, in the studied Q^2 range (2-100 GeV^2), the contributions from the weak interactions are suppressed by $Q^2/M^2_{Z^0,W^\pm}$, where $M_{Z^0} \approx 91$ GeV and $M_{W^\pm} \approx 80$ GeV. If the masses of the electron and the proton are considered negligible, one gets:

$$Q^2 \approx sxy$$

$$W^2_{\gamma^* p} \approx ys - Q^2$$

where p stands for proton. In this case, only three Lorentz-invariant variables determine the complete kinematics of the lepton-nucleon scattering. Having

constant beam energies at HERA, just two variables are needed to describe the kinematics of a DIS event. The resolving power of the photon for probing the proton is given by:

$$\Delta b \sim \frac{\hbar c}{\sqrt{Q^2}} = \frac{0.197}{\sqrt{Q^2}}\ GeV\ fm$$

Before HERA, there were no measurements in the low Bjørken-x region, particularly below 0.01. The energies available, 27.6 GeV for the leptons and 920 GeV for the protons, have made it possible to access x-values down to 10^{-6} [AAA+09].

1.1.2. The Parton Model and the Inclusive DIS Cross Section

The basic idea of Feynman's parton model [Fey72] is to represent the inelastic electron-nucleon scattering as a scattering of the exchanged photon from point-like quasi-free constituents within the proton when viewed from a frame in which the proton has infinite momentum and provided the collision is deeply inelastic. In this frame of infinite momentum, the transverse momenta of the proton's constituents and their masses can be neglected. This assumption has two consequences:

1. The parton 4-momentum can be written as a fraction of the nucleon 4-momentum, $p = fP$, where f is a number and p is the 4-momentum of the parton.

2. The deep inelastic scattering can be seen as an incoherent sum of point-like elastic scattering of spin-$\frac{1}{2}$ nucleon components (the partons).

The inclusive cross section for lepton-nucleon DIS is given by [DCS04]:

$$\frac{d^2\sigma}{dQ^2dx} = \frac{4\pi\alpha^2}{Q^4x}\left[(1-y)F_2(x) + \frac{y^2}{2}2xF_1(x)\right] \tag{1.7}$$

where

$$F_2(x) = \sum_i e_i^2 \int_0^1 dx'\ q_i(x')x'\delta(x'-x)$$

and

$$2F_1(x) = \sum_i e_i^2 \int_0^1 dx'\ q_i(x')\frac{x}{x'}\delta(x'-x)$$

are structure functions, the fractional momentum of the struck parton, x', is identified with Bjørken-x, $e' = e_i e$ is the electrical charge of the quark in terms of the electron charge e and $q_i(x)$ is the distribution function which gives

the probability that the struck quark i carries a fraction x of the nucleon's momentum p.

Assuming that the proton constituents participating in the scattering are point-like spin-$\frac{1}{2}$ particles, Callan and Gross showed [CG69]:

$$2xF_1(x) = F_2(x) \tag{1.8}$$

or

$$F_L(x, Q^2) = 0. \tag{1.9}$$

The first observations of DIS [BCD$^+$69, BFK$^+$69, BBD$^+$79] occured in a region ($x \simeq 0.1$) where the Bjørken scaling holds, therefore confirming the quark parton model.

Taking Equation 1.8 into account, the cross section can be written as:

$$\frac{d^2\sigma}{dQ^2dx} = \frac{2\pi\alpha^2}{Q^4x}\left[\left(1 + (1-y)^2\right) F_2(x)\right] \tag{1.10}$$

where the term $1 + (1-y)^2$ is called the helicity factor Y_+.

1.2. The DIS Formalism in Quantum Chromodynamics

The concept of 'colour' was introduced [Gre64] in order to preserve the antisymmetry of the Δ^{++} meson's wavefunction, i.e., one more degree of freedom was needed, in addition to flavor, spin and space. The colour attribute for quarks can take any of the three possible values, denoted by: red (R), green (G) and blue (B), the quarks being assigned to a triplet of an $SU(3)$ colour group. The gluons form an $SU(3)$ color octet and they can carry the following colour combinations:

$$\mathrm{R\bar{G}}, \mathrm{R\bar{B}}, \mathrm{G\bar{R}}, \mathrm{G\bar{B}}, \mathrm{B\bar{R}}, \mathrm{B\bar{G}}, \sqrt{\frac{1}{2}}(\mathrm{R\bar{R}} - \mathrm{G\bar{G}}), \sqrt{\frac{1}{6}}(\mathrm{R\bar{R}} + \mathrm{G\bar{G}} - 2\mathrm{B\bar{B}}) \tag{1.11}$$

The $SU(3)$ colour singlet,

$$\sqrt{\frac{1}{3}}(\mathrm{R\bar{R}} + \mathrm{G\bar{G}} + \mathrm{B\bar{B}}) \tag{1.12}$$

does not carry colour and can't mediate between colour charges. From the perspective of the SU(3) algebra, the interaction of a gluon with a quark is understood as rotating the quark's colour in the SU(3) space. Neither quarks, nor gluons are observed as free particles. They can exist only in colourless combinations, called 'hadrons', which are colour singlets under SU(3) colour group. This property of the colour interaction is called 'confinement'. All colourless states are invariant under colour rotations in the SU(3) space -

the leptons don't feel the strong interaction. Experimentally, only two types of hadrons are obeserved: three-quark or three-antiquark compunds, called 'baryons', and quark-antiquark mixtures, called 'mesons', though other combinations are hypothesized to exist, like glueballs and pentaquarks. The formalism describing the colour interactions was derived within the framework of quantum field theory and it is called 'Quantum Chromodynamics' (QCD).

1.2.1. Renormalization and the Running of the Strong Coupling Constant

Renormalization is a collection of techniques used to regulate the divergences which appear in the contributions to the perturbative expansion of scattering amplitudes beyond leading order. A renormalizable field theory is one in which the renormalization of a finite number of parameters ensures finite results for calculations to all orders of perturbation theory.

In the Quark Parton Model, the quarks are considered quasi-free, which implies that the coupling strength of the interaction is weak in the short-distance, high momentum transfer regime. The failure of observing free quarks led to the assumption that the coupling constant of the interaction must be rather large in the long-distance, low momentum transfer regime, making the quarks confined in the hadrons. This behaviour of the coupling constant is determined by the self-interaction of gluons, which has as a result an antiscreening effect from the vacuum polarization. Calculating the QCD coupling constant according to the renormalization group equation, one obtains that α_s is described by a decreasing function of the characteristic energy scale in the interaction. In the leading order approximation α_s is given by:

$$\alpha_s(Q^2) = \frac{4\pi}{\beta_0 \ln \frac{Q^2}{\Lambda^2}}, \quad \text{with } \beta_0 = 11 - \frac{2}{3} n_f \tag{1.13}$$

where n_f is the number of quark flavours and Λ characterizes the strength of the coupling. The latter depends on the number of active flavours and, in case of higher order calculations, on the convention.

In QCD, three types of divergences occur:

- **Infrared divergences.** They appear when a quark emits a very soft gluon ($E_g \to 0$) or an electron emits a very soft photon. An example of this kind of diagram is shown in Figure 1.3.

- **Collinear divergences.** This kind of divergences appears when a quark radiates a collinear gluon ($\cos \theta_{qg} \to 1$).

- **Ultraviolet divergences.** When diagrams with loops, like those in Figure 1.4, are included in the cross section calculations, ultraviolet

divergences arise due to the infinite loop momenta, i.e., the particle in the loop can have infinite momentum.

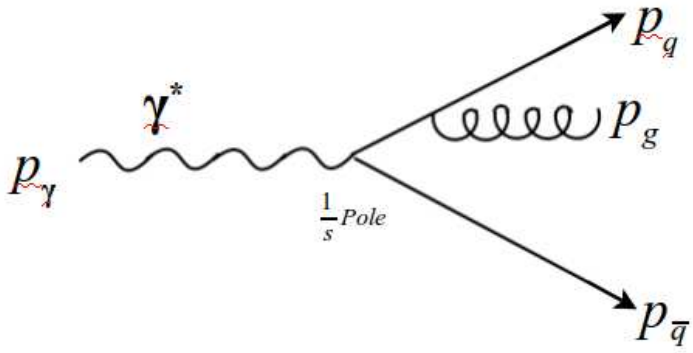

Figure 1.3: Diagram for $\gamma^* \to q\bar{q}g$ showing the particle 4-momenta.

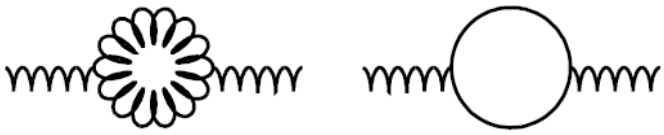

Figure 1.4: Examples of Feynman loops.

There are several renormalization techniques which help getting rid of the divergences. One of the renormalization schemes is the minimal subtraction scheme of 't Hooft and Veltman (MS). Considering the divergence arising from a Feynman loop integral (two examples can be seen in Figure 1.4):

$$\int \frac{d^4k}{k^2 - m^2 + i\varepsilon}$$

which diverges quadratically, is dimensionally regularized by evaluating the integral in an n-dimensional space ($n \neq 4$) in which it converges:

$$\int \frac{d^4k}{k^2 - m^2 + i\varepsilon} \to i\pi^{\frac{n}{2}} \Gamma\left(1 - \frac{n}{2}\right) \left(-m^2\right)^{\frac{n}{2}-1}$$

where

$$\Gamma(1 - \frac{n}{2}) = -\frac{2}{4-n} - 1 + \gamma_E + O(4-n)$$

γ_E being the Euler constant, $\varepsilon > 0$ an arbitrarily small non-zero number and the divergences occuring as the pole at $n = 4$. However, for most perturbative

calculations, it is preferred that the singular terms and the terms involving γ_E terms are removed. This scheme is called the modified minimal subtraction scheme ($\overline{\text{MS}}$).

The renormalization procedure introduces an additional parameter, called the renormalization scale (μ_R), which is chosen for removing the ultraviolet divergences. This parameter being arbitrary, the theory retains its power of prediction as long as it doesn't depend on the particular choice of μ_R.

1.2.2. Scaling Violations in QCD

One of the predictions of the quark-parton model is that the structure functions F_i scale and don't depend on Q^2, when Q^2 and the lepton's energy loss in the nucleon rest frame goes to ∞. This property is related to the assumption that the transverse momentum of the partons in the infinite momentum frame of the proton is small. In QCD, gluons carry colour and therefore vertices of the type ggg and qqg also appear. The gluon emission leads to the production of partons and hadrons with high transverse momenta. Considering the one-gluon emission contribution, the structure function F_2 becomes:

$$\frac{F_2\left(x,Q^2\right)}{x} = \sum_q e_q^2 \int_x^1 \frac{dy}{y} q(y) \left(\delta\left(1-\frac{x}{y}\right) + \frac{\alpha_s}{2\pi} P\left(\frac{x}{y}\right) log\frac{Q^2}{\mu^2} \right) \quad (1.14)$$

where $q(y)$ is the quark structure function and $P(\frac{x}{y})$ are the splitting functions that describe the probability of a given parton splitting into two other partons. The log Q^2 term leads to a violation of the parton model scaling for the structure functions. As Q^2 increases, more and more gluons are radiated, which in turn split into $q\bar{q}$ pairs. This process leads both to softening of the initial quark momentum distributions and to the growth of the gluon density and the $q\bar{q}$ sea as x decreases. The behaviour of the proton structure function F_2 for two fixed Q^2 values is shown in Figure 1.5.

The structure function F_2 also has a strong dependence on Q^2 at fixed x, as it can be seen in Figure 1.6. The H1 and ZEUS measurements span a wide range in x, showing the differences between the scaling violations at high x, where F_2 decreases as a function of Q^2 due to gluon bremsstrahlung, and at low x, where F_2 increases as a function of Q^2 mainly due to $q\bar{q}$ pair production from the splitting of the gluon in a quark-antiquark pair, $g \to q\bar{q}$.

1.2.3. QCD Factorization

Factorization is the hypothesis that the cross section for DIS may be written as the convolution of two terms: a calculable hard scattering cross section

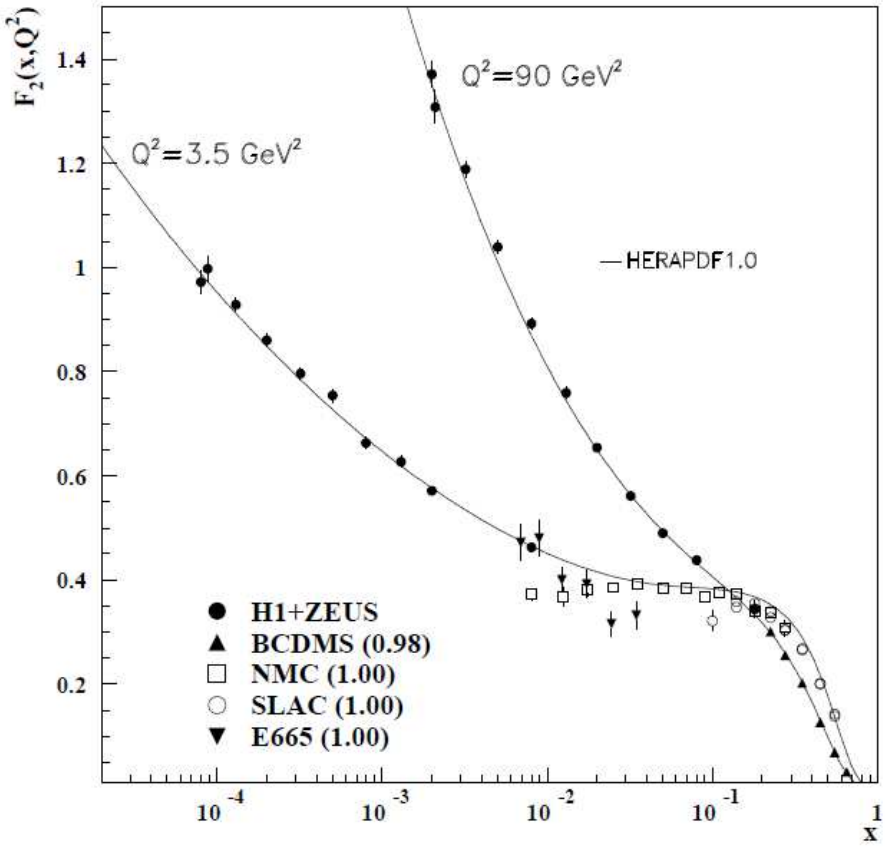

Figure 1.5: The proton structure function F_2 at two fixed Q^2 values (3.5 GeV^2 and 90 GeV^2). Figure from [N$^+$10], page 203. References for the data sets are given there.

and a non-perturbative parton density distribution. The factorization theorem has been proved only for a few processes, though it is assumed to hold for most processes taking place at high energy colliders. The factorization theorem is usually expressed in a specific scheme, like DIS or $\overline{\text{MS}}$. In the DIS scheme, the gluon contributions are absorbed into the parton distributions, while in the $\overline{\text{MS}}$ only the collinear divergency is factorized out. Particular schemes are used when studying heavy flavour production, which will be detailed in Section 1.3. The factorization scale considered in the predictions used in this analysis is $Q^2 + 4m_c^2$.

1.2.4. Parton Evolution Models

Parton distribution functions (PDFs) are the momentum distribution functions of the partons inside the proton and they represent the probability

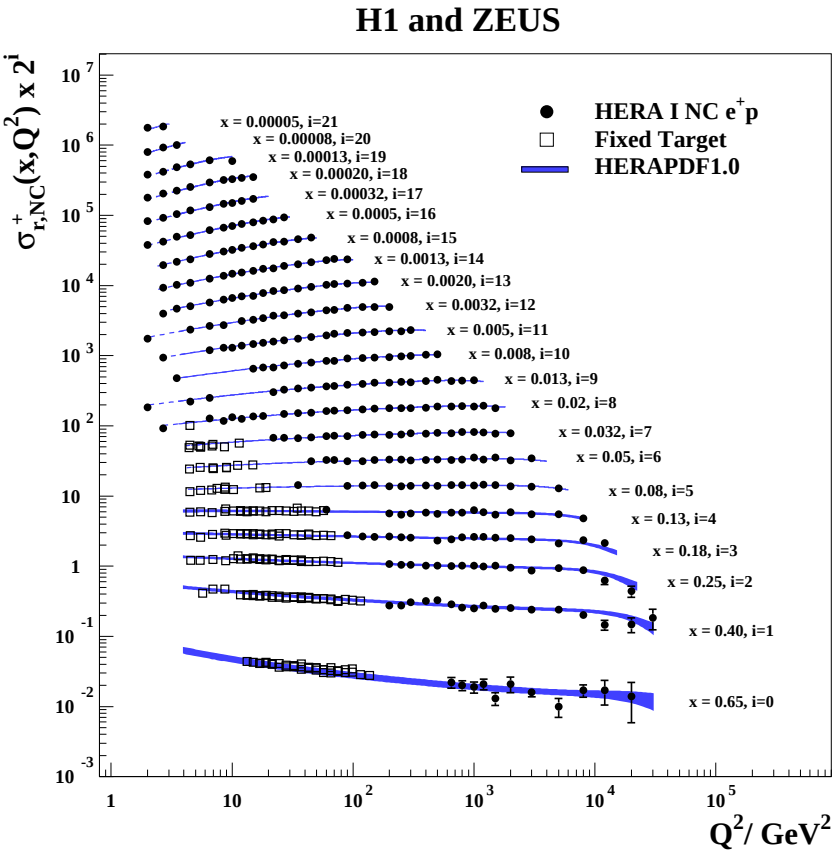

Figure 1.6: HERA combined neutral current e^+p reduced cross section and fixed target data as a function of Q^2. The error bars indicate the total experimental uncertainty. The HERAPDF1.0 is represented by the blue line. Figure taken from [A+10].

densities to find a parton carrying the momentum fraction x at a specific Q^2 value. DIS experiments have shown that the number of partons increases at low x with Q^2 and decreases at high x. The valence quarks dominate the nucleon structure at low Q^2, whereas at high Q^2 more quark-antiquark pairs carrying low momentum fractions x are available. The gluon contribution to the nucleon structure increases together with Q^2.

The PDF sets are obtained by a fit on a large number of cross section data points in a large grid of Q^2 and x values from one or several experiments. The most commonly used procedure consists of parametrising the dependence of the parton distributions (quarks, antiquarks, gluons) on the variable x at

the lowest value possible of Q^2 and use the DGLAP[3] equations to get their behaviour at higher energies. This lowest value of Q^2 is denoted Q_0^2 and it is large enough that the unknown terms of the perturbative equations are assumed to be negligible. The number of parameters left free for the fitting procedure is typically between 10 and 30 [Fel10]. An example of a PDF set is the HERAPDF1.0, shown in Figure 1.7 at the starting scale $Q^2 = 1.9$ GeV^2. The PDFs are universal, i.e., once determined they can be used for calculating the cross section for any hard process to which the factorization theorem is applicable.

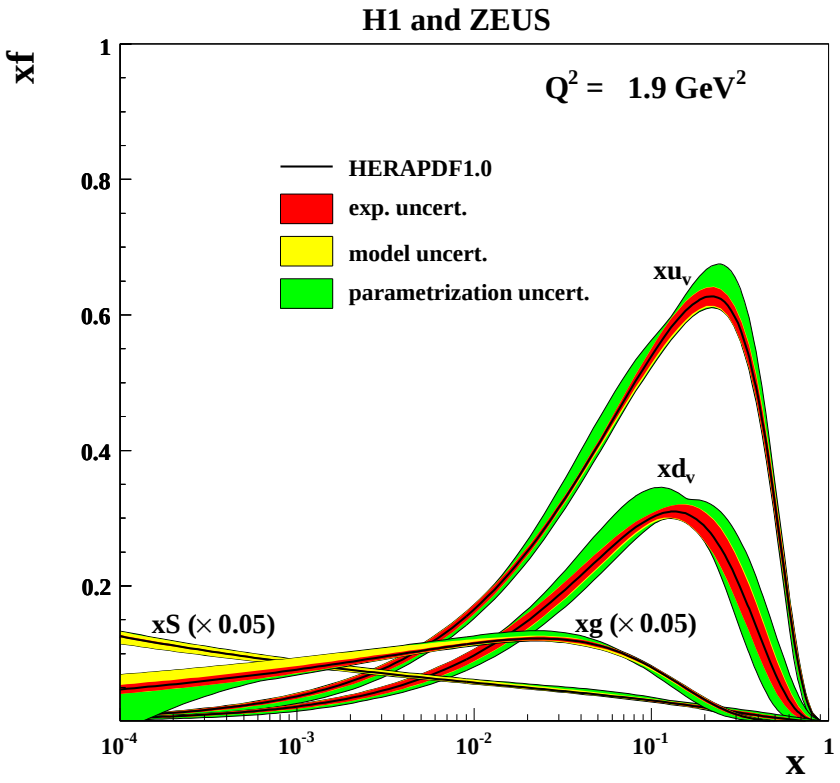

Figure 1.7: Extracted parton densities from the HERA PDF fit HERAPDF1.0 for the valence quarks xu_v and xd_v, the sea quarks xS and the gluons xg. The uncertainties are shown in red for experimental uncertainty, yellow for the model uncertainty and green for the parametrization uncertainty.

[3]Dokshitzer Gribov Lipatov Altarelli Parisi

By 'parton evolution' one understands the dependence of the parton distribution functions in the proton on the energy scale. There are several parton evolution models, each of them providing a specific treatment of the parton distributions. The most widely used one for predictions at collider experiments is the DGLAP model [Dok77, GL72, AP77], which gives Q^2-dependent parton distributions and holds for medium and high x range. The BFKL[4] model [KLF77, BL78] provides unintegrated gluon densities and it is intended for the small x regime, while CCFM[5] [Cia88, CFM90a, CFM90b, Mar95] attempts to cover both ranges and has DGLAP and BFKL as border cases.

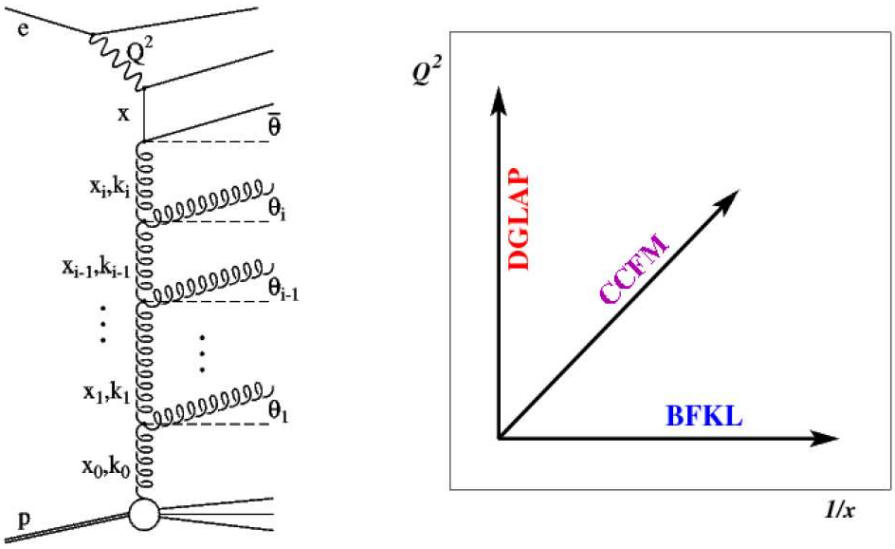

Figure 1.8: Gluon ladder in DIS (left) and the three main evolution schemes (right). The graphic on the right shows the dependence of the evolution of the parton densities for each scheme.

DGLAP. The equations give a formalism for calculating the changes of the parton densities as Q^2 changes. The procedure involves the summation of leading $\alpha_s \ln Q^2/\mu^2$ terms and it assumes that the gluons in the gluon ladder are ordered in Q^2. It requires input from elsewhere for the x dependence of the parton distribution functions at the starting scale Q_0^2. This type of evolution has been tested at HERA and it holds for most of the HERA range, though it is expected to break at small x. The evolution equations for quark and gluon densities in the proton are:

[4]Balitsky Fadin Kuraev Lipatov
[5]Ciafaloni Catani Fiorani Marchesini

$$\frac{dq_i(x,Q^2)}{d\ logQ^2} = \frac{\alpha_s}{2\pi}\int_x^1 \frac{dy}{y}\left(q_i(y,Q^2)P_{qq}\left(\frac{x}{y}\right) + g(y,Q^2)P_{qg}\left(\frac{x}{y}\right)\right) \quad (1.15)$$

$$\frac{dg(x,Q^2)}{d\ logQ^2} = \frac{\alpha_s}{2\pi}\int_x^1 \frac{dy}{y}\left(q_i(y,Q^2)P_{gq}\left(\frac{x}{y}\right) + g(y,Q^2)P_{gg}\left(\frac{x}{y}\right)\right) \quad (1.16)$$

In Equation 1.15, the index i runs over all quark flavours. The second term considers the probability $\alpha_s P_{qg}(x/y)$ that a quark with momentum fraction x is the result of $q\bar{q}$ pair creation py a parent gluon with momentum fraction $y > x$. In Equation 1.16, the index $i = 1, ..., 2n_f$ runs over quarks and antiquarks of all flavours. The processes described by the splitting functions P are shown in Figure 1.9.

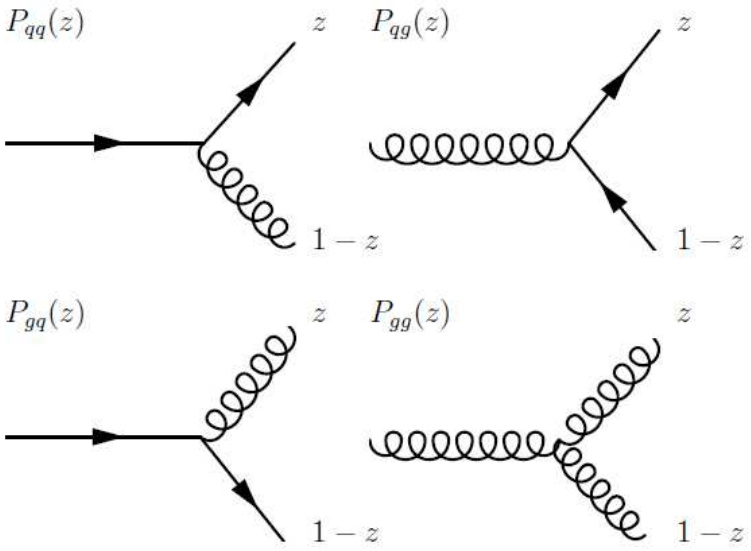

Figure 1.9: Diagrams illustrating the processes described by the splitting functions.

BFKL. At very small x and small Q^2 the logarithmic terms in Q^2 are no longer divergent, but problems arise from logarithmic terms in $1/x$. The gluon density increases strongly at low x, and the gluon induced processes are dominating this regime. The resummation of the logarithmic terms in $1/x$ is done independent of Q^2 in the BFKL framework, in which the rungs from the gluon ladder are strongly ordered in their longitudinal momenta. The result is the BFKL evolution equation, which gives the evolution in x of the unintegrated gluon density function F_g in terms of x and transverse

momentum k_T. This function is related to the gluon density that appears in the DGLAP equations by:

$$xg(x,Q^2) = \frac{1}{\pi}\int_0^{Q^2} \frac{d^2\mathbf{k}}{\mathbf{k}^2}\Theta(Q^2-\mathbf{k}^2)F_g(x,\mathbf{k}) \tag{1.17}$$

CCFM. The CCFM equation is the application of angular ordering to the calculation of the gluon ladder. It provides an alternative approach to inclusive DIS. The predictions are given also in the form of unintegrated gluon densities. BFKL and DGLAP equations are border cases of the CCFM set.

1.3. Heavy Quark Production in *ep* Scattering

1.3.1. Charm Production

Conventional perturbative QCD theory is formulated most simply in terms of zero-mass partons and the factorization theorem provides a straightforward procedure for order-by-order perturbative calculations in the case of processes depending on just one hard scale Q [TKS02]. The heavy flavour quark (c, b and t) production brings an additional hard scale in the perturbative calculations, due to the large masses of these quarks. There are several prescriptions for treating the heavy flavour production, some considering the heavy quark masseless, like the Zero-Mass scheme (ZM), and some which take into account the mass of the heavy quark, $m_{\rm hq}$ and the ratio $\rm m_{hq}/Q$, like Fixed Flavour Number Scheme (FFNS) and General Mass Variable Flavour Number Scheme (GMVFNS).

In the conventional parton-model approach the zero-mass parton approximation is applied to a heavy quark calculation as soon as the energy[6] scale E of the physics process is above the mass scale m_{hq} of the heavy quark, leaving E as the only apparent hard scale of the problem. This scheme is well suited for analyses in which $E^2 \gg m_{hq}^2$. However, as one approaches the charm production threshold region, the calculations become unreliable [TKS02].

In the fixed flavour number scheme, the proton consists of gluons and three light (u, d, s) active flavours. The heavy flavour quarks appear only in the final state and are generated perturbatively. The mass parameter m_{hq} is explicitely kept along with the energy scale. As E becomes large with respect to m_{hq}, this approach becomes unreliable, since the perturbative expansion contains terms of the form $\alpha_s^n log^n(m_{\rm hq}^2/E^2)$ at any order n. This type of terms are not infrared safe as $m_{\rm hq} \to 0$ or $E \to 0$.

[6]The energy scale E is a generic name for a typical kinematic physical scale: Q^2, W or $p_\perp$, depending on the process.

A model which combines the two aforementioned approaches was also developed, the so called 'generalized mass variable flavour number scheme' [TT08]. This consists of a sequence of n_f-FFNS calculations, each in its region of validity, for flavour number $n_f = 3, 4, ...$ They are matched at a certain scale which is usually set to the heavy quark mass.

The charm production in DIS proceeds mostly via photon-gluon fusion, $\gamma g \to c\bar{c}$. In this case, the charm production is directly sensitive to the gluon density in the proton. By comparing the measured charm cross section with the gluon density from the inclusive analyses, a powerful cross check on the perturbative QCD calculations is available.

There are two types of mechanisms through which the charm quark may be produced in DIS: direct and resolved. In the direct process, the interaction is point-like between the photon and the gluon. In DIS, the direct process dominates the medium and high Q^2.

The resolved processes contribute mainly at low Q^2. In this case, the photon behaves like a source of partons, one of which takes part in the hard interaction, thus 'resolving' the hadronic structure of the photon. Since the photon virtuality and the large mass of the heavy quark suppress the hadronic fluctuations of the photons, the contribution from these processes decreases rapidly with Q^2, such that their contribution is negligible at medium and high Q^2. Diagrams for direct and resolved processes are shown in Figure 1.10.

There are other processes which can produce charm in the DIS: diffractive heavy flavour production, scattering off charmed sea quarks and intrinsic charm in the proton [AC99]. These processes have either been measured to have small cross sections relative to the already discussed mechanisms, or are not expected to contribute in the current kinematic regions.

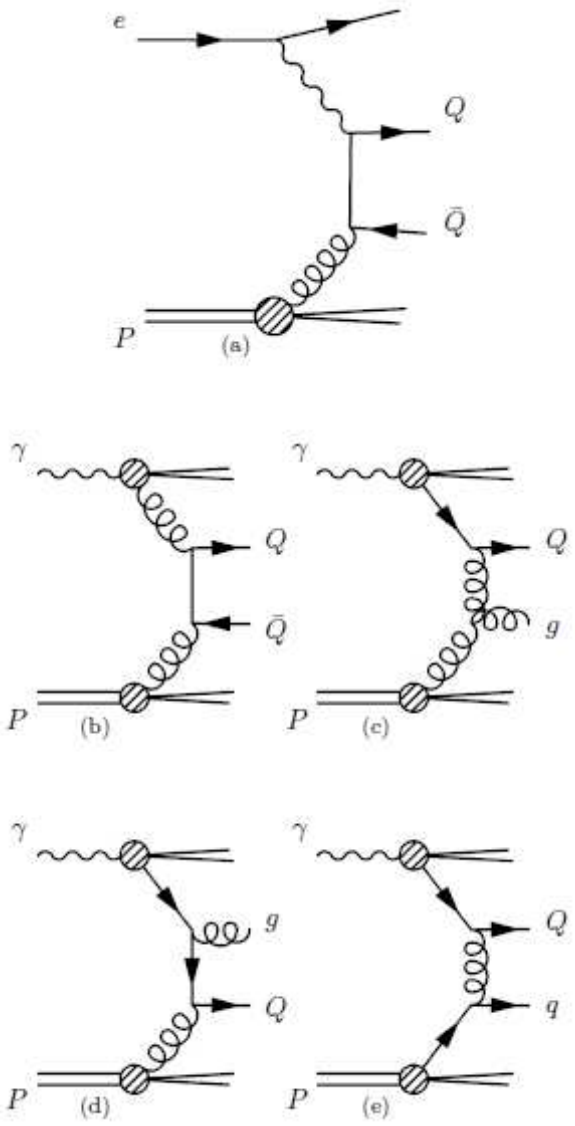

Figure 1.10: Heavy quark production processes in LO QCD: boson-gluon fusion (a) and resolved photon processes (b-e).

1.3.2. Charm Fragmentation

Experimentally, heavy quarks are not observed directly, but heavy flavoured hadrons are measured instead. The fragmentation of the quarks into hadrons is described only by phenomenological models. The fragmentation process is assumed to be independent of the production mechanism of the heavy quark. Within the fragmentation process two independent aspects have to be considered. One aspect concerns the probability that a quark will turn into a certain colourless object. The fraction $f(c \to D^*)$ of charm quarks fragmenting into D^* mesons is 23.5±0.7 % [Loh11]. The other aspect deals with the fragmentation function $D_{hq}^{H}(z)$, where z is the energy fraction which is transferred due to fragmentation from the parent parton hq to the daughter hadron H. The fragmentation function can be factorized into a hard interaction part and a soft non-perturbative part. The first part is described perturbatively by parton showers, where the virtual quarks participating in the hard matrix element emit particles until they become on-shell. The non-perturbative part, or hadronization, corresponds to the transition of the on-shell partons to bound hadron states.

There are several hadronization models available, among them the Lund String model and the cluster model. In the Lund String model, when both particles of a $q\bar{q}$ pair are moving away after the interaction, the resulting colour field is compressed into a string. If sufficient energy is stored in this string it breaks and a new $q\bar{q}$ pair is produced. Radiated gluons cause kinks in the strings, which influence the angular distribution of the hadrons produced. This model is utilized in the Monte Carlo generator used in this analysis.

The cluster model assumes that, when the virtualities of the partons in the cascade reach a lower limit, beyond which the perturbation theory can't be applied any more, any gluons in the cascade are forced to split non-perturbatively in $q\bar{q}$ pairs. Those pairs sharing a colour index form color singlet clusters. The clusters convert into hadrons by isotropic quasi-two-body decays into pairs of resonances. This model has few parameters compared to the Lund String model and a natural mechanism for generating tranverse momenta and suppressing the heavy particle production in hadronization [Web00].

For the fragmentation of the heavy flavoured quarks, different models are employed. The most known and used are Peterson fragmentation [PSSZ83], Bowler model [Bow81, Mor89] and Kartvelishvili function [KLP78]. These functions describe the longitudinal momentum transfer ($z = E_H/E_{hq}$) from the quark hq to the hadron H:

$$\textit{Peterson: } D_{hq}^{H}(z) \propto \frac{1}{z[1 - 1/z - \epsilon_{hq}/(1-z)]^2} \tag{1.18}$$

$$\textit{Bowler: } D_{hq}^{H}(z) \propto \frac{1}{z^{1+b\, r_{hq}\, m_Q^2}} \cdot (1-z)^a \cdot exp\frac{b\, M_T^2}{z} \tag{1.19}$$

$$\textit{Kartvelishvili: } D_{hq}^{H}(z) \propto z^{\alpha} \cdot (1-z) \tag{1.20}$$

The Peterson and the Kartvelishvili parametrisations have one free parameter each, ϵ_Q and α, respectively, whereas the Bowler function has two free parameters, a and b. The value m_Q is the mass of the heavy quark, $M_T = \sqrt{M_H^2 + p_\perp^2}$ stands for the transverse mass of the hadron H with the transverse momentum $p_\perp$, r_Q for the radius of the quark which is set to 1 by default. The ϵ_Q parameter scales for charm and beauty fragmentation with $1/m_Q^2$ [N$^+$10]. The heavy quark fragmentation function is expected to be harder than that of the light flavours because the formed hadron carries a high momentum fraction and for heavy quarks the fragmentation function peaks near 1 [N$^+$10].

1.3.3. Properties of the D^* Meson

The charged D^{*+} (D^{*-}) meson with the quark content $c\bar{d}$ ($\bar{c}d$) is the lowest excited state of the charged D meson. With its quantum numbers $I(J^P) = 1/2(1^-)$, where I stands for isospin, J for angular momentum and P for parity, the $D^{*\pm}$ meson is a vector meson. Its mass amounts to 2010.28±0.13 MeV [N$^+$10] which differs from the mass of the D^0 meson 1864.86±0.0.13 MeV by somewhat more than one pion mass.

The D^* meson decays into a neutral pion or a photon and a $D^\pm$ meson or into a charged pion and a D^0 meson. The total decay width Γ of the D^* amounts to 96±22 keV. The decay channels with their branching ratios are summarized in Table 1.1. In this analysis only the decay of the D^* in $D^0\pi^\pm$ is used. Due to the small difference between the D^* and the D^0 mesons, the pion is produced in this decay with a small momentum in the D^* rest frame. It is therefore denoted 'slow pion' (π_s).

Decay channel	Fraction
$D^0\pi^\pm$	(67.7±0.5) %
$D^\pm\pi^0$	(30.7±0.5) %
$D^\pm\gamma$	(1.6±0.4) %

Table 1.1: Decay channels of the charged D^* meson [N$^+$10].

The D^0 decays via the weak interaction with a mean lifetime of $\tau = (410.1 \pm 1.5) \cdot 10^{-15}$ s. The decay channels relevant for this analysis together with their branching fractions are listed in Table 1.2. For this analysis the decay of the D^0 meson into a charged kaon and a charged pion is used. It

follows that in the final state only charged particles are present, which can be detected with track detectors. For the reconstruction of D^* mesons a strong background suppression exists due to the small phase space of the π_s. This particular decay channel is also called the 'golden channel'.

Decay channel	fraction
$K^{\pm}\pi^{\mp}$	(3.80±0.07) %
$K^{\pm}K^{\mp}$	(3.84±0.10) $\cdot 10^{-3}$
$\pi^{\pm}\pi^{\mp}$	(1.364±0.032) $\cdot 10^{-3}$
$K^{\pm}l^{\mp}\nu_l$	(6.7±0.4) %
$\pi^{\pm}\pi^{\mp}\pi^0$	(1.31±0.06) %

Table 1.2: Selection of decay modes of the D^0 meson, where the meson decays into charged particles [N$^+$10].

1.4. NLO Calculations

In this analysis the HVQDIS program [HS95, HS98] is used for the NLO calculation of the D^* cross sections in the massive scheme. This calculation also makes use of the fixed flavour number scheme, assuming three active flavours in the proton (*u, d, s*). Heavy quarks are produced dominantely in the boson-gluon fusion. In addition, a small fraction of quark induced processes with the emitted gluon splitting into a $c\bar{c}$ pair is present. For the calculation the HERAPDF1.0 set is used. On top of the HVQDIS calculation, which yields complete four-vectors of the charm quarks produced, the quarks are fragmented into D^* according to the Kartvelishvili fragmentation function. To obtain the central values for the D^* cross section, both scales are set to $\mu_R = \mu_F = \mu_0 = \sqrt{Q^2 + 4m_c^2}$ and the charm mass is set to $m_c = 1.5$ GeV. The fragmentation is calculated with the parameter α chosen according to the measurement [A$^+$09]: $\alpha = 3.3^{+0.4}_{-0.4}$ for $\hat{s} > 70$ GeV^2 and $\alpha = 6.0^{+1.1}_{-1.3}$ for $\hat{s} < 70$ GeV^2. The notation $\hat{s}$ stands for the centre-of-mass energy of the $c\bar{c}$ pair. To estimate the theoretical uncertainties the input parameters are varied as follows:

- the charm mass is varied from $m_c = 1.35$ GeV to $m_c = 1.65$ GeV.
- the renormalization and factorization scales are varied simultaneously from $0.5\mu_0$ to $2\mu_0$.

The resulting uncertainties are added in quadrature and are correlated.

1.5. Event Generators and Detector Simulation

A measurement of the physical quantities like cross sections requires corrections due to the detector response. This includes the limited acceptance and efficiency as well as the influence of the resolution of the detector components. The treatment of these aspects constitutes the main task for the Monte Carlo simulations since it is difficult to determine these corrections for a complete physics analysis just from data. Monte Carlo simulations are also used in developing the selection criteria, by helping to determine which variables are particularly useful for separating signal from background. Where simulations and data disagree the MC simulation is tuned to model the data behaviour in several ways. Where the detector response is concerned, the relevant parts, for example the material distributions, can be determined directly from data and then implemented in the simulation. If the differences between data and Monte Carlo arise from simulation of the underlying physical processes on the generator level, one can either try varying the parameters (the fragmentation, for example) or change the physical input for the simulation. When using a Monte Carlo simulation for correction of the measured quantities to the detector response, it is common practice to reweight the Monte Carlo events with respect to the generated distributions in order to describe the data.

The Monte Carlo generator RAPGAP [Jun95] performs calculations of charm production in *ep* scattering in the massive scheme in leading order pQCD. Higher order corrections within the hard interaction part are implemented via initial state (proton side) and final state (heavy quark side) parton showers. For the parton evolution RAPGAP uses the DGLAP formalism where the PDF set HERAPDF1.0 at the starting scale is used for this analysis. The RAPGAP version used is 3.1. The renormalization and the factorization scale for RAPGAP has been set to $\mu_R = \mu_F = \mu_0 = \sqrt{Q^2 + p_\perp^2}$. The charm quark mass is set to $m_c = 1.43$ GeV. For the fragmentation of the light quarks the Lund String model is used, whereas for the fragmentation of the heavy quarks the Bowler fragmentation has been used. The initial and final state QED radiation in LO, i.e., single photon emission off the lepton line, as well as virtual electroweak corrections were considered via an interface with HERACLES [KSM92].

The detailed simulation of the detector response is contained in the H1SIM package [Mey89] which is based on the GEANT3 program [BBM+87]. The simulation contains information like the generation of hits in the tracking chambers as well as showers in the calorimeters. Inflight decays of the instable hadrons and production of new particles by interactions with the material are also considered. The parameters used in this program were determined in test beam measurements and optimized during *ep* data taking. For the

reconstruction the data and the simulated events pass through the same program H1REC [Col08].

Chapter 2: HERA and the H1 Detector

The electron[1]-proton storage ring HERA [Wol] was in operation between 1992 and 2007 at the DESY laboratory located in Hamburg, Germany. There were four interaction points at HERA: H1 and ZEUS (general purpose experiments), and HERMES and HERA-B (fixed target experiments). The analysis presented in this thesis was done with data collected by the H1 experiment. In this chapter, the main features of the HERA ring and a general description of the H1 detector are presented.

2.1. HERA

HERA consisted of two independent rings designed to accelerate and store electrons or positrons and protons in a tunnel 6.3 km in circumference. In the Figure 2.1 the layouts of the HERA accelerator and of the injection system are shown.

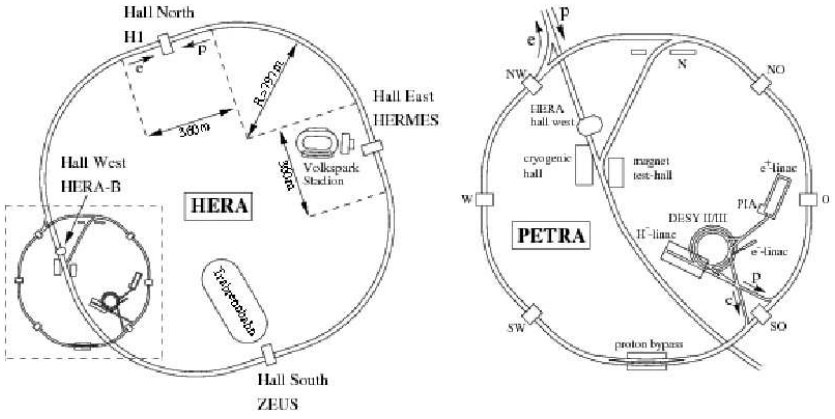

Figure 2.1: Schematic view of the HERA collider: the main HERA ring (left) and the pre-accelerator system (right).

Before injection into the HERA ring the electrons and protons were first passed through a chain of pre-accelerators. Negatively charged hydrogen ions were accelerated in a 50 MeV linear accelerator and then stripped of their electrons in order to get the protons which were afterwards injected into DESY III. The protons were accelerated to 7.5 GeV before being transferred

[1]The term 'electrons' refers to both electrons and positrons

to PETRA III. There they were accelerated to 40 GeV and then injected into the main HERA ring. The proton current achieved was of approximately 100 mA.

Electrons were first brought up to 500 MeV in a linear accelerator, then injected into a small storage ring. There they were allowed to accumulate in a single bunch of 60 mA before being injected into DESY II and then accelerated to 7 GeV. Afterwards, the bunch was transferred to the PETRA II ring, with this stage being repeated at a rate of 12.5 Hz until 70 bunches have been filled. The bunches were then injected into the HERA ring. This procedure was carried out three times with a resulting electron current of approximately 30 mA being achieved.

Some bunches were left empty such that a proton or an electron bunch may arrive in the detector with no collision partner. These unpaired 'pilot' bunches were used to estimate the rates of background processes such as beam interactions with the residual gas in the beam pipe and collisions with the beam pipe wall.

During the 1999 and 2000 running periods, 27.6 GeV positrons were brought into collision with 920 GeV protons, providing a center-of-mass energy $\sqrt{s} \approx 318$ GeV and a time of 96 ns between bunch crossings.

2.2. The H1 Detector

The H1 detector [A$^+$97a], [A$^+$97b] was a general purpose 4π detector measuring both the scattered electron and the final hadronic state produced by the scattered quark and proton remnant. Due to the energy imbalance of the colliding particle beams, the H1 detector was forward-backward asymmetric in design. The forward region of the detector was instrumented to measure the large energy flows and particle multiplicities emerging in the proton direction. The backward region was designed to provide an accurate measurement of the scattered electron energy and momentum which are important in determining the event kinematics.

The H1 detector consisted of several components, layered around the interaction point. A three dimensional view is shown in Figure 2.2.

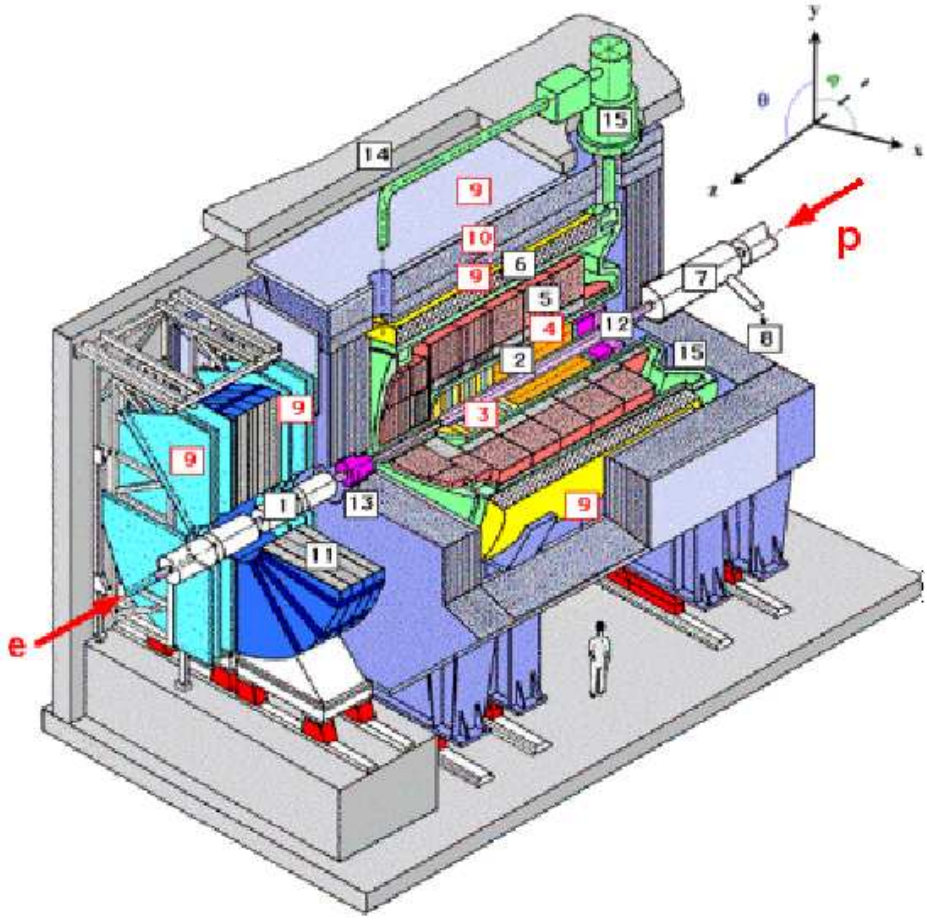

1	Beam pipe and beam magnets
2	Central tracking device
3	Forward tracking device
4	Electromagnetic LAr calorimeter
5	Hadronic LAr calorimeter
6	Superconducting coil
7	Compensating magnet
8	Helium supply for 7
9	Muon chambers
10	Instrumented iron yoke
11	Forward muon toroid
12	Backward electromagnetic calorimeter
13	PLUG calorimeter
14	Concrete shielding
15	Liquid argon cryostat

Figure 2.2: A three-dimensional view showing the layout of the H1 Detector. The components are indicated by numbers on the picture.

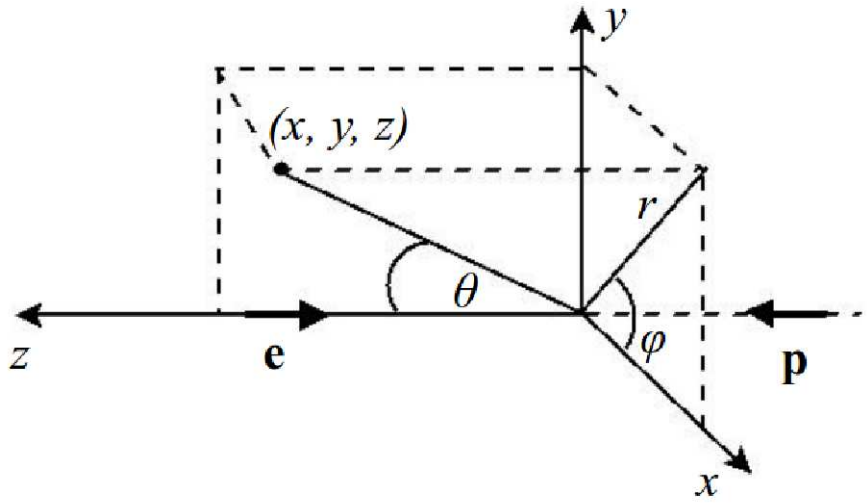

Figure 2.3: The coordinate system at H1

The beam pipe was surrounded by the tracking detectors which were followed by the calorimeters. The superconducting solenoid enveloped the latter. It provided the magnetic field of ~ 1.15 T needed to measure particles' momenta with the tracking detectors. The whole apparatus was surrounded by an iron yoke to return the magnetic flux of the solenoid. The iron yoke was instrumented and used as a central muon detector.

The z axis of the right-handed H1 coordinate system, illustrated in Figure 2.3, was defined by the beam axis with positive values in the direction of the proton beam. The x axis pointed towards the center of the HERA ring and the y axis pointed perpendicular upwards. The origin of the coordinate system was the nominal interaction point. The azimuthal angle ϕ laid in the xy plane and the polar angle θ was measured from the z axis.

The luminosity measurement was based on the Bethe-Heitler process [BH34], for which the cross section can be calculated precisely by the quantum electrodynamics framework (QED), and was performed with a dedicated detector system.

2.3. Central Tracking Detectors

The central tracking system was composed of the central silicon tracker (CST), the central inner z chamber (CIZ), the central inner proportional chamber (CIP), the central outer z chamber (COZ), the central outer proportional chamber (COP) and the central jet chamber (CJC). A schematic view of the entire tracking system is presented in Figure 2.4.

The main tracking device was the CJC, which consisted of two coax-

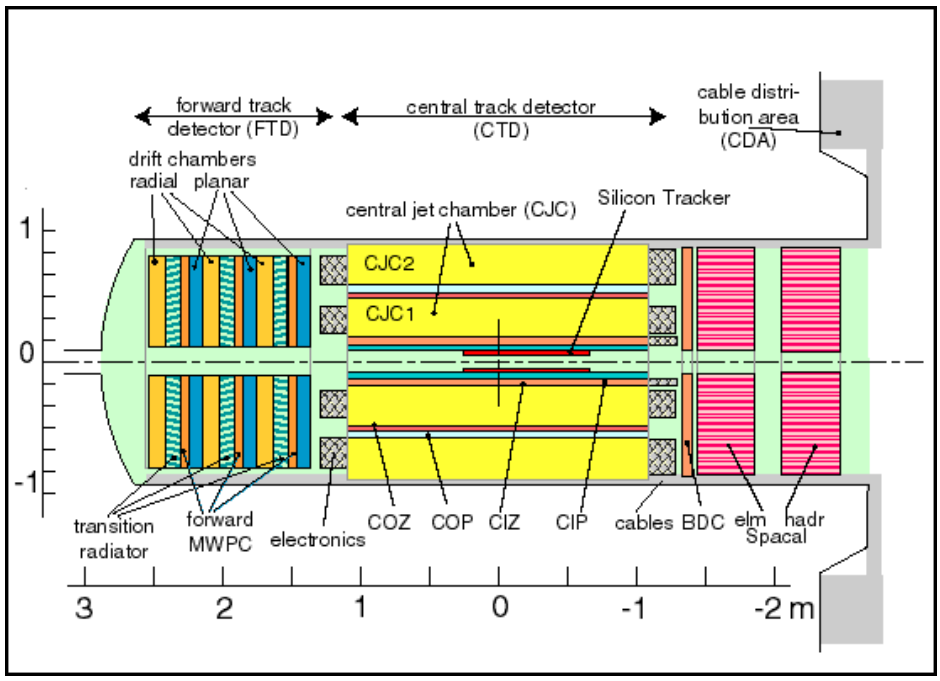

Figure 2.4: The H1 Tracking system $(r-z)$ view.

ial cylinders filled with gas, and was positioned along the beam axis from z = -1.1 m to z = + 1.1 m. The inner cylinder (CJC1) covered the angular range $11^o < \theta < 169^o$ and the outer cylinder (CJC2) covered $26^o < \theta < 154^o$. Both chambers had their wires strung parallel to the beam axis and the drift cells were inclined with respect to the radial direction in the (r, ϕ) drift plane. Charged particles traversing the CJC ionized the CJC gas. The released electrons drifted towards the wires and caused an electron cascade, driven by the electric field between the wires. The drift velocity and the time at which the charge collected by the wires was measured defined the position of hits in the (r, ϕ)-plane. The charge was read at both ends of the wires. The space point resolution in the drift plane was 170 μm, and by comparing the signals read from both ends of the wires a resolution of 1% of the wire length in z was achieved.

To further improve the z-resolution, hits in CIZ and COZ were also taken into account in the track reconstruction. They were located inside the CJC1 and in between the CJC1 and CJC2, respectively. Their signal wires were perpendicular to the z axis, resulting in a z-resolution better by two orders of magnitude compared to the CJC alone.

The central silicon tracker (CST) was the innermost track detector. It consisted of two layers with a polar coverage of $30^o < \theta < 150^o$. In the (r, ϕ) plane a hit resolution of $\sigma_{r\phi} = 12$ μm was achieved. Including the

precise CST (r, ϕ) hits in the track fit improved the transverse momentum resolution due to the good hit resolution and due to the extension of the measured arc length in the (r, ϕ) plane.

The central inner and the central outer proportional chambers (CIP and COP) didn't have any influence on the final track measurement. Together with the forward proportional chamber (FPC) they performed a fast measurement of the z position of the interaction point at first trigger level. Like in the CJC, the wires in CIP and COP were parallel to the z axis. Each of these two chambers contained two layers. CIP (COP) was divided in 8 (16) azimuthal ϕ sectors and in 60 (18) pads of 36 (120) mm each in the z direction. The two CIP layers were rotated by $\pi/16$ in ϕ with respect to each another, thus halving the eightfold segmentation of each chamber at the trigger level by requiring coincidences of the two planes.

In the forward region of the H1 detector the forward tracking detectors (FTD) and the forward proportional chambers (FPC) were located. Information from the FTD was not used in this analysis because the track information obtained with it was worse qualitatively than the information from the central tracking system. One reason for this was the multiple scattering of the particles in the region between the interaction point and the forward tracking detectors. The forward proportional chamber was used together with CIP and COP to gather rapid information about the position of the interaction vertex.

2.4. Track Reconstruction

The solenoid generated a longitudinal magnetic field in the central tracking system and bent the tracks of the charged particles. The trajectory of a charged particle was ideally approximated by a circle in the (r, ϕ) plane and by a helix in three dimensions. The five parameters of the helix were afterwards determined:

- the signed curvature parameter $\kappa = \pm r^{-1}$ of the track in the (r, ϕ) plane,
- the signed distance of closest approach d_{ca} of the track to the z axis in the (r, ϕ) plane,
- the azimuthal angle ϕ of the track in the point of closest approach: the angle between the x direction and the transverse momentum (tangent to the helix) in the (r, ϕ) plane in the point of closest approach,
- the polar angle θ in the point of closest approach: the angle between the z direction and the momentum in the point of closest approach
- z position z_{ca} of the track in the point of closest approach.

The sign of the κ parameter was positive when the particles were moving in the (r, ϕ) plane projection in the anticlockwise direction from the point of closest approach. This was a negatively charged particle. The transverse momentum of the track was directly correlated to the curvature parameter κ of the helix in the (r, ϕ) plane: $\kappa \propto 1/p_\perp$. The sign of the d_{ca} parameter was positive when the vector from the origin to the point of closest approach, the momentum vector in the (r, ϕ) plane and the positive z axis made a right-handed system.

The first three parameters were determined from the fit of the projection of the track in the (r, ϕ) plane to a circle. The polar angle θ and the z position z_{ca} of the track resulted from a subsequent fit in the (r, z) plane.

Due to the fact that the real interaction point, which is relevant for the physical observation, usually differs from the nominal interaction point, in addition to the variables d_{ca} and z_{ca}, that depend on the origin of the coordinate system, the variables dependent on the real interaction vertex d'_{ca} and Δz_0 were also defined:

- d'_{ca} is the signed distance of closest approach of the track to the reconstructed interaction point in the (r, ϕ) plane

- $\Delta z_0 = \delta_{ca} - z_{rec\,vtx}$, where δ_{ca} is the difference between the z coordinate of the point of closest approach and the nominal interaction vertex, and $z_{rec\,vtx}$ is the z position of the reconstructed vertex.

For tracks fitted to the reconstructed vertex, these variables vanish by definition. Therefore, when the quality of these tracks was evaluated, the values of d'_{ca} and Δz_0 were used, which were determined for a track with the same hits in the tracking detectors as the evaluated track, but which was not fitted to the reconstructed interaction point.

The track reconstruction algorithm has been modified for the most recent offline reconstruction program. It takes into account the effects of the sources that can spoil the ideal form of a circle in the (r, ϕ) plane or of a straight line in the Sz plane[2], like multiple scatterings in the material (which manifest in sudden changes of direction) and energy loss in the material (which affect the curvature of the track) by using a broken-line fit. The new track reconstruction also comprises with a more robust treatment of the outliers (hits that are far from the reconstructed track) in a reasonable amount of time. More details can be found in [Blo].

[2]S is the distance in the xy plane

2.5. Calorimeters

The Liquid Argon calorimeter (LAr) [A$^+$93] enclosed the forward and the central part of the detector, covering the polar angular range $4^o < \theta < 154^o$. It was a sampling calorimeter with absorbers of lead in the inner electromagnetic and of stainless steel in the outer hadronic part. Altogether it had more the 44 000 readout channels, called calorimeter cells.

The LAr was a non-compensating calorimeter, having on average a larger response to the electromagnetic compared to hadronic energy depositions. A software weighting algorithm was applied to correct for the electromagnetic shower fraction of energy depositions caused by the hadrons, examining shower shapes. Since the shape of low energetic hadronic depositions is irregular, for energy depositions below $\sim 7-10$ GeV in a specific cone weighting factors were applied without detailed analysis of the shower shape.

The reconstruction software provided energy measurements with and without this correction of hadronic energies. The *hadronic* energy level applied the individual hadronic weighting factor for each calorimeter cell. The *electromagnetic* energy level assumed the energy deposition to be purely electromagnetic and only corrections for dead material in front of the calorimeter were applied. Finally the cells were grouped into clusters.

An energy resolution of $\sigma(E)/E \sim 12\%/\sqrt{E/GeV} \oplus 1\%$ in the electromagnetic part and of $\sigma(E)/E \sim 50\%/\sqrt{E/GeV} \oplus 2\%$ in the hadronic part was achieved.

The spaghetti calorimeter (SpaCal) [A$^+$97c] was composed of a forward electromagnetic part and of a backward hadronic part, covering the polar angular range between 153^o and 177.5^o. The 1192 electromagnetic cells provided a fine granularity. The hadronic part had 136 cells. Both the hadronic and electromagnetic parts used the so-called spaghetti technology. A cell in the electromagnetic part had an area of 40.5 x 40.5 mm^2 and contained scintillation lead fibers strung parallel to the beam axis, whose ends were all tied together and were read by the same photomultiplier. Both the electromagnetic and the hadronic part had each an active volume of 25 cm deep, corresponding to 28 radiation lengths for the electromagnetic part and to 29 radiation lengths for the hadronic part.

The energy resolution of the electromagnetic part of the SpaCal was measured in test beams at CERN and DESY [N$^+$96] to be:

$$\frac{\sigma_{em}(E)}{E} = \frac{(7.1 \pm 0.2)\%}{\sqrt{E(GeV)}} \oplus (1.0 \pm 0.1)\% \qquad (2.1)$$

The calibration for high electron energies was performed by studying the energy spectrum of the scattered electrons reconstructed by the electron and

double angle methods[3]. The energy scale up to small energies can be verified by comparing the energy of the scattered electron cluster in SpaCal to the track in the backward silicon tracking detector [Eck02]. The energy resolution of the SpaCal was found to vary linearly from 1% at 2 GeV to 0.2% at 27.6 GeV ([Pet11]).

The energy resolution of the hadronic part of the SpaCal was measured in test beams at ITEP Proton Synchrotron in Moscow [eaHSG] to be:

$$\frac{\sigma_{had}(E)}{E} = \frac{(56.0 \pm 3.0)\%}{\sqrt{E(GeV)}} \tag{2.2}$$

The backward drift chamber (BDC) [Col], [Sch96] was positioned in front of the SpaCal. Together with the latter, it improved the precision of the scattered electron polar angle measurement. The BDC was divided in eight parts. One part consisted of four drift chambers with two scintillating fiber layers, each layer positioned along the z axis. The 2048 fibers of the BDC were strung perpendicularly on the beam pipe, such that a fast measurement of the radial drift direction could be made. This geometry optimized the resolution of the polar angle measurement. From outside inwards the distance between the fibers diminished, such that an uniform resolution of the polar angle was achieved. In order to allow the measurement of the azimuthal angle, the two layers were rotated by 11.5^o with respect to each other. The final resolution of the scattered electron polar angle is $\sigma_\theta = 2$ mrad.

2.6. The Trigger

Electron and proton bunches collided every 96 ns leading to a rate of 10.4 MHz. Since the rate of the physically interesting *ep* rates was much lower and the reading out of the total detector in 96 ns is not possible, fast hardware and software algorithms had to decide whether to keep an event or not. This was done by a sophisticated multilevel trigger system which selected the relevant *ep* events and reduced the background rates in several steps. The input rate decreased from about 100 kHz at the first level (L1) down to 50 Hz at the fourth level (L4). During the data taking periods 1999 and 2000 there were three trigger levels in use.

The L1 decision was based on special trigger signals from various detector components. There were 256 trigger elements logically combined in 192 subtriggers. An event was kept at L1 if at least one of the 192 subtriggers was giving a positive decision. To allow sufficient time to acquire the individual signals, they were first fed into a pipeline, bunch crossing by bunch crossing. The decision to keep an event came 24 bunch crossings later. The

[3]The electron and double angle methods are presented in Chapter 3.

pipelines were stopped if the decision was positive. Until the pipelines were restarted, so-called dead time accumulated in which no data could be collected. If a specific subtrigger had a too large rate, it was scaled down by a factor n. That means that only every n-th positive decision of this subtrigger was taken into account, effectively reducing the integrated luminosity seen by this subtrigger. The L1 output rate was of the order of a few kHz.

Neural networks and topological triggers were implemented on L2. Within 20 μs the decision had to be made whether to start the full detector readout or to reject the event and restart the pipelines. The L1 subtriggers selected in this analysis did not require an L2 condition to be fulfilled. The L2 output rate had to be below 50 Hz since L3 was not yet operational for the data analyzed here.

On the fourth trigger level an on-line event reconstruction was performed. This did not contribute further to the dead time since an asynchronous event buffer was used. If the L1 and the L2 decisions could be validated, the events were classified into L4 classes. They belonged to at least one of the physics event classes if they provided a "hard scale", e.g. a scattered electron with a sufficiently large squared momentum transfer (Q^2) or if specific final state finders selected them. All events assigned to physics classes were kept. The remaining events were downscaled. For the kept fraction of the downscaled events an according weighting factor was stored, the L4-weight. The maximal allowed decision time of L4 was 100 ms.

2.7. The Luminosity System

The luminosity was determined from the rate of the Bethe-Heitler process, $ep \to ep\gamma$. This process depends on the inner structure of the proton and can be computed precisely in the quantum electrodynamics (QED) framework. The cross section of the Bethe-Heitler process in the visible phase space of the H1 luminosity system is around 70 nb [Fav].

The luminosity system [Fav],[eaHC] was based on two dedicated detectors: the electron tagger for the detection of the scattered electrons and the photon tagger for the radiated photon. The kinematics of the Bethe-Heitler's process favors the electrons scattered inside the beam pipe. Therefore the electron tagger was located very close to the beam pipe and quite far from the interaction point (z = -33 m), in order to detect the electrons scattered at angles close to 180^o. Just like the beam electrons, the scattered electrons were also bent by the magnetic system which separated the beam electrons from the beam protons after the interaction point. The outgoing photon went straight to the photon detector centered on the proton beam axis at z = -103 m. A graphical overview of the luminosity system is shown in Figure 2.5 and the total luminosity recorded by the H1 experiment in the 2 runs are

shown in Figure 2.6.

The luminosity was calculated from the total rate R_{tot} of the bremsstrahlung events, R_0 is the rate for electron pilot bunches, I_{tot} and I_0 are the corresponding electron beam currents and σ_{vis} is the visible part of the Bethe-Heitler cross section with acceptance and trigger efficiency included:

$$L = \frac{R_{tot} - (I_{tot}/I_0)R_0}{\sigma_{vis}} \tag{2.3}$$

The event rate of pilot bunches allowed for a good estimate of the bremsstrahlung events coming from the interaction between the electrons and the residual gas in the beam pipe ($eA \rightarrow eA\gamma$), which is the main background for the Bethe-Heitler processes.

After the trigger selection, a complete off-line event reconstruction is performed and the output is stored on tapes. Using the knowledge obtained from previous technical studies and physics analyses, a new reprocessing of the recorded data was made recently[4], leading to improvements in the electromagnetic and hadronic calibrations and in the track reconstruction efficiency.

[4]The reprocessed files are available since year 2011.

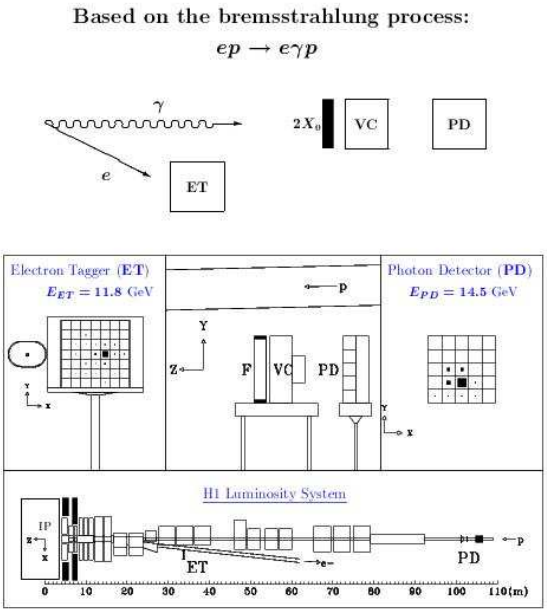

Figure 2.5: The layout of the luminosity system at H1 experiment.

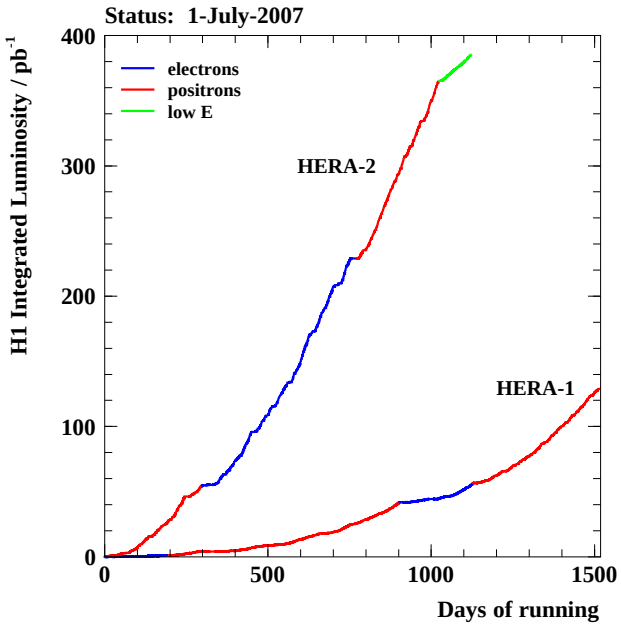

Figure 2.6: The total luminosity recorded by the H1 experiment in the 2 run periods

Chapter 3: Event Selection

In this chapter, the criteria used in the event selection are presented. The distributions of different observables in the data sample are compared with the Monte Carlo simulation.

3.1. General Event Selection

The data set analyzed in this thesis covers the period of HERA operating positron beams from the years 1999 and 2000 and corresponds to an integrated luminosity of 47.66 pb^{-1}.

A run is a short data taking period with constant readout and the trigger settings. The runs must fulfill the following conditions in order to be selected:

- The run quality has to be good or medium. It means that all major subsystems must be operational: the luminosity system, CST, CJC1, CJC2, LAr and SpaCal.
- The integrated luminosity of a run should be at least 0.1 nb^{-1}. If the collected luminosity in a run is lower, it is usually because of technical problems.
- The subtrigger 61 has to be on.

3.2. Online Selection

The selection of the data events is performed in two steps. In the first step, an online preselection is done during data taking. This step is based on a trigger decision which selects a certain class of physics events. In the second step, the final selection is done offline by applying analysis specific cuts.

The trigger used in this analysis, trigger 61, receives signals from several detector components. It is a level 1 trigger and it fires if the conditions formulated in terms of trigger elements are fulfilled. Trigger elements are the digital information that is sent from the individual subdetector triggers. Trigger 61 decides on the scattered electron, z vertex and track information:

$$(DCRPh\_THig \;\&\; zVtx\_sig \;\&\; (SPCL\_IET > 2 \mid SPCLe\_IET\_Cen\_3))$$

The scattered electron: $(SPCL\_IET > 2 \mid SPCLe\_IET\_Cen\_3))$. All electrons are triggered using the inclusive electron trigger (IET). The

condition for a scattered electron is an energy cluster deposit in the electromagnetic part of the SpaCal. The deposit must be of at least 6 GeV. There are also rules in place to discard the events in which the energy cluster deposits in the hadronic part of the SpaCal are higher than 0.6 GeV for the electron candidate cluster and 12 GeV in total. These requirements are a veto condition for the hadrons faking electrons.

***z* vertex**: $zVtx\_sig$. The z vertex information is obtained from CIP, COP and FPC. The trigger recognizes the tracks seen in these chambers and the information with all the intersections between these tracks and the z axis is provided as a distribution, which for real tracks, has a significant peak in one bin, whereas the number of entries in the other bins is randomly distributed.

Tracks: $DCRPh\_THig$. The information on tracks comes from the CJC. The DCRPh_THig requirement means that at least one energetic track, corresponding to a transverse momentum larger larger than 800 MeV, passes through these chambers. There are additional conditions coded to discard the events with high multiplicity of charged particles, thus reducing the non-*ep* background.

The subtrigger efficiency will be discussed in Chapter 4 as a function of the kinematic variables.

3.3. Offline Reconstruction of the DIS Events

The recorded events are subjected to the offline reconstruction and afterwards to an extended set of selection criteria to minimize the background contributions. The methods used and the constraints applied are detailed in the following subsections. The data distributions of the variables analyzed are compared with the distributions given by the Monte Carlo simulation. These comparisons are the so-called *control distributions*.

3.3.1. Reconstruction of the Kinematics

The first step in the reconstruction of the event kinematics is determining the interaction's primary vertex position. For an efficient event reconstruction, the primary vertex z position should be within 35 cm from the nominal interaction point. This restriction maximizes the rejection of the non-*ep* events, like beam-gas and beam-wall interactions, halo and cosmic muons. A comparison between the z position in data and the Monte Carlo simulation is shown in Figure 3.1.

At H1 several methods are used for reconstructing the kinematic variables, using the redundant information for cross checks and calibrations. The event kinematics can be reconstructed using the information just from the scattered electron measurement or from the hadronic final state measurement.

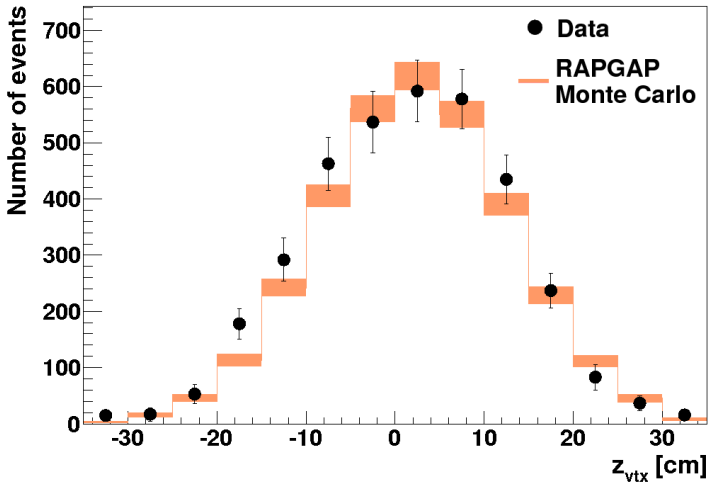

Figure 3.1: The comparison between data and Monte Carlo simulation for the z position of the primary interaction vertex. A good agreement between the data (black points) and the simulation (orange band) is observed. The error bars on the points and the width of the band represent the respective statistical uncertainties.

Electron method. This method is based on the measurement of the scattered electron only. The transferred momentum squared Q^2, the inelasticity y and the Bjørken-x are reconstructed using the energy of the incoming electron E_e, the energy of the scattered electron E'_e and the scattering angle of the electron θ_e:

$$Q^2_e = E_e E'_e (1 + \cos\theta_{e'}) \tag{3.1}$$

$$y_e = 1 - \frac{E'_e}{2E_e}(1 - \cos\theta_{e'}) \tag{3.2}$$

$$x_e = \frac{Q^2_e}{s \cdot y_e} \tag{3.3}$$

The resolution for y reconstructed using the electron method is given by:

$$\frac{\delta y_e}{y_e} = \frac{(1 - y_e)}{y_e} \left(\frac{\delta E'_e}{E'_e} \oplus \frac{\delta\theta_{e'}}{\tan(\theta_{e'})} \right) \tag{3.4}$$

and it degrades fast when $y \to 0$ because of the $1/y_e$ term. Another drawback of the method is the sensitivity to the initial state radiation (ISR) of a photon by the electron, as it lowers the energy of the beam electron available for the

interaction: $E_e = E_{\text{beam}} - E_\gamma$, influencing the reconstruction of high y values. The electron method is rather safe against final state radiation (FSR) of a photon by the scattered electron, because the photon cluster is merged with the scattered electron cluster. Both ISR and FSR influences are accounted for in the cross section calculation, as described in Subsection 4.1.3.

Sigma method. It is based on the longitudinal momentum conservation relation:

$$\sum_i (E - p_z)_i = 2E_e \tag{3.5}$$

where the sum runs over all the particles in the final state, including the scattered electron. The reconstruction of the event kinematics is done using both the scattered electron measurement and the hadronic final state measurement $\Sigma = \sum_i^{had}(E_i - p_{z,i})$, where the sum runs over all the particles measured in the final state, except the scattered electron.

$$y_\Sigma = \frac{\Sigma}{\Sigma + E'_e \cdot (1 - \cos\theta_{e'})} \tag{3.6}$$

$$Q^2_\Sigma = \frac{E'^2_e \cdot \sin^2\theta_{e'}}{1 - y_\Sigma} \tag{3.7}$$

$$x_\Sigma = \frac{Q^2_\Sigma}{y_\Sigma \cdot s} \tag{3.8}$$

The advantages of this method are the good resolution at low y and the low sensitivity to radiative corrections. The drawback is that it needs a very good measurement of the hadronic final state. The resolution in y reconstructed with the Σ method is given by:

$$\frac{\delta y_\Sigma}{y_\Sigma} = (1 - y_\Sigma)\left(\frac{\delta\Sigma}{\Sigma} \oplus \frac{\delta E'_e}{E'_e} \oplus \frac{\delta\theta_{e'}}{\tan(\theta_{e'}/2)}\right) \tag{3.9}$$

and it degrades slightly at larger y values due to particles emitted very close to the beam pipe.

Electron-Σ method. The $e\Sigma$ method for reconstructing the event kinematics was developed [BB95], such that one could reconstruct simultaneously the transverse momentum squared and the Bjørken-x with good resolutions and little dependence on the radiative corrections. In this method, the inelasticity y is obtained from:

$$y_{e\Sigma} = \frac{Q^2_e}{x_\Sigma \cdot s} \tag{3.10}$$

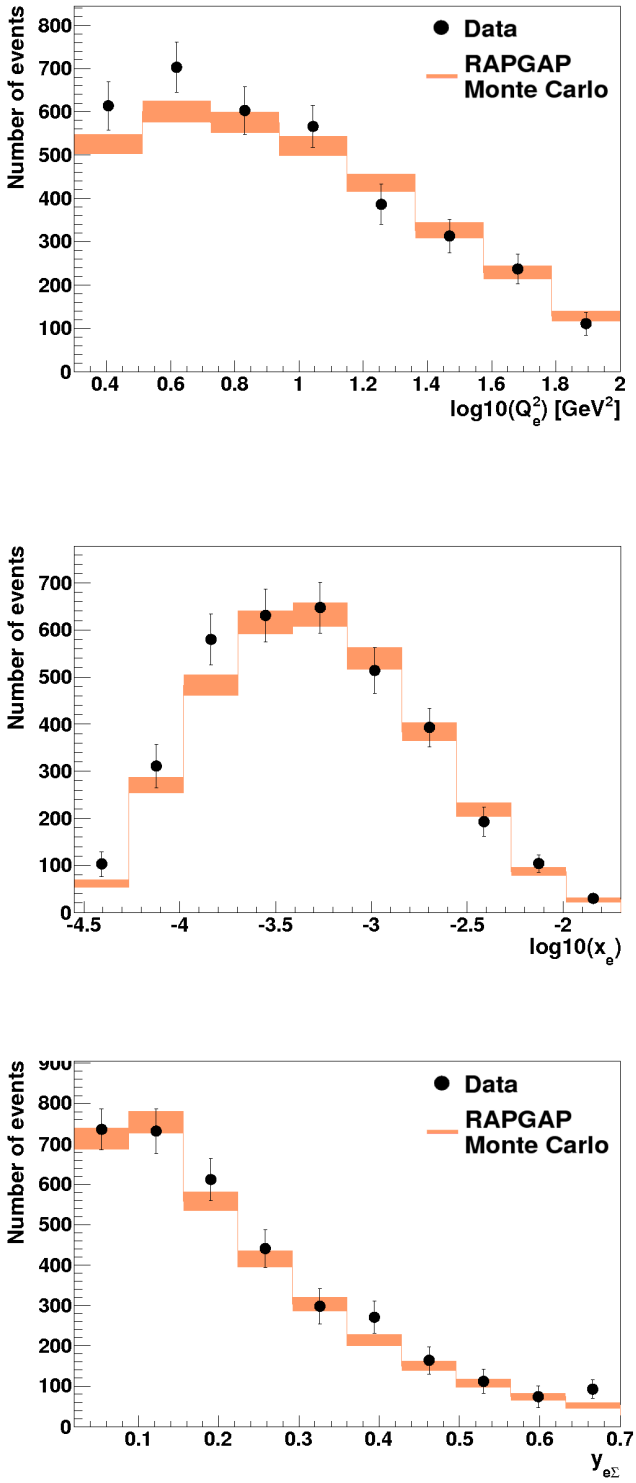

Figure 3.2: The data distribution (black points) and the Monte Carlo simulation (orange band) for Q^2, Bjørken-x and inelasticity y.

The ratio y_{rec}/y_{true} is compared for the three reconstruction methods, where y_{rec} is y and y_{true} is the y generated by the Monte Carlo program RAPGAP. The ratio y_{rec}/y_{true} is drawn in bins of y_{true} and then fitted with a Gauss function. The fitted value of the σ parameter for each method is plotted as a function of y_{true} and it is shown in Figure 3.3.

For this analysis, the Q_e^2 range is between 2 and 100 GeV^2 and the $y_{e\Sigma}$ range is between 0.02 and 0.7. The control distributions for Q_e^2, x_e and $y_{e\Sigma}$ are shown in Figure 3.2.

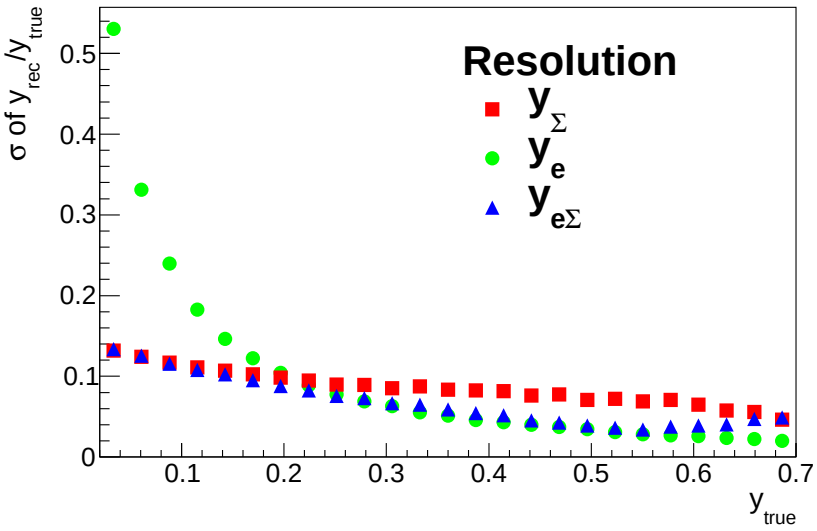

Figure 3.3: Resolution in y for different reconstruction methods as a function of true y derived from fitted distributions of the fraction y_{method}/y_{true} in each y_{true} bin.

Double angle. The double angle method uses the scattered electron polar angle and the polar angle γ which characterizes the hadronic final state. If the quarks are considered massless, then γ is the polar angle of the scattered quark. This method has low radiative corrections and doesn't depend heavily on the energy scales, but it has a low resolution at small y due to the particle losses in the beam pipe. The observables reconstructed with this method are used in calibration procedures of the electromagnetic and hadronic energy scales.

$$\delta_{had} = \sum_{i}^{\text{no. of hadrons}} E_i(1-\cos\theta_i) = E_{had} - p_{z\,had} \tag{3.11}$$

$$\cos\gamma = \frac{p_{t\,had}^2 - \delta_{had}^2}{p_{t\,had}^2 + \delta_{had}^2} \tag{3.12}$$

$$Q^2 = 4E_e^2 \frac{\sin\gamma(1+\cos\theta_e)}{\sin\gamma + \sin\theta_e - \sin(\theta_e+\gamma)} \tag{3.13}$$

$$x = \frac{E_e}{E_p} \frac{\sin\gamma + \sin\theta_e + \sin(\theta_e+\gamma)}{\sin\gamma + \sin\theta_e - \sin(\theta_e+\gamma)} \tag{3.14}$$

Due to the longitudinal momentum conservation relation 3.5, the $\sum_i (E-p_z)_i$ is expected to peak at ∼55 GeV if all particles are detected. In order to reject those events in which there are particles emitted close to the beam pipe and thus escaping detection, $\sum_i (E-p_z)_i$ is restricted between 40 GeV and 70 GeV. The distribution is shown in Figure 3.4.

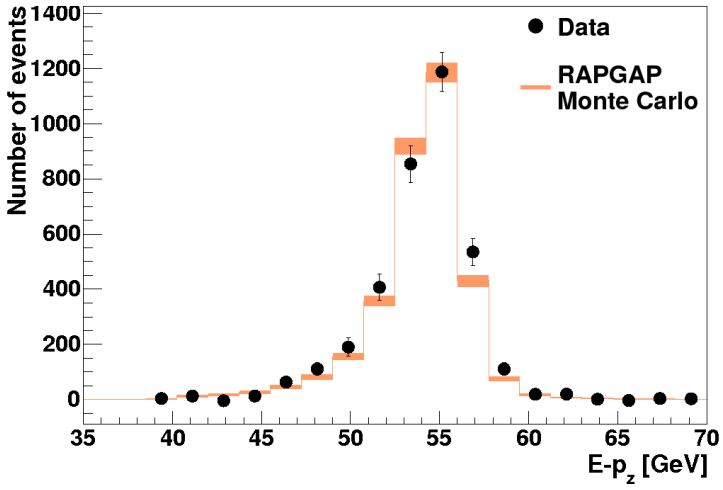

Figure 3.4: The comparison between data and Monte Carlo simulation for $E-p_z$. A good agreement between the data (black points) and the simulation (orange band) is observed. The error bars on the points and the width of the band represent the respective statistical uncertainties.

3.3.2. Scattered Electron Selection

Because the kinematics reconstruction is partially based on the measurement of the scattered electron, there are several criteria employed for an efficient electron identification. The information used in the reconstruction of the electron candidate is taken from SpaCal and BDC subdetectors.

The scattered electron produces showers in the electromagnetic part of the SpaCal. The cells with the energy depositions from the shower form a cluster, which is then used to calculate the properties of the electron candidate. If more than one candidate is found, then the one with the highest

transverse momentum is considered to be the scattered electron. The energy of the cluster has to be at least 8 GeV and a polar angle between 153^o and 177.8^o. The properties of the scattered electron, the energy, the polar and the azimuthal angles, are well described by the Monte Carlo simulation, as it can be observed in Figure 3.5.

A true scattered electron shower seldom extends into the hadronic part of the SpaCal. Therefore, the electron cluster position is restricted to the electromagnetic part by a cut in the radial position of the cluster, where x_{cluster} and y_{cluster} are the x and y coordinates of the electron cluster:

$$r_e = \sqrt{x^2_{\text{cluster}} + y^2_{\text{cluster}}} < 74\ cm$$

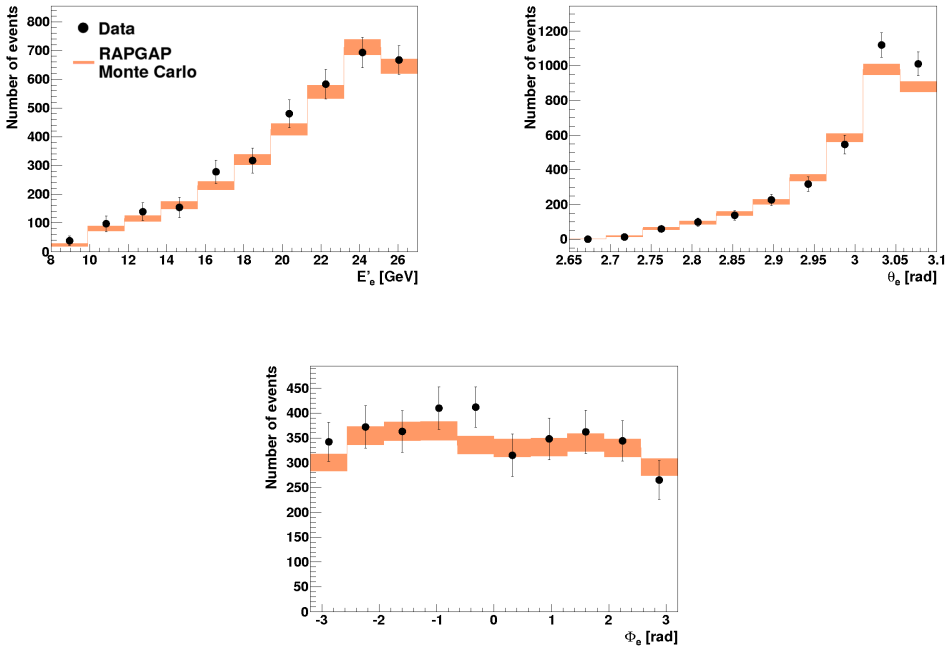

Figure 3.5: The properties for the scattered electron: the energy (upper left), the polar angle (upper right) and the azimuthal angle (bottom) in data and in the Monte Carlo simulation. Data is represented by the black points and the Monte Carlo simulation by the orange band. Statistical uncertainty is represented by error bars for data and by width of the band for Monte Carlo.

Also, the amount of energy deposited in the hadronic SpaCal is limited by two requirements: it should not exceed 500 MeV and it should not be more than 3% of the total energy of the electron cluster. These two requirements help differentiating the electron shower from hadronic showers, as the latter deposit more energy in the hadronic part of the calorimeter. Also, the cluster radius is larger for hadrons than for electrons. The electron shower doesn't have an uniform deposition in the calorimeter cells, so the cluster radius is calculated by using the logarithm of the ratio between the cell energy and the cluster energy as a weight for the cell position:

$$w_i = max\left(0, w_0 + ln\frac{E_i}{\sum_i E_i}\right)$$

$$\overrightarrow{r} = \frac{\sum_i w_i \overrightarrow{r_i}}{\sum_i w_i}$$

$$E_{\mathrm{cra}} = \sqrt{\frac{\sum_i \tilde{w}_i \left(\overrightarrow{r_i} - \overrightarrow{r}\right)}{\sum_i \tilde{w}_i}}$$

where $\overrightarrow{r}$ is the cluster position as a weighted sum over the positions of all cells, with the weight functions w_i [Gla98]. E_{cra} denotes the size of the cluster and it is restricted to 4 cm:

$$E_{cra} < 4\ cm.$$

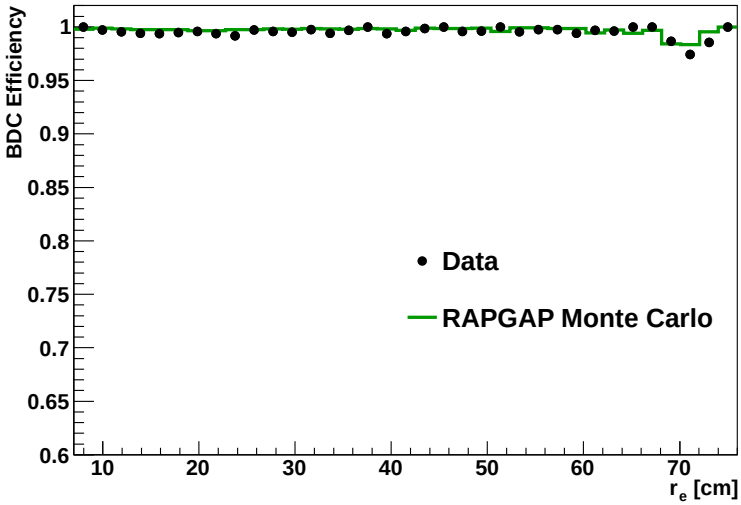

Figure 3.6: The efficiency of the BDC extrapolation cut as a function of the radial position r_e of the scattered electron cluster. The Monte Carlo simulation (solid line) gives a good description of the data points (black points). The efficiency is flat and close to 100%.

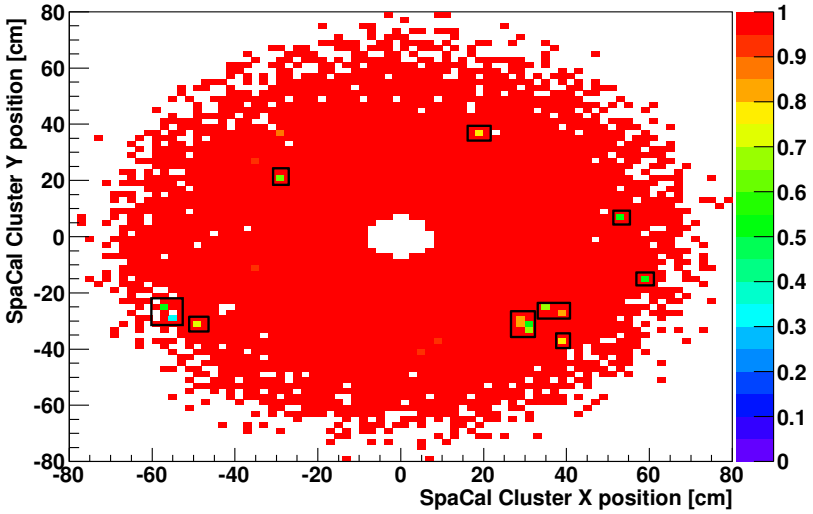

Figure 3.7: SpaCal efficiency. The red color corresponds to 100% efficiency, while lighter shades correspond to lower efficiencies. The inefficient regions are highlighted with black rectangles.

The inner part of the SpaCal is shielded from the beam pipe by a layer of tantalum (see Figure 3.8). This layer is called the VETO layer. If the scattered electron is emitted under a large angle and enters close to the beam pipe, a part of its energy will be deposited in the VETO layer cells and another part will leak into the beam pipe. Due to this leakage, the energy of the electron will not be fully reconstructed. This type of events is rejected in the analysis by requiring that the energy in the VETO layer is less than 2 GeV. Also, all the events with clusters in a radius of 8.7 cm from the beam pipe are discarded.

The electron and the proton beam are not parallel to one another and are not exactly parallel to the z axis of the coordinate system. This can lead to a shift of the actual cluster position closer to the beam pipe than it is read from the SpaCal geometry alone. This effect is corrected for by requiring that:

$$|(z_{SpaCal} - z_{vertex}) \cdot \tan\theta_e| > 9.1\ cm$$

In order to improve the resolution of the electron's azimuthal angle measurement, BDC conditions are also applied. At least 4 hits in the BDC have to be used in the reconstruction. In addition, the distance between the SpaCal cluster and the electron cluster in the BDC shouldn't be larger than 1.5 cm. In this way, the background consisting of the photons originating from the π^0 decays is rejected. The efficiency of this cut as a function of the radial position of the cluster in SpaCal is close to 100% and it is shown in

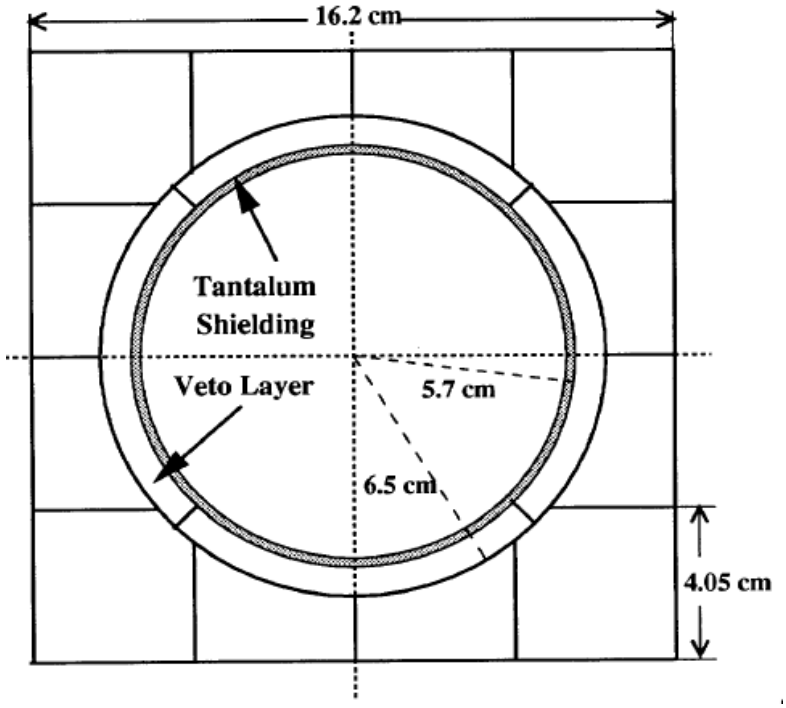

Figure 3.8: The (x,y) view of the SpaCal inner cells and the VETO layer

Figure 3.6.

The efficiency of some regions in SpaCal can drop due to possible malfunctions of the cables and the trigger. In order to identify the inefficient regions, the efficiency of the SpaCal part of the trigger is evaluated in SpaCal x-y bins. In Figure 3.7, the few inefficient cells are represented by green shaded boxes and are marked by black rectangles. The events recorded in the areas in which the trigger efficiency of the SpaCal part drops below 80% are discarded during the selection of both data and Monte Carlo events.

3.4. Selection of $D^{*\pm}$ candidates

The D^* mesons are reconstructed in the decay channel:

$$D^{*\pm} \to \pi_s^{\pm}\, D^0 \to \pi_s^{\pm}\, K^{\mp}\, \pi^{\pm}.$$

The difference between the $D^{*\pm}$ [1] mass and the D^0 mass is 145.4 MeV, leaving very little energy for the pion from the decay of D^*, therefore the label of 'slow pion'. By subtracting the $K\pi$ invariant mass from the $K\pi\pi_s$ invariant mass, $\Delta M = m(K\pi\pi_s) - m(K\pi)$, the resolution of the resulting distribution is much better than the resolution of the separate invariant mass distributions.

[1] In the following, D^* refers to both D^{*+} and D^{*-}

A set of quality requirements is applied, to ensure a good reconstruction of the D^* candidate and the reduction of the background.

3.4.1. Track selection

Only those tracks are selected, which are fitted to the primary vertex and fulfill a set of general criteria, which are summarized in Table 3.1. The tracks passing this general set are called 'good tracks'.

Variable	Condition
p_T	> 0.07 GeV
$\lvert dca' \cdot \sin\theta \rvert$	< 2 cm
R_{start}	≤ 50 cm
R_{length}	≥ 10 cm if $\theta \leq 150^o$
R_{length}	≥ 5 cm if $\theta > 150^o$
N_{CJC} hits	≥ 0

Table 3.1: 'Good track' selection criteria refer to the transverse momentum of the track p_T, the distance of closest approach dca', as defined in Chapter 2, the polar angle of the track θ, the radial position of the first hit of the track R_{start}, the radial length of the track R_{length}, the number of the hits in the two CJCs used in the reconstruction of the track N_{CJC} hits.

These conditions are tightened further to select tracks with a better quality. A summary of these cuts is given in the Table 3.2.

The p_T distributions for the kaons and the pions are shown in Figure 3.9. There is a good agreement between data and Monte Carlo in all distributions. The track of the π_s candidate curls in the CJC and dedicated studies for low-p_T tracks [Bri10] have shown that the behaviour of this kind of tracks is well understood down to $p_T = 0.12$ GeV. For more energetic charged particles, like the D^0 decay products, the required minimum transverse momentum is 0.25 GeV. An additional constraint for these decay products is applied, $p_T(K) + p_T(\pi) > 2$ GeV, to reduce the combinatorial background from the $K\pi$ pairs with a low p_T pion candidate.

The selected tracks should be reconstructed from at least 10 hits in the central jet chambers. The higher the number of hits, the smaller the uncertainty on the track's parameters. The description of this number is a good test of the detector simulation software. There is a reasonable agreement between data and Monte Carlo, as it can be seen in Figure 3.10, left.

Variable	Condition	Daughter
p_T	> 0.12 GeV	π_s
	> 0.25 GeV	K, π
$p_T(K) + p_T(\pi)$	> 2 GeV	K, π
$\|dca'\|$	< 1 cm	K, π, π_s
R_{start}	< 30 cm	K, π, π_s
R_{length}	> 10 cm	π_s
	> 18.9 cm	K, π
N_{CJC} hits	> 10	K, π, π_s
dE/dx likelihood	$> 1\%$	K, π, π_s

Table 3.2: Selection criteria for the tracks in the current analysis. The dE/dx likelihood is the probability of the particle identification, obtained from the energy loss behaviour.

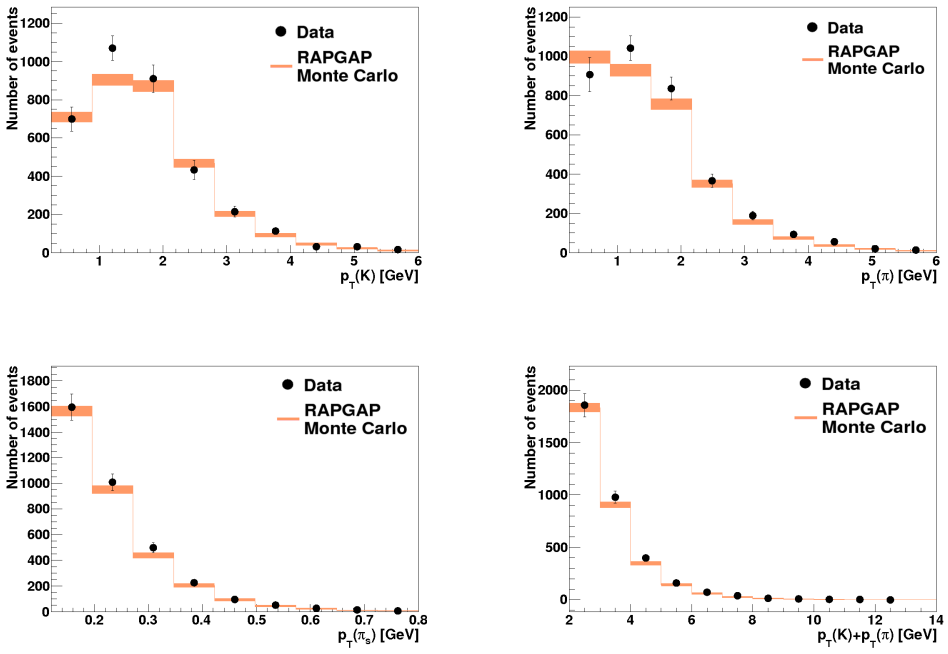

Figure 3.9: Transverse momenta of the daughters. The black points represent data, the orange band represents the RAPGAP Monte Carlo simulation.

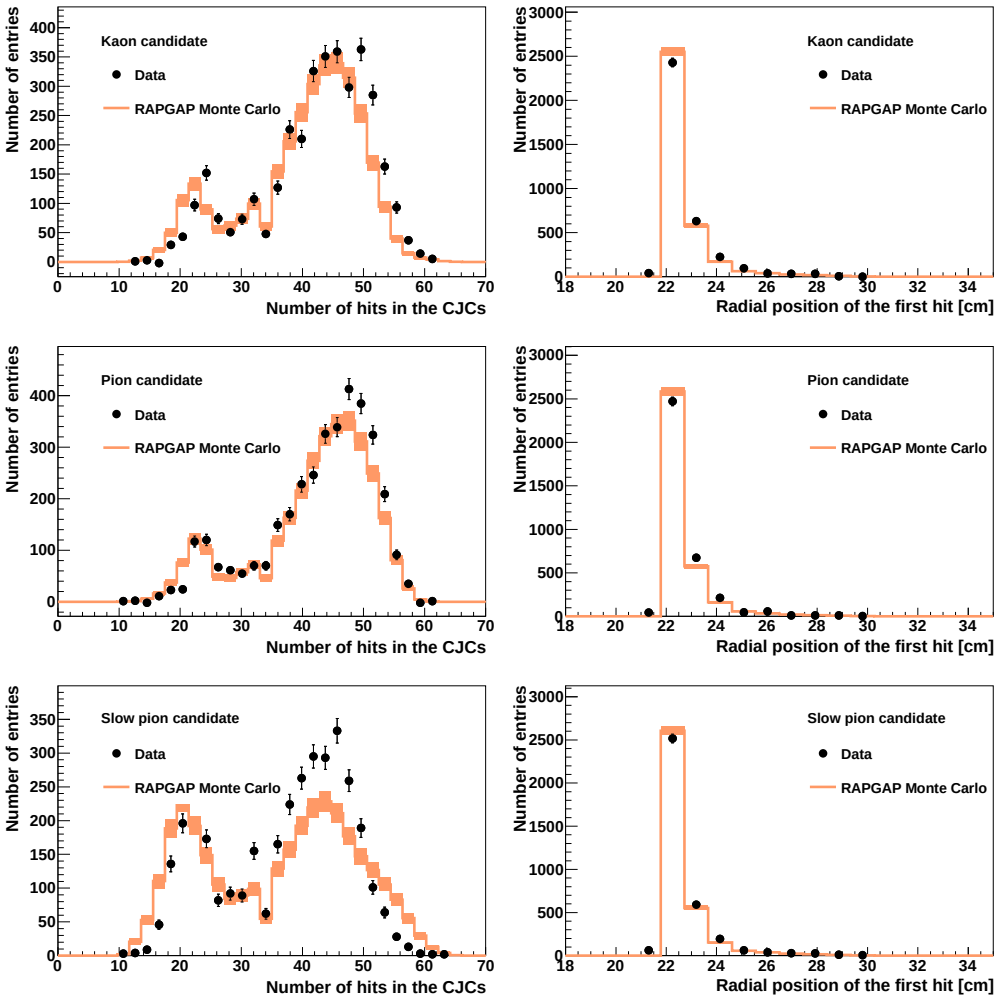

Figure 3.10: Number of CJC Hits (left) and the radial position of the first hit of the track (right). Black points are data, the orange band is the Monte Carlo simulation.

The selected tracks are required to start no further than 30 cm from the z axis. This condition ensures that the tracks considered start in the inner central jet chamber. The radial starting position of the track R_{start} in data is well described by the Monte Carlo simulation (see Figure 3.10, right).

If the tracks leave the CJCs before they reach a sufficient length for a good reconstruction, the radial length of the track is less than 10 cm for the slow pion and less than 19 cm for the kaon and the pion. The comparison between data and the Monte Carlo simulation is shown in Figure 3.11, left.

The range of the dca' of the track is further constrained, to reduce the contribution from the tracks originating from other sources than the primary vertex, like beam pipe interactions or cosmic rays. The Monte Carlo simulation gives a good description of this observable, shown in Figure 3.11, right.

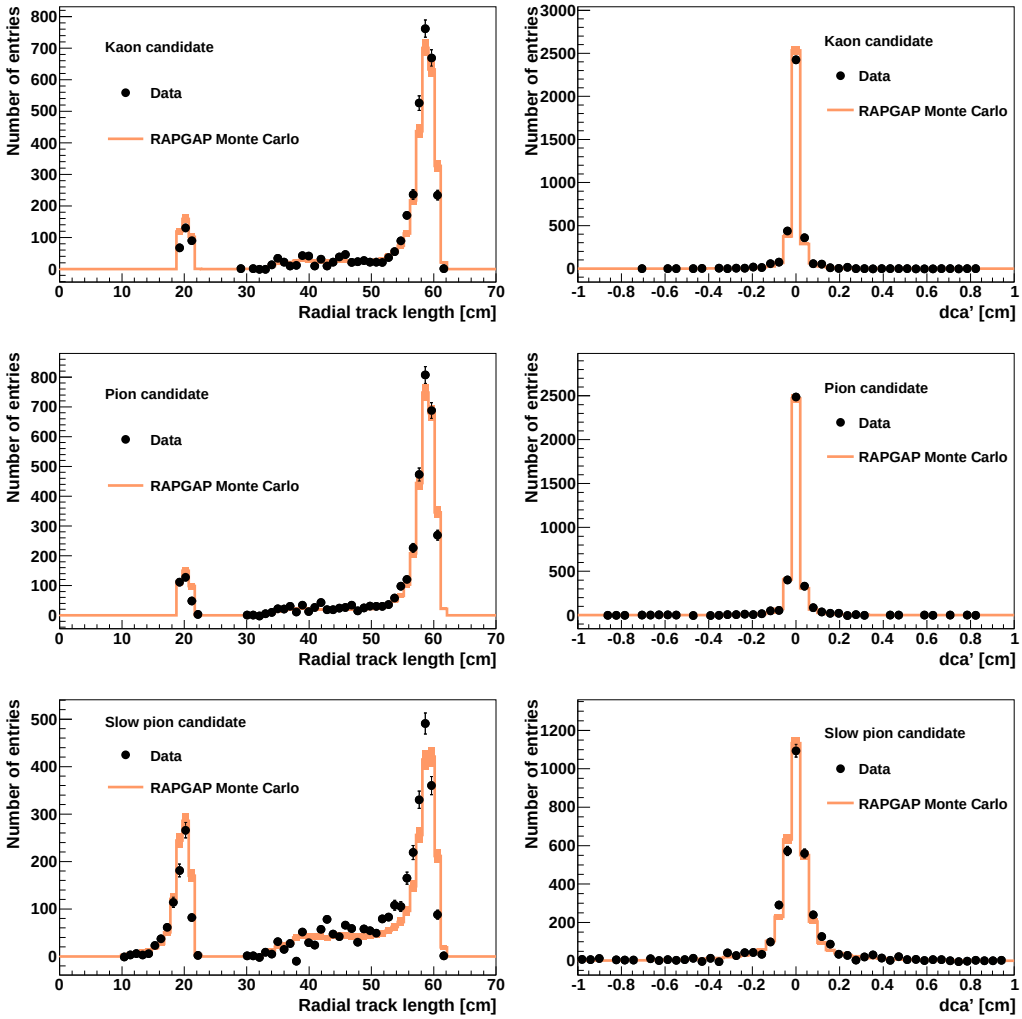

Figure 3.11: Radial track length (left) and the distance of closest approach (right). Black points are data and orange band represents Monte Carlo simulation.

3.4.2. The reconstruction of the D^* meson

The D^* meson candidate is reconstructed from charged kaon and charged pion candidate tracks. First, a kaon candidate and a pion candidate are selected, each having a transverse momentum of at least 250 MeV. The invariant mass of the $K\pi$ pair is required to agree within 80 MeV with the mass of the D^0 meson quoted by the Particle Data Group [N$^+$10], 1.86 GeV. Both opposite-sign $K^{\pm}\pi^{\mp}$, and same-sign $K^{\pm}\pi^{\pm}$, pairs are kept. The opposite-sign pairs are denoted *right charge* combinations. The same-sign pairs are called *wrong charge* combinations. When plotting the invariant mass of the wrong charge $K\pi$ pairs, it can be noticed that the distribution mimicks the light flavour background (see Figure 3.12).

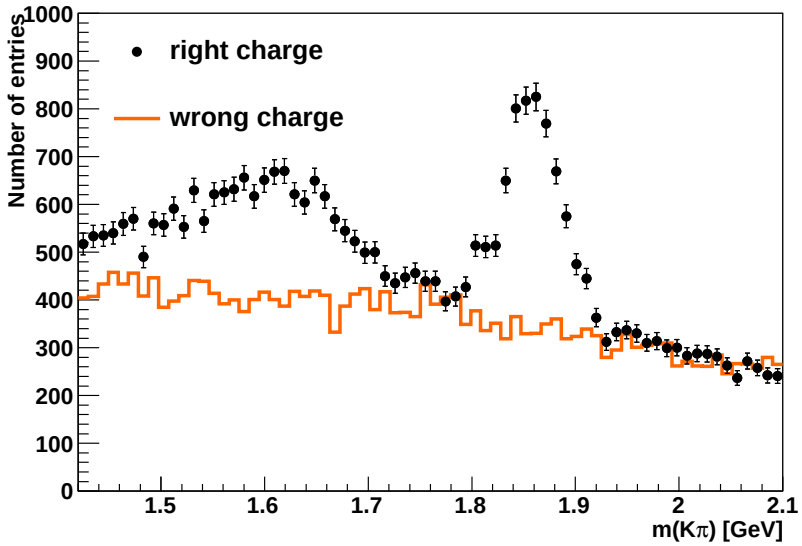

Figure 3.12: Invariant mass of the candidate $K\pi$ pairs in data. The right charge combinations are represented by black points and the wrong charge combinations are represented by the orange line.

A second pion is selected, whose transverse momentum is larger than 120 MeV. The D^* meson candidate is selected using the mass difference method [F$^+$77] between the invariant mass of the $K\pi_1\pi_2$ combination and the invariant mass of the $K\pi_1$ pair:

$$\Delta M = m(K\pi_1\pi_2) - m(K\pi_1)$$

The difference ΔM is required to be smaller than 170 MeV. The ΔM distribution in data is plotted for right charge and wrong charge combinations in Figure 3.13. There is a clear peak around 143 MeV in the right charge

distribution. The wrong charge distribution gives a good description of the light flavour background.

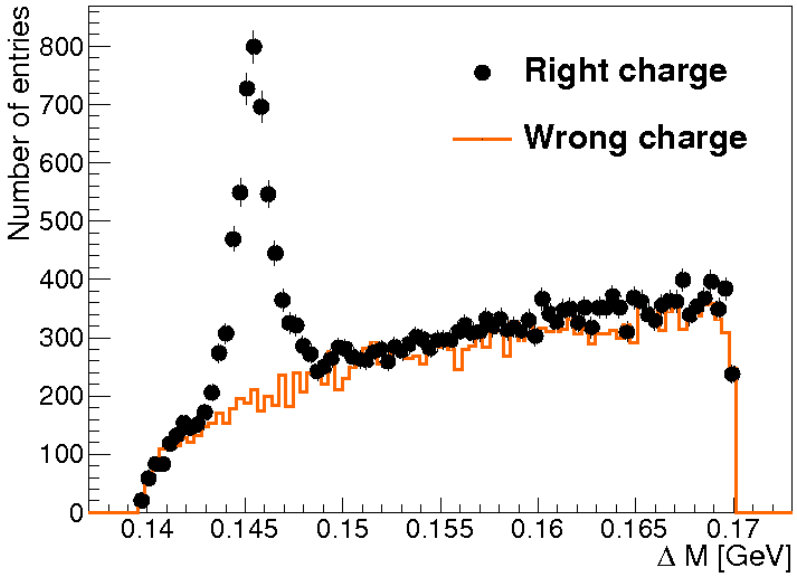

Figure 3.13: The invariant mass difference ΔM. The right charge combinations are represented by black points and the wrong charge combinations are represented by the orange line.

The *pseudorapidity* of the D^* candidate is defined as:

$$\eta(D^*) = -ln\, tan\frac{\theta(D^*)}{2} \tag{3.15}$$

where $\theta(D^*)$ is the polar angle of the D^* candidate. The visible phase space is restricted by the detector acceptance to $p_T(D^*) > 1.25$ GeV and $|\eta(D^*)| < 1.8$. The complete definition of the visible phase space is given in Table 3.3. Data and Monte Carlo distributions for $p_T(D^*)$ and $\eta(D^*)$ are shown in Figure 3.14.

The number of D^* mesons is determined using statistical methods. For the present analysis two methods are used. The statistical subtraction method is used when comparing distributions in data to the distributions in the Monte Carlo simulation. Only those events are used, for which $|\Delta M - 0.1454| < 0.0025$ GeV. The wrong charge distribution is subtracted from the right charge distribution.

The other method is based on fits to the ΔM distributions and is used for the determination of the cross sections. The method using fits will be described in Chapter 4.

Observable	Range
Q_e^2	2-100 GeV^2
$y_{e\Sigma}$	0.02-0.7
$p_T(D^*)$	> 1.25 GeV
$\|\eta(D^*)\|$	< 1.8

Table 3.3: The visible phase space of the analysis

As mentioned in Section 1.3, the production of D^* mesons takes place through two mechanisms: the direct and the resolved processes. In the RAPGAP Monte Carlo generator, these processes can only be generated separately. Therefore, two distinct Monte Carlo samples, one direct sample and one resolved sample, are used to describe the data. When comparing the distributions in data to the distributions in the Monte Carlo simulation, only the sum of the two Monte Carlo samples is shown. In Figure 3.15 each contribution can be seen, for the transverse momentum and the pseudorapidity of the D^* candidate. Each Monte Carlo contribution is normalized to the data luminosity. The total Monte Carlo prediction is obtained by adding the two normalized Monte Carlo contributions.

3.4.3. Additional Reduction of the Background

To further reduce the large background contribution at low transverse momenta of the D^*, particle identification criteria based on the energy loss with the distance are used. The energy loss is described by the Bethe-Bloch formula [H$^+$02]:

$$-\frac{dE}{dx} = Cz^2\frac{Z}{A}\frac{1}{\beta^2}\left[\frac{1}{2}ln\left(\frac{2m_ec^2\beta^2\gamma^2T_{max}}{I^2}\right) - \beta^2 - \frac{\delta}{2}\right] \tag{3.16}$$

where z is the charge of the incident particle, β is the velocity of the incident particle, $\gamma = (1-\beta^2)^{-1/2}$, Z and A are the atomic charge and atomic mass of the absorber, m_e is the electron mass, I is the mean excitation energy, T_{max} is the maximum energy transfer energy per collision, δ is the density correction and $C = 4\pi N_A r_e^2 m_e c^2$, with N_A the Avogadro number and r_e the classical electron radius.

The experimental dE/dx values measured by the H1 detector differ from the theoretical dE/dx values, due to influences from the detector and track reconstruction. The measured dE/dx values are therefore empirically parametrised using the function:

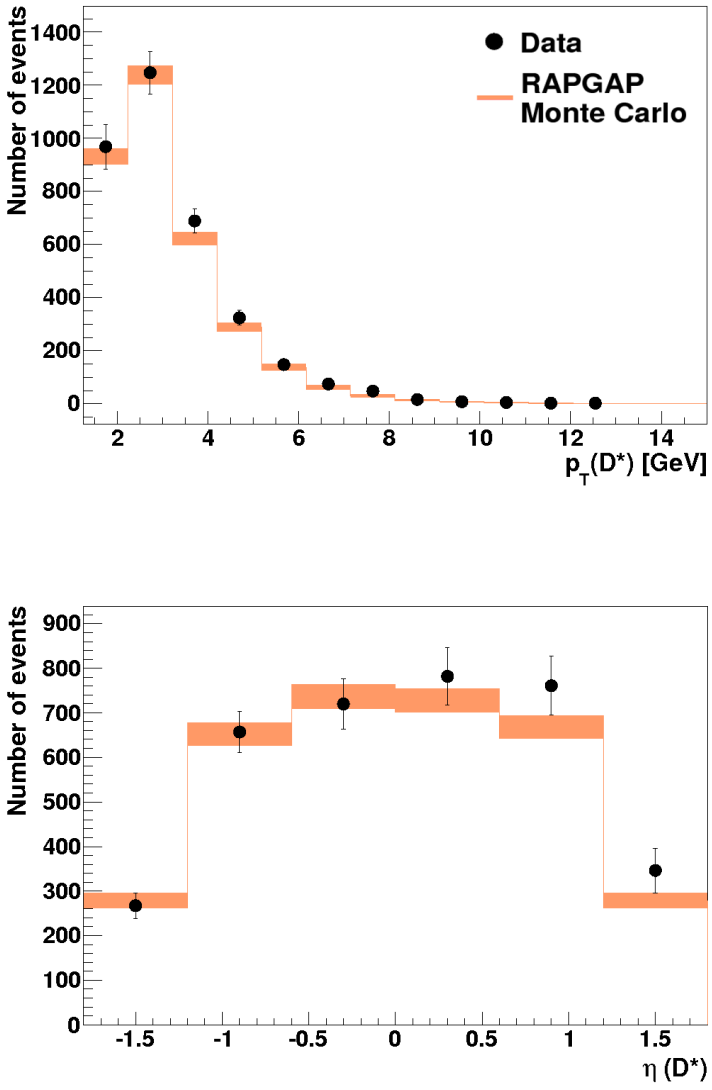

Figure 3.14: Distributions of transverse momentum $p_T(D^*)$ and pseudorapidity $\eta(D^*)$ in data (black points) as compared to the Monte Carlo simulation (orange band).

$$-\frac{dE}{dx} = a_1 z^2 \beta^{-a_2} \left(1 + a_3 e^{-a_4 log(0.25+\beta\gamma)}\right) \tag{3.17}$$

with $a_1 = 1.4139$, $a_2 = 1.6504$, $a_3 = -0.6410$ and $a_4 = 0.56924$. This parametrisation is documented in [Ste99]. The measured dE/dx and the parametrization for kaons, pions, electrons and muons is shown in Figure 3.16.

Experimentally, the measurement of the energy loss proceeds in two steps.

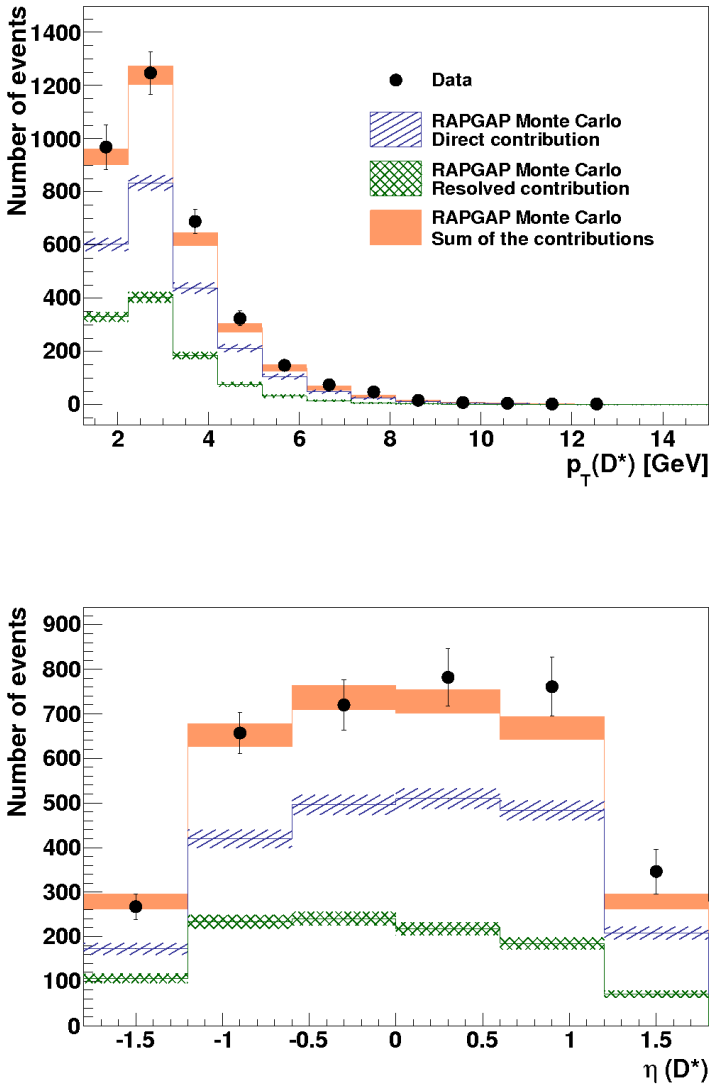

Figure 3.15: Distributions for transverse momentum $p_T(D^*)$ and pseudorapidity $\eta(D^*)$. The data is represented by black points, the direct contribution by the hashed region, the resolved contribution by the doubly hashed region and the sum of the two Monte Carlo contributions by the orange band.

First, the energy loss is measured on one wire in a CJC chamber by adding the charges collected at each end of the wire:

$$dE/dx \sim q_i = q_i^+ + q_i^- \tag{3.18}$$

The single hit charge of the wires are averaged. The value obtained is then

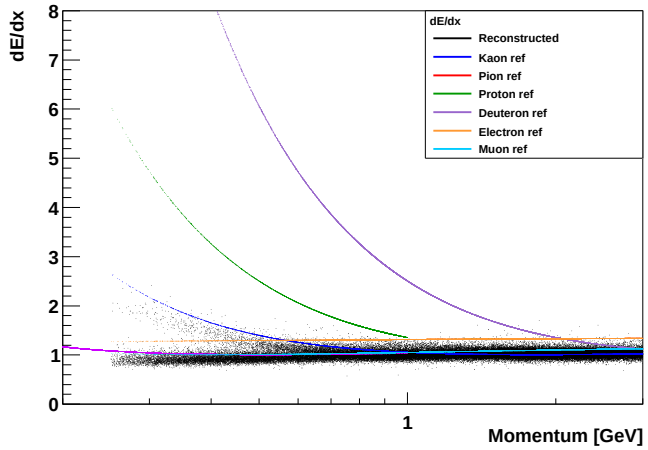

Figure 3.16: The energy loss with respect to the momentum of a particle, for kaons and pions, compared with the empirical parametrization for several particles. The kaon and the pion bands are well separated and reasonably well described by the parametrization.

corrected for the effects from various sources - material, position on the wire, readout electronics, operating conditions (temperature, pressure, high voltage). The second step is to get the dE/dx measurement for a particular track. The measured dE/dx values for each hit are evaluated, and only those satisfying certain quality conditions are kept. The dE/dx average value for a track is then obtained by:

$$\frac{dE}{dx} = \left(\frac{1}{N_{hits_{dE/dx}}} \sum_{i}^{N_{hits_{dE/dx}}} \frac{1}{\sqrt{\left(\frac{dE}{dx}\right)_i}} \right)^{-2} \tag{3.19}$$

where $N_{hits_{dE/dx}}$ is the number of hits with dE/dx information used. Further details regarding the measurement are given in [Ste99].

The momentum information together with the dE/dx knowledge allow identifying certain kinds of particles, like pions, kaons, electrons etc. The variable used for the particle identification is the likelihood of a track to belong to a specific particle:

$$lh = \frac{1}{\sqrt{2\pi}} \int_{\chi^2}^{\infty} \mathrm{d}t \; e^{-\frac{t}{2}} \cdot \frac{1}{\sqrt{t}} \tag{3.20}$$

where the χ^2 is the density for one degree of freedom of $t = dE/dx_{\text{measured}} - dE/dx_{\text{reference}}$. Experimentally, the normalised likelihood is used, in order to account for the probability of misidentification of the particle of interest. The normalised likelihood definition for the the kaon is given in equation 3.21, where $lh_{K,K}$ is the likelihood that the kaon candidate is a 'real' kaon, $lh_{K,\pi}$

and $lh_{K,p}$ are the likelihoods that the kaon candidate is actually a pion or a proton, respectively.

$$N_{lh,K} = \frac{lh_{K,K}}{lh_{K,K} + lh_{K,\pi} + lh_{K,p}} \tag{3.21}$$

The normalized likelihood for the pions is defined in a similar manner to the one for kaons. The normalised likelihood for each daughter is required to be at least 1%. The effect of this cut is most pronounced in the events with low reconstructed p_T of the D^* meson. The ΔM distribution for the p_T of the D^* in the range $1.25 - 2.0$ GeV is shown in Figure 3.17 for events passing the dE/dx requirement compared with the events before applying this condition.

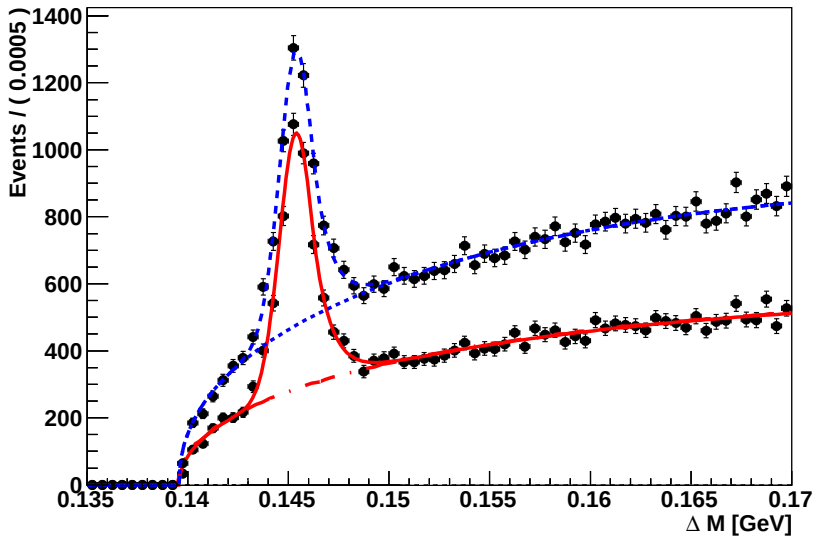

Figure 3.17: Comparison of the ΔM distributions for 1.25 GeV $< p_T(D^*) <$ 2.0 GeV in data. The dashed blue line is the signal fit for the sample without the dE/dx conditions, the dotted blue line is the background fit for the same sample, the continuous red line is the signal fit for the sample with the dE/dx requirements and the dashed-dot red line is the background fit for the second sample. The fitting procedure is detailed in Chapter 4. The reduction in the background of the total sample is of the order of 40% and the reduction in the signal of the total sample is around 5%, most of the effect being visible at low values of p_T of the D^* meson.

Chapter 4: Cross Section Determination and Systematic Uncertainties

In this chapter the determination of the cross section is explained and the cross section results are shown. Also, the sources of systematic uncertainties are presented, together with the additional corrections applied to the cross section calculation.

4.1. Determination of the Cross Section

The visible D^* production cross section is calculated as follows:

$$\sigma^{vis} = \frac{N(D^*)(1-r)}{\mathcal{L}\ \mathcal{B}(D^* \to K\pi\pi_s)\ \varepsilon_{rec}\ \varepsilon_{trig}(1+\delta_r)} \tag{4.1}$$

where

- $N(D^*)$ is the number of D^*,
- r is the contribution from decays other than $D^* \to \pi_s D^0 \to \pi_s K\pi$ (also called 'reflections'),
- $\mathcal{L} = 47.66 \pm 0.71$ pb^{-1} is the integrated luminosity,
- $\mathcal{B} = 2.63 \pm 0.04\%$ [N$^+$10] is the branching ratio for the studied decay mode,
- ε_{rec} is the total reconstruction efficiency,
- ε_{trig} is the trigger efficiency,
- $1 + \delta_r$ are the radiative corrections.

In the following, determination of the cross section is described in details.

4.1.1. Signal Extraction

The number of D^* mesons is determined using the fit to the ΔM distributions. A sum of two functions, one for the signal and one for the background, is used.

The shape of the signal is asymmetric, as it can be seen in Figure 3.13. The parametrisation used for fitting is the Crystal Ball function (CB) [Gai82], which is given by:

$$f(m) = N \cdot \begin{cases} exp\left(-\frac{1}{2}\left(\frac{m-\mu}{\sigma}\right)\right)^2, & \text{if } \frac{m-\mu}{\sigma} \leq -\alpha \\ \frac{\left(\frac{n}{|\alpha|}\right)^n exp\left(-\frac{1}{2}\alpha^2\right)}{\left(\frac{n}{|\alpha|} - |\alpha| - \frac{m-\mu}{\sigma}\right)^n}, & \text{if } \frac{m-\mu}{\sigma} > -\alpha \end{cases} \tag{4.2}$$

In the context of previous analyses [Boe07] of D^* meson production in DIS, extensive studies have been performed, which concluded that the CB function is suitable for describing the ΔM distribution.

The function used for the background description is the Granet parametrisation [G$^+$78]:

$$f(m) = (\delta m)^{p_1} \cdot exp(-p_2 \delta m - (-p_3(\delta m)^2)) \tag{4.3}$$

where $\delta m = m - m_\pi$ is the difference between the reconstructed $m = \Delta M$ and the pion mass m_π, whereas p_1, p_2 and p_3 are parameters left free for the fit procedure.

The fit is performed simultaneously on the right charge and on the wrong charge distributions. The normalization of the background function is not constrained in the right charge fit. For the minimisation procedure, the fit is performed as an unbinned negative log-likelihood fit, where the likelihood is defined as:

$$\mathcal{L}(a) = \prod_{i=1}^{n} f(x_i|a) \tag{4.4}$$

The likelihood gives the probability for a certain measured value x_i with a previously defined choice of the parameter a. The quantity $f(x_i|a)$ is normalised to 1 with respect to parameter a. As fitting tools, the RooFit package [VK05] is used. RooFit is based on the MINUIT package [Jam] and provides additional numerical integration for every step of the optimisation procedure. RooFit allows to compose fit functions in a short and computational efficient way via the definition of probability density functions which are positive defined and normalized to unity.

The events forming the fitted distributions were selected according to the procedures described in Chapter 3. The same cuts were applied to the simulated and reconstructed Monte Carlo events and to the data events. The fit of the total data set analyzed yields 3493 events for the signal and 23352 events for the background and it is shown in Figure 4.1 for both right charge and wrong charge distributions.

The right charge and the wrong charge are fitted simultaneously. The number of background events found by the fit to the right charge sample is lower than the number found by the fit to the right charge sample, by about

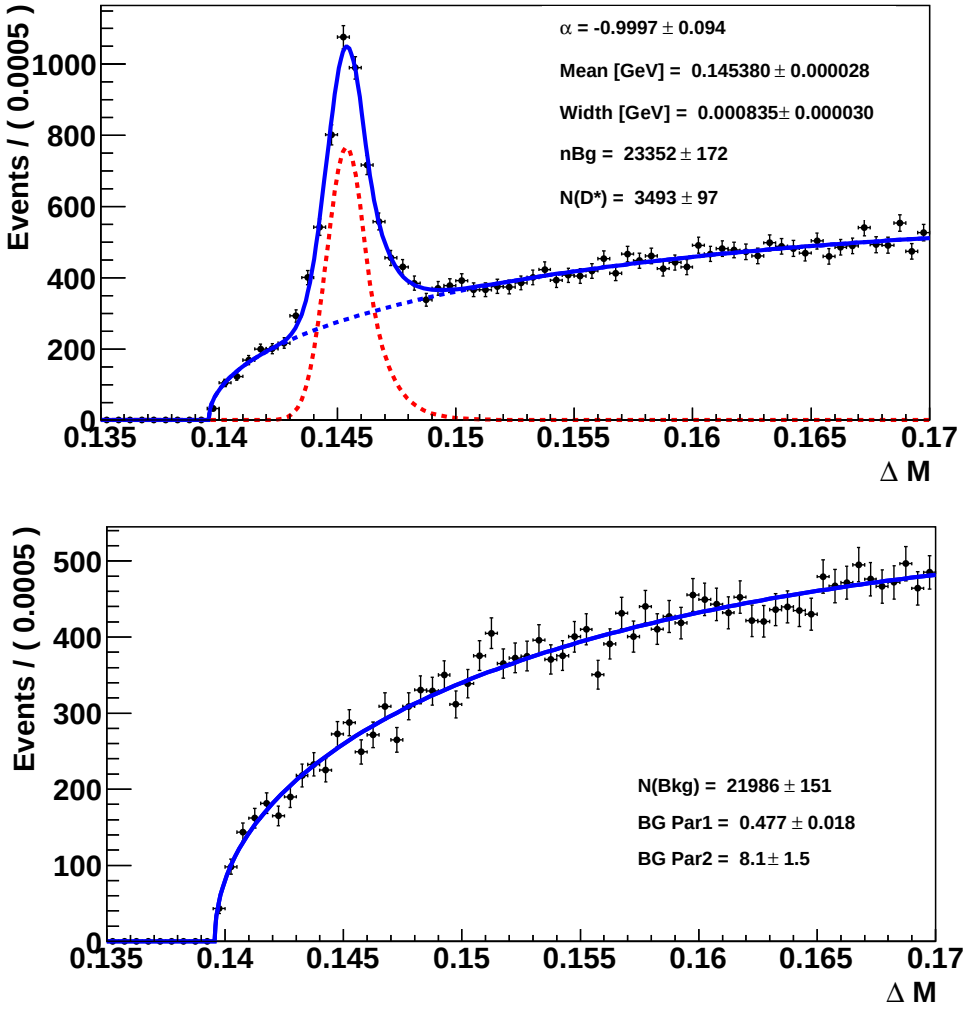

Figure 4.1: The ΔM distribution in data for the right charge sample (above) and for the wrong charge sample (below). On the right charge plot, the data points are with black points, the combined fit is with a solid blue line, the background contribution is drawn as a blue dashed line and the signal contribution is shown with a red dashed line. On the wrong charge plot the background fit is drawn with a solid blue line. The parameters for each fit are in the respective boxes.

6%. This difference is taken into account when making the control distributions, by reweighting the wrong charge distributions accordingly before subtracting them from the right charge distributions. The ΔM distribution is fitted after applying the analysis cuts, as presented in the previous chapter.

4.1.2. Reconstruction Efficiencies

The reconstruction efficiency ε_{rec} is estimated for each kinematic bin by using the Monte Carlo simulation RAPGAP. The efficiency is determined using:

$$\varepsilon_{rec} = \frac{N_{rec}}{N_{gen}}, \tag{4.5}$$

where N_{gen} is the number of generated events in the visible phase space obtained after applying the restrictions for the visible phase space, given in Table 3.3. The generated events without any phase space cuts applied are passed through the same reconstruction algorithm as the data and the number obtained after all the analysis cuts have been applied is N_{rec}. There are two signal Monte Carlo sets used, one for the direct contribution and one for the resolved contribution, as described in Sections 1.3 and 3.4. The reconstruction efficiency is evaluated for each of these Monte Carlo samples using the formula 4.5. The total reconstruction efficiency is obtained by using:

$$\varepsilon_{rec} = \frac{\mathcal{L}_1 \cdot \varepsilon_{rec,1} + \mathcal{L}_2 \cdot \varepsilon_{rec,2}}{\mathcal{L}_1 + \mathcal{L}_2} \tag{4.6}$$

where index 1 is for the direct contribution, index 2 is for the resolved contribution and $\mathcal{L}$ is the luminosity of the respective contribution.

The reconstruction efficiency is affected by events migrating inside and outside the visible phase space and by bib-to-bin migrations within the visible phase space. These effects can be estimated by considering the purities. The purity P_i in bin i is given by:

$$P_i = \frac{N_i^{rec\&gen}}{N_i^{rec}} \tag{4.7}$$

where $N_i^{rec\&gen}$ is the number of events reconstructed and generated in bin i and N_i^{rec} is the number of events reconstructed in bin i regardless where they were generated. The events reconstructed in bin i can be generated in the same bin, in a neighbouring bin, somewhere else in the visible phase space (PS) or outside the visible phase space (oPS). The contributions from each of these sources is shown for the kinematical variables in Figure 4.2. The largest contribution from events not generated in the same bin as the reconstructed events comes from the events generated in a neighbouring bin. The contributions from oPS are quite small and they come mainly from low Q^2 and low $p_T(D^*)$. The migrations from somewhere else in the visible phase space are negligible.

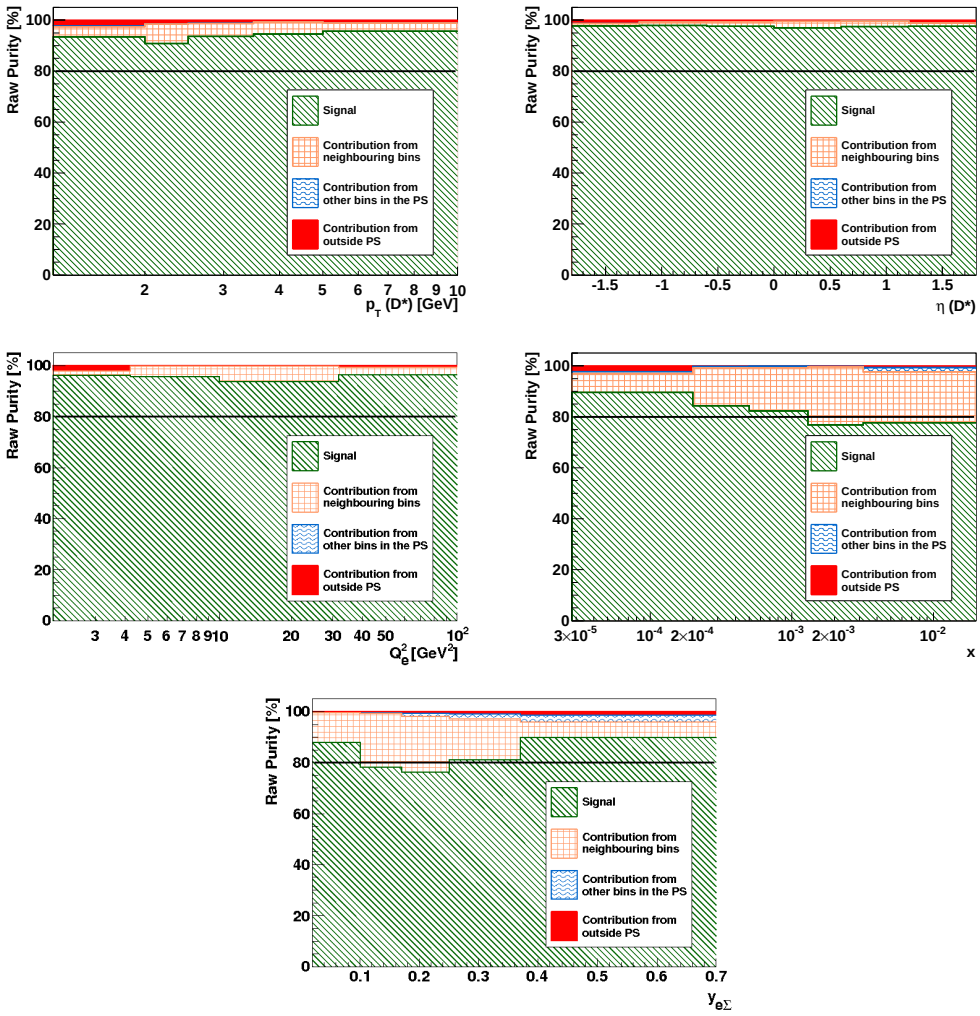

Figure 4.2: Purities for kinematical variables with the individual contributions shown in filled area for the migrations oPS, in squares for neighbouring bins and in wavy lines for the ones from somewhere else in PS. The purity is given in fractions of unity. The black line is at 80%.

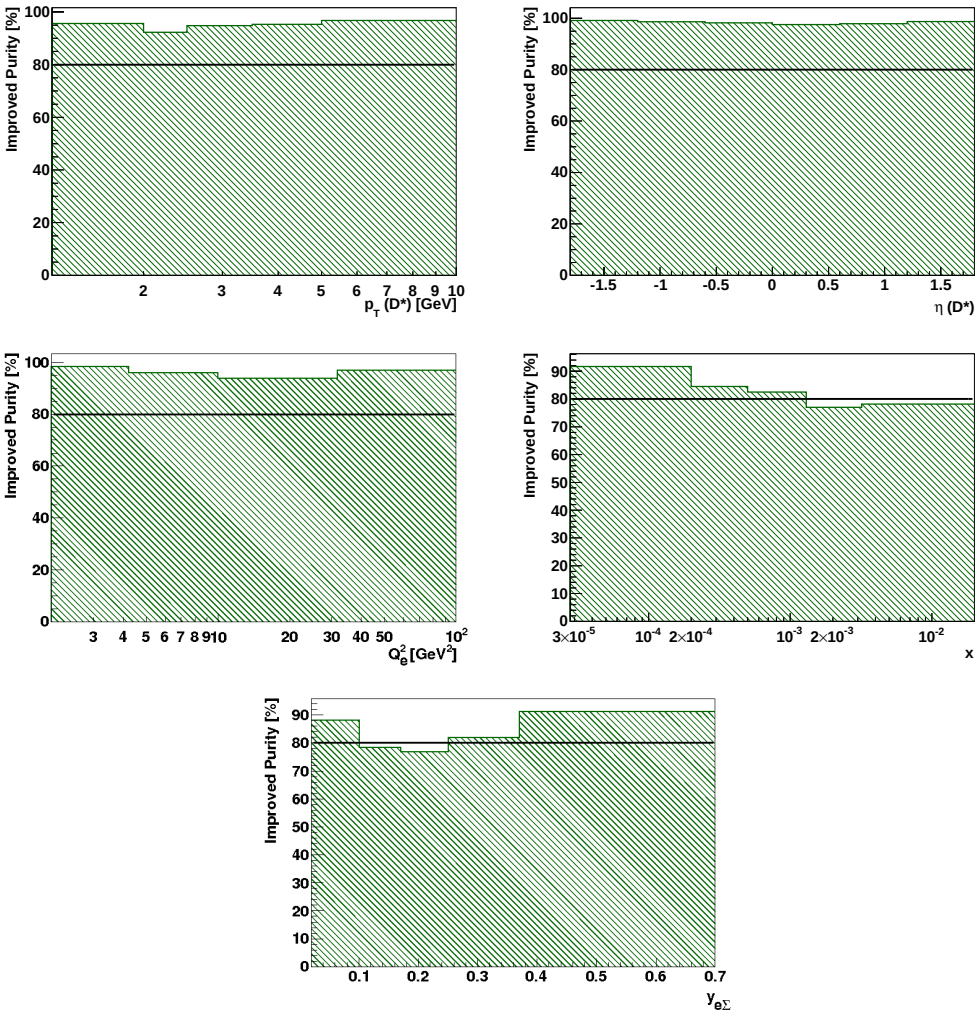

Figure 4.3: Modified purities for $p_T(D^*)$, $\eta(D^*)$, Q^2, x and y. The purity is given in fractions of unity. The black line is at 80%.

Q^2 [GeV^2]	y	Purity
2.0, 4.22	0.02, 0.1	0.80
	0.1, 0.2	0.81
	0.2, 0.4	0.91
	0.4, 0.7	0.97
4.22, 10.0	0.02, 0.1	0.82
	0.1, 0.2	0.82
	0.2, 0.4	0.90
	0.4, 0.7	0.95
10.0, 17.8	0.02, 0.1	0.81
	0.1, 0.25	0.86
	0.25, 0.7	0.95
17.8, 31.6	0.02, 0.15	0.86
	0.15, 0.7	0.95
31.6, 100.0	0.02, 0.15	0.87
	0.15, 0.7	0.96

Table 4.1: Modified purities for $Q^2 - y$ bins. Migrations from outside and within visible phase space are small. Purities are well above 64%.

p_T [GeV]	η	Purity [fractions of unity]
1.25, 2.0	-1.8, -0.6	0.96
	-0.6, 0.6	0.94
	0.6, 1.8	0.95
2.0, 2.5	-1.8, -0.6	0.92
	-0.6, 0.6	0.92
	0.6, 1.8	0.92
2.5, 3.5	-1.8, -0.6	0.95
	-0.6, 0.6	0.95
	0.6, 1.8	0.94
3.5, 5.0	-1.8, -0.6	0.95
	-0.6, 0.6	0.95
	0.6, 1.8	0.95
5.0, 15.0	-1.8, -0.6	0.96
	-0.6, 0.6	0.97
	0.6, 1.8	0.96

Table 4.2: Modified purities for $p_T - \eta(D^*)$ bins. Migrations from outside and within visible phase space are small. Purities are well above 64%.

The migrations outside the visible phase space are accounted for in $\varepsilon_{\mathrm{rec}}^{\mathrm{modified}}$, after subtracting the number of these migrating events from the number of reconstructed events:

$$\varepsilon_{rec}^{\mathrm{modified}} = \frac{N_{rec} - N_{mig}}{N_{gen}} \tag{4.8}$$

As long as the modified purity

$$P_{ij} = \frac{N_{ij}^{rec\&gen}}{N_{ij}^{rec} - N_{mig}} \tag{4.9}$$

is greater than $(0.8)^d$ in all bins, where d is the dimension of the binning, 'improved bin-by-bin' correction 4.8 of the cross section is sufficient and no full unfolding is necessary [Sch]. This is the case for most single differential distributions, shown in 4.3, and for all the double differential ones, given in Table 4.1 and Table 4.2.

The reconstruction efficiencies are recalculated and the yields used in the cross section determination are given in Figure 4.4 for the kinematical observables.

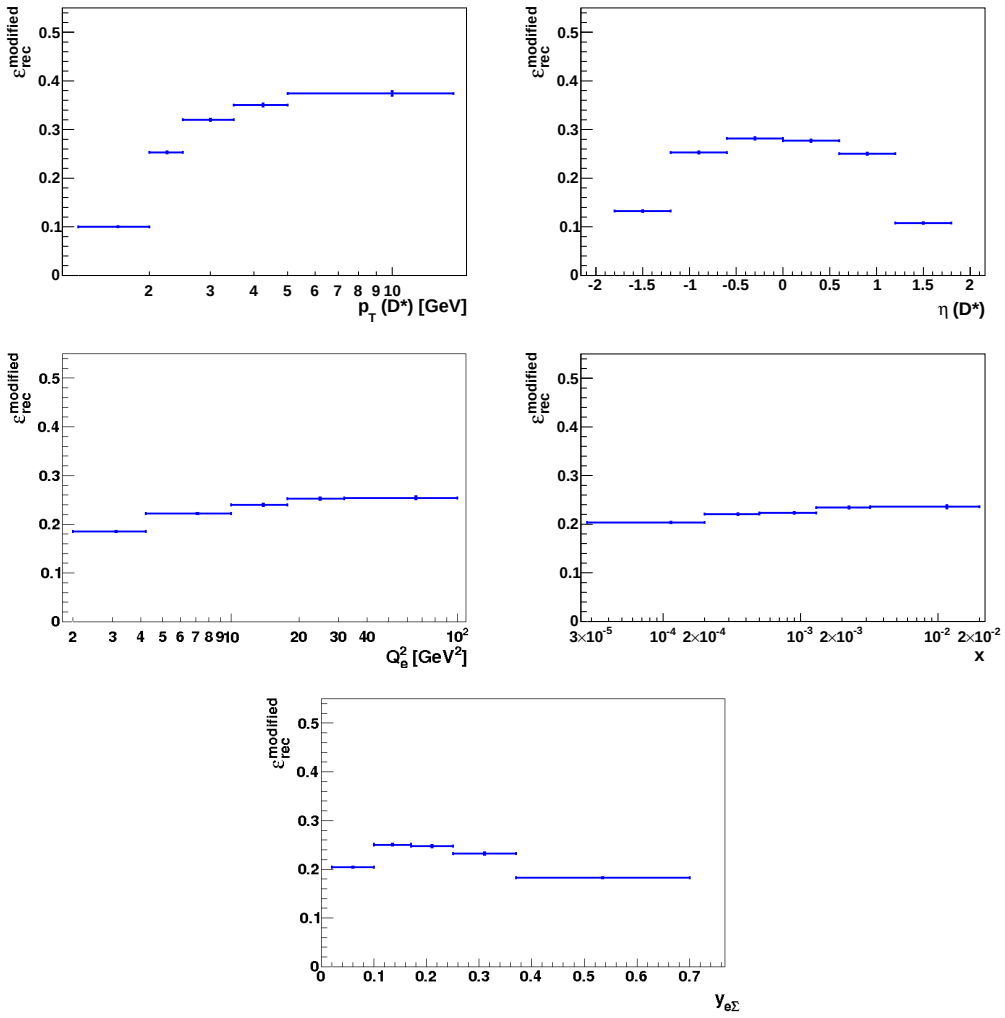

Figure 4.4: Modified reconstruction efficiencies as a function of $p_T(D^*)$, $\eta(D^*)$, Q^2, Bjørken-x and inelasticity y.

4.1.3. Radiative Corrections

In order to correct the measured cross section to the Born level (one-photon exchange), virtual and real NLO QED contributions are taken into account. These contributions are given by event topologies where a photon is radiated prior to the interaction (Initial State Radiation - ISR) or after the interaction (Final State Radiation - FSR).

The radiative correction is expressed in the form:

$$\sigma_{Born+NLO} = (1 + \delta_{rad}) \cdot \sigma_{Born} \tag{4.10}$$

The correction factor $c_{rad} = (1 + \delta_{rad})^{-1}$ is determined by using a radiative Monte Carlo sample, generated by interfacing RapGap with HERACLES [KSM92] which is also used for estimating ε_{rec}. Alternatively, RapGap was used in a non-radiative mode. The correction was estimated for the visible phase space:

$$c_{rad} = \frac{\sigma_{gen}^{non-rad}}{\sigma_{gen}^{rad}} \tag{4.11}$$

by using cross sections at hadron level. The average correction factor in the visible phase space amounts to 4%. This correction is also determined for each bin of the cross sections. The actual values are shown in Figure 4.5 as a function of investigated variables. The correction factor is estimated only for the direct contribution. The Monte Carlo generator doesn't allow the estimation of this correction for the resolved processes, which can be generated only with a non-radiative setup.

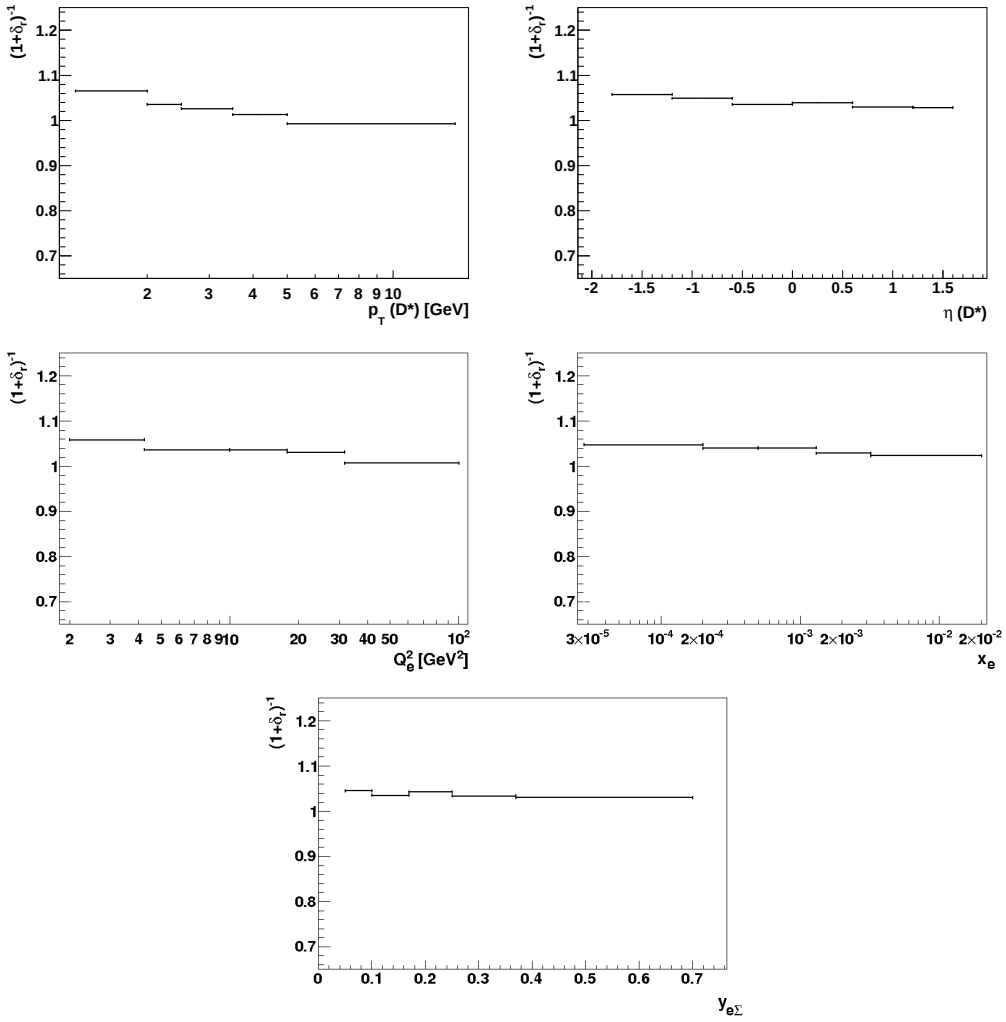

Figure 4.5: Radiative corrections as a function of $p_T(D^*)$, $\eta(D^*)$, Q^2, Bjørken-x and inelasticity y.

4.1.4. Contribution from Reflections

The D^0 meson has several decay modes with kaons and pions in the final state, summarised in Table 4.3, which can contribute to the signal in the ΔM distribution.

Decay	Branching Ratio
$D^0 \to K^- K^+$	$(0.39 \pm 0.007)\%$
$D^0 \to \pi^- \pi^+$	$(0.14 \pm 0.0026)\%$
$D^0 \to \pi^- \pi^+ \pi^0$	$(1.44 \pm 0.06)\%$
$D^0 \to \pi^- \pi^+ \pi^- \pi^+$	$(0.74 \pm 0.021)\%$
$D^0 \to K^- e^+ \nu_e$	$(3.55 \pm 0.05)\%$
$D^0 \to K^- \mu^+ \nu_\mu$	$(3.31 \pm 0.13)\%$
$D^0 \to \pi^- e^+ \nu_e$	$(0.29 \pm 0.008)\%$
$D^0 \to \pi^- \mu^+ \nu_\mu$	$(0.24 \pm 0.024)\%$

Table 4.3: Other decay modes with kaons and pions, other than the channel used in this analysis. Branching ratios quoted according to [N$^+$10].

In a previous study [A$^+$11], these contributions were estimated to be around 3.8% for a narrower Q^2 range. As these contributions are not expected to depend on Q^2, this value is used in the current work as well, together with its systematic uncertainty.

4.1.5. Trigger Efficiencies

The trigger efficiency is evaluated by using a set of monitor triggers, s00 and s09. Monitor triggers don't contain a z_{vertex} part, a SpaCal part or a DCRPh_THig part. The mentioned parts are the ones defining the trigger used in this analysis. A set of triggers is necessary, while those completely independent have very small rates or are heavily prescaled. The efficiency is defined:

$$\varepsilon = \frac{N_{triggered}}{N_{all}} \tag{4.12}$$

where N_{all} is the number of events selected by the monitor triggers and $N_{triggered}$ is the number of events which are selected by both the analysis trigger and the monitor triggers. The efficiency is plotted in bins of Q_e^2, x_e, $y_{e\Sigma}$, $p_T(D^{*\pm})$ and $\eta(D^{*\pm})$ and is flat within a few percents. The overall trigger efficiency is 91%. The trigger efficiencies in data are used in the cross section determination. In the first and last bins of the $\eta(D^{*\pm})$, the trigger

efficiency used in the cross section determination is the average between the efficiencies determined in data and in the Monte Carlo simulation.

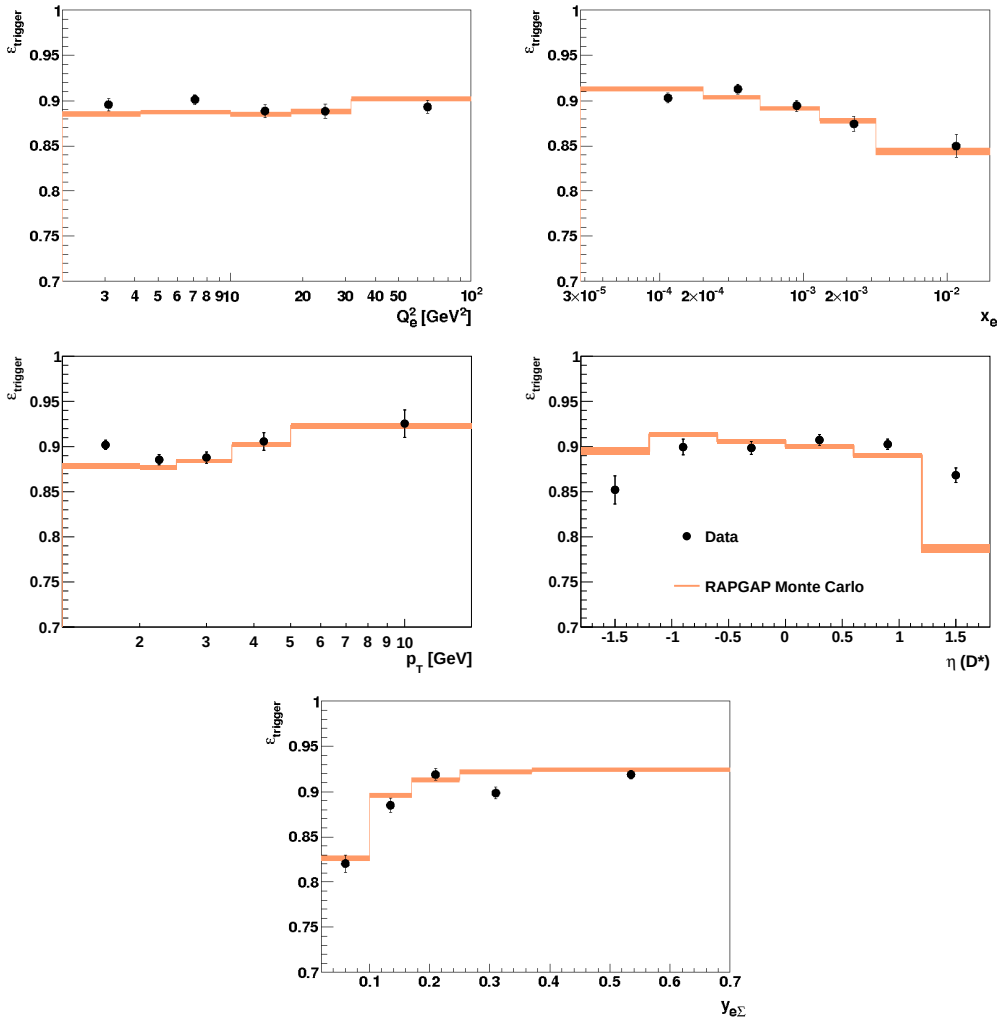

Figure 4.6: Trigger efficiency as a function of $p_T(D^*)$, $\eta(D^*)$, Q^2, Bjørken-x and inelasticity y.

4.2. Experimental Systematic Uncertainties

In this section, the experimental systematic uncertainties will be discussed. The sources considered and their contributions to the total cross section are summarised in Table 4.4.

Source	Contribution
Uncorrelated	
Trigger	1%
Signal extraction	3%
Reflections	1%
Correlated	
D^0 mass cut	2%
Tracking	3.4 %
Luminosity	1.5%
Branching ratio	1.5%
Fragmentation	1%
Electron energy scale	0.2%
Electron θ angle	1.3%
Hadronic energy scale	0.4%
Sum	**5.83%**

Table 4.4: Summary of the considered sources of systematic uncertainty. All contributions are added in quadrature.

The uncertainties are grouped into a bin-to-bin correlated and an uncorrelated part and each of these uncertainty sources will be discussed in the following subsections. The dominant uncertainties are the tracking uncertainty and the signal extraction uncertainty. For the latter, the larger value is correlated to the low statistics in data.

4.2.1. Uncorrelated Uncertainties

Trigger Uncertainty. It is not possible to relax or restrict the trigger conditions in order to evaluate the possible systematic uncertainties. Therefore, the statistical uncertainty on the trigger efficiency determination is taken as systematic uncertainty. Because the events in the monitor sample and the events in the triggered sample used for estimating the trigger efficiency are correlated, the statistical uncertainty is calculated by:

$$\sigma(\varepsilon_{trig}) = \frac{\sqrt{N_{triggered} \cdot (1 - \varepsilon_{trig})}}{N_{monitored}} \tag{4.13}$$

It amounts to about 1% for the total sample and it is estimated also differentially.

Signal Extraction. The method for the estimation of a signal extraction uncertainty has previously been used in [Jun09]. The main idea is to check the stability of the fit to the ΔM distribution against using different parametrisations. For signal, the Crystal Ball function is replaced with the Bukin function:

$$f_{Bukin}(x) = A \cdot exp\left(-\frac{1}{2}\frac{ln^2(1 + \Lambda\tau(x - x_0))}{\tau^2} + \tau^2\right) \tag{4.14}$$

and for background the Granet parametrisation is replaced with a polynomial shape:

$$(x - m_0)^2 \cdot (1 - b \cdot x^2) \tag{4.15}$$

The differences are evaluated for full data and Monte Carlo samples, in order to minimise the dependence of the fit on the statistical effects. The maximum difference is found to be around 3% in data and less than 1% in Monte Carlo. A summary of the numbers of D^* given by each combination is in Table 4.5.

Function	Data	MC direct	MC resolved
CB+Garnet	3493	167138	130485
CB+Poly	3506	167404	130435
Bukin+Garnet	3540	168884	131612

Table 4.5: The number of D^* mesons, obtained by using different fit parametrisations.

4.2.2. Correlated Uncertainties

Uncertainty of the D^0 mass cut. The efficiency of restricting the reconstructed mass of the D^0 candidate within 80 MeV around the PDG value was studied on a larger data and Monte Carlo sample [Jun09]. The uncertainty of this cut was estimated to be 2%.

Tracking Reconstruction Uncertainty. The uncertainty on the reconstruction of the kaon and pion tracks in the CJC has several sources:

- Fitting the tracks to the primary vertex presents some differences between data and Monte Carlo. This was evaluated for the D^* analysis [Sch04] and found to be 1% per D^* candidate.

- The algorithm of finding charged tracks with low transverse momenta has an uncertainty of 1% per track. There were dedicated studies [Beh05], performed using charged pions coming from the K_s^0 decay, as described in [Erd96].

- The nuclear interactions of the particles with the detector material are not included in the detector simulation. Therefore, investigations were made [Bri10, Dau10] to quantify the effects of these interactions and subsequently correct the detector simulation. The remaining uncertainties are 1% for the slow pion and 0.5% for the kaon and the pion.

All these sources are added in quadrature, resulting in a 3.4% total tracking reconstruction uncertainty.

Fragmentation Uncertainty. The RapGap Monte Carlo samples used for the data correction were generated with a Bowler fragmentation function with the parameters $a = 0.437$ and $b = 0.850$. The fragmentation variable is defined in the center-of-mass system of e^+e^- interaction as:

$$z_{frag} = \frac{(E + p_L)_{D*}}{(E + p)_{\text{parent quark}}} \tag{4.16}$$

where p_L is the component of the hadron momentum which is parallel to the momentum of the parent c quark. It represents the momentum fraction of the parton's momentum which is transferred to the resulting hadron. The H1 measurement [A$^+$09] of the fragmentation variable has shown that the hardness of the fragmentation function is different in different regions of the partonic center-of-mass system $\hat{s}$. The parameters were determined for two regions, defined by the photon-gluon centre of mass energy $\hat{s}$: $\hat{s} < 70$ GeV and $\hat{s} > 70$ GeV. The z_{frag} distribution was reweighted to the Kartvelishvili function with the respective parameters taken from [A$^+$09] and shown in Table 4.6. The reweighted z_{frag} distribution is shown in Figure 4.7.

In order to estimate the fragmentation uncertainty, two variations were made. First, the $\hat{s}$ threshold $\hat{s} = 70$ GeV between the two regions was shifted up and down by 20 GeV simultaneously for both regions in the same direction. Second, the Kartvelishvili parameter α was shifted up and down by the errors given in the publication, again, simultaneously for both regions in the same direction. The effect on the number of events at hadron level was estimated in each cross section bin, with respect to the number of events obtained when reweighting to the Kartvelishvili function with the $\hat{s}$ threshold

Region	Parameter Value	Uncertainty
$\hat{s} < 70$ GeV	4.4	$^{+0.6}_{-0.5}$
$\hat{s} > 70$ GeV	10.3	$^{+1.9}_{-1.6}$

Table 4.6: Values of the Kartvelishvili parameter for the two $\hat{s}$ regions.

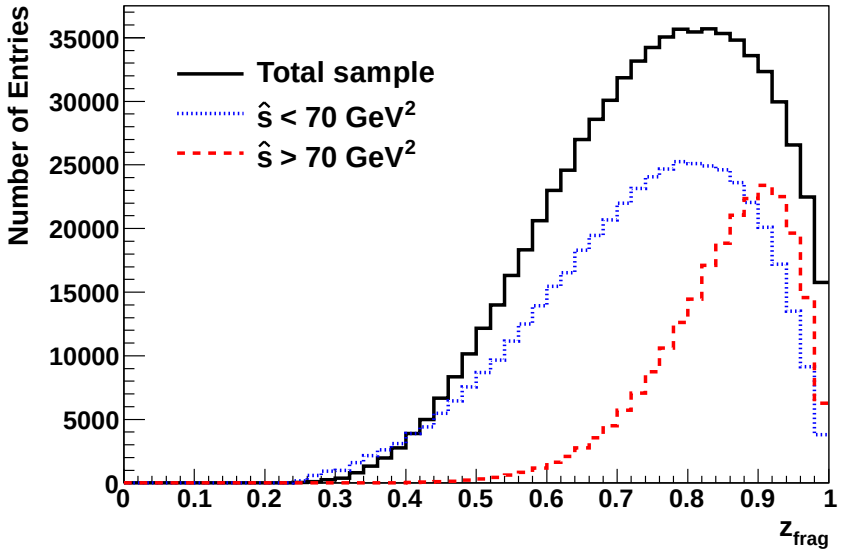

Figure 4.7: The distribution of the fragmentation variable z_{frag} reweighted to the Kartvelishvili function with parameter $\alpha = 4.4$ for the events with $\hat{s} < 70$ GeV (dotted line) and $\alpha = 10.3$ for the events with $\hat{s} > 70$ GeV (dashed line). The total number of reweighted events is given by the full line.

at 70 GeV and the nominal values of the parameters. The effect of the varying of the threshold is shown in Figure 4.8 as a function of the kinematical variables. The reweighting procedure described in this section was performed solely for the purpose of evaluating the fragmentation uncertainty and the reweighting factors are not used for data corrections or in the cross section comparisons.

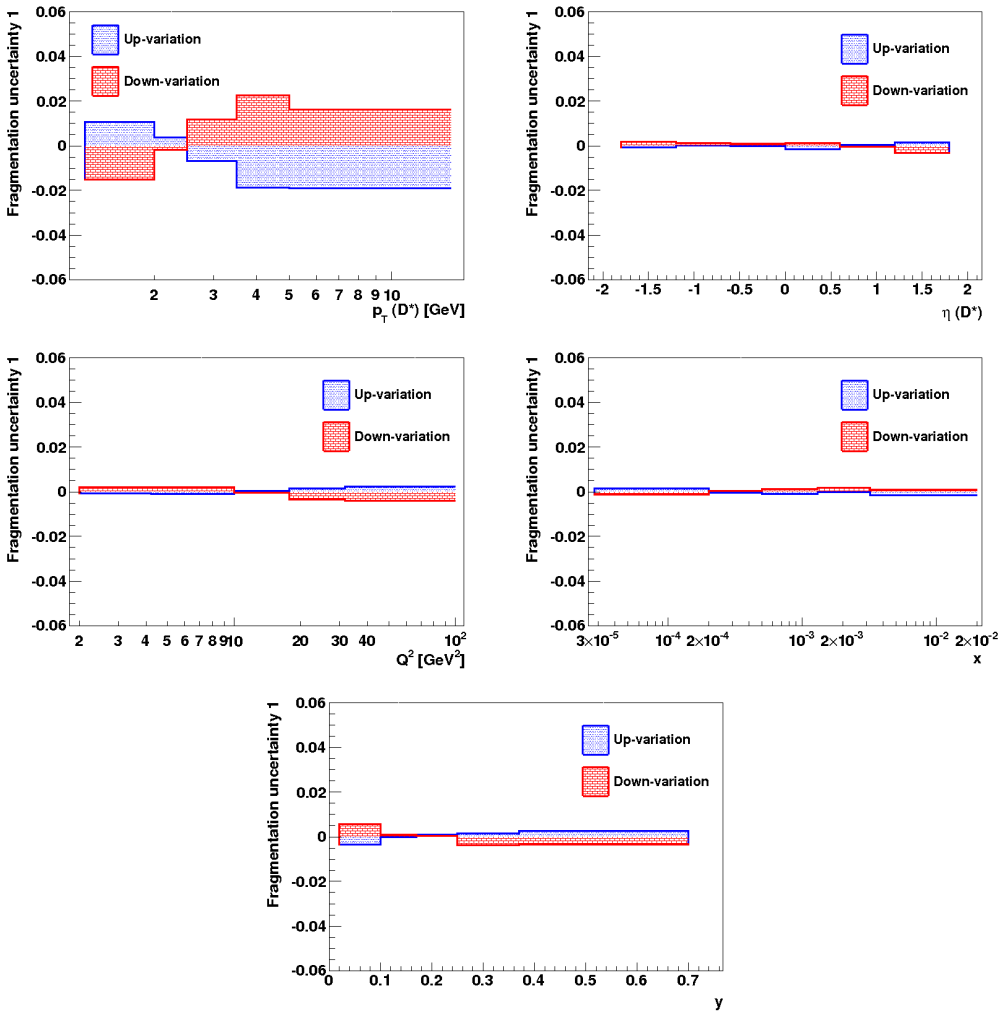

Figure 4.8: The obtained uncertainties when varying the value of $\hat{s}$ threshold up (blue) and down (red) with 20 GeV. The effect on the cross section is below 1%, in most cases even less than 0.5%.

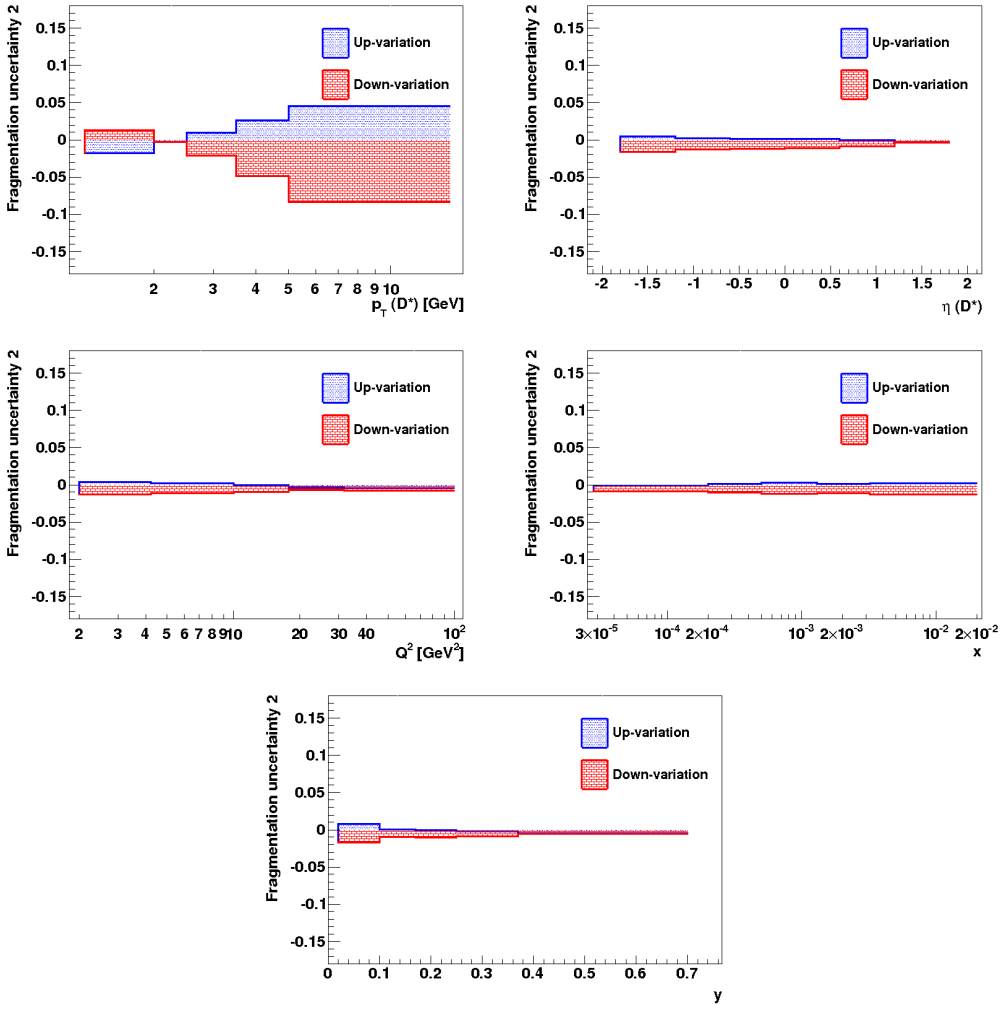

Figure 4.9: The obtained uncertainties when varying the value of the fragmentation function parameter up (blue) and down (red) with the respective errors. The effect on the cross section is in most cases below or around 0.5%.

The variation of the fragmentation function parameters up and down within the respective errors was also performed. A graphical representation of the effect is shown in Figure 4.9. While most kinematical variables shown are rather insensitive to the fragmentation, provided that the variation is small, the effect on the p_T distribution is more visible. This is explained by the dependence of the meson's momentum on the charm quark's momentum.

Electromagnetic Energy Scale Uncertainty. The systematic uncertainty on the measurement of the energy scale of the scattered electron is estimated by comparing the electron and the double angle methods for the reconstructed scattered electron four-vector. The uncertainty varies linearly from 1% at 2 GeV to 0.2% at 27.5 GeV. The energy of the scattered electron is shifted up and down by this function and the changes are propagated to the 4-vector of the electron and the kinematical variables. The uncertainty of the electromagnetic energy scale variation on the cross section is estimated by:

$$\delta = \frac{\sigma_{nominal} - \sigma_{shifted}}{\sigma_{nominal}} \tag{4.17}$$

where $\sigma_{nominal}$ is the cross section determined with the nominal Monte Carlo samples and $\sigma_{shifted}$ is the cross section determined with the shifted Monte Carlo samples. The effect of this shift is exemplified graphically in Figure 4.10. An uncertainty of 0.5% covers the variations in most distributions. The x distribution is more sensitive to this variation, because x is reconstructed using the electron energy. This uncertainty is completely covered by the statistical uncertainty in the respective bins. The uncertainty on the total sample is 0.2%.

Electron Polar Angle Measurement Uncertainty. The systematic uncertainty on the measurement of the polar angle of the scattered electron is estimated to be 2 mrad by comparing the electron and the double angle methods for the reconstructed scattered electron four-vector. The value of this angle is shifted up and down by 2 mrad and the changes are propagated to the 4-vector of the electron and the kinematical variables. The effect is around 1.3% on the total sample. The x and Q^2 are more influenced by this variation, as they are reconstructed using the polar angle of the scattered electron.

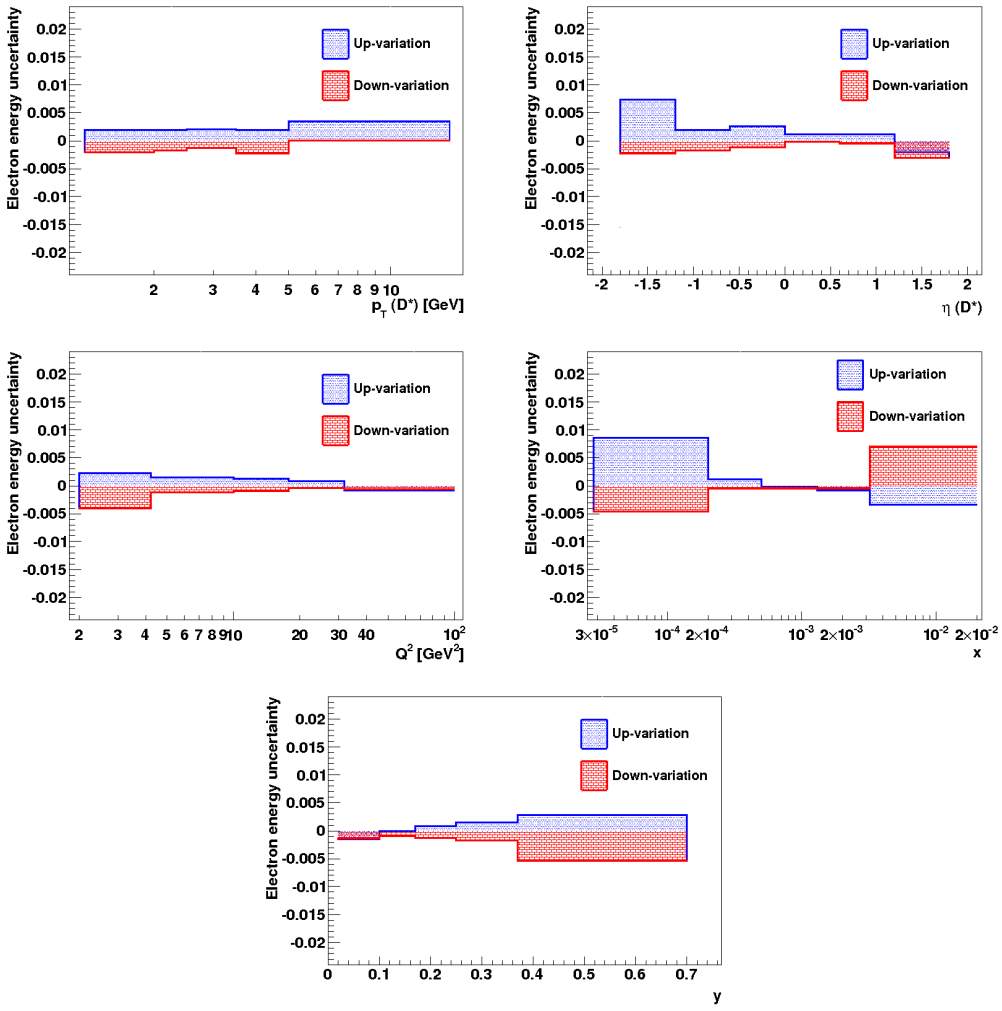

Figure 4.10: The electromagnetic scale uncertainty. The up variation (blue dots) and the down variation (red bricks) are well covered by the statistical uncertainty in the respective bins. The relative uncertainty for each variable is given in fractions of unity.

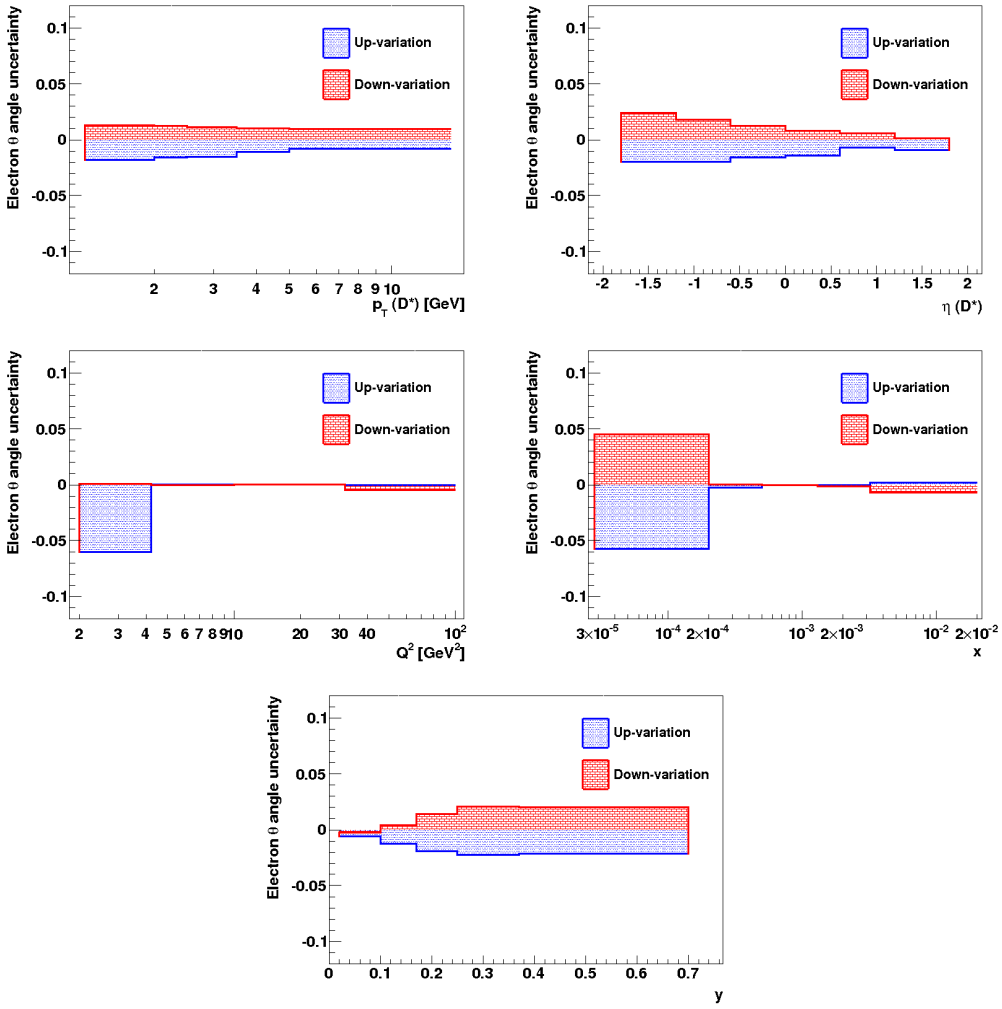

Figure 4.11: The electron polar angle uncertainty. The effect on the cross section by measuring a larger polar angle is shown in blue dots, and the effect of measuring a lower polar angle is shown in red bricks. The relative uncertainty for each variable is given in fractions of unity.

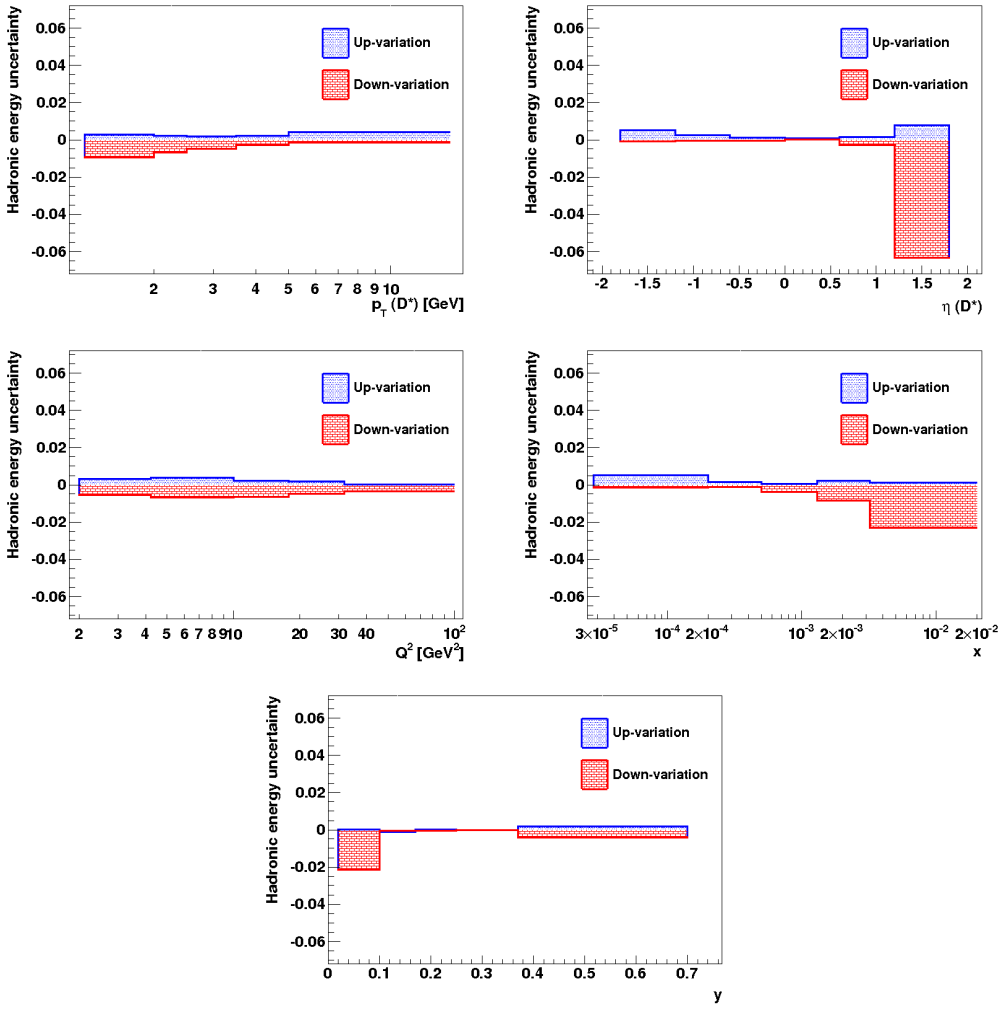

Figure 4.12: The hadronic energy scale uncertainty. A larger effect is seen at large $\eta(D^*)$, but it still covered by the statistical uncertainty in that bin. The relative uncertainty for each variable is given in fractions of unity.

Hadronic Energy Scale Uncertainty. The procedure for calibrating the hadronic energy scale is described in detail in [Kog10]. The calibration was redone for this data period and the uncertainty of the hadronic energy scale is 1% [Kog12]. The $E - p_z$ and $y_{e\Sigma}$ are recalculated accordingly and the effect on the cross sections is investigated. As expected, there is a visible effect at small y and in very forward direction (large $\eta(D^*)$), but this effect is completely covered by the statistical uncertainty in those bins. The overall effect for the up variation is about 0.5 %, while for the down variation, the effect is 0.9 %. The variation is plotted as a function of the kinematical variables and shown in 4.12.

4.3. Cross Sections

4.3.1. Total Cross Section

The total measured cross section is determined using the formula 4.1 in the visible phase space defined by $2 < Q^2 < 100$ GeV^2, $0.02 < y < 0.7$, $p_T(D^*) > 1.25$ GeV^2 and $|\eta(D^*)| < 1.8$. The total measured cross section is:

$$\sigma_{vis}^{tot} = 13.68 \pm 0.38(\text{stat}) \pm 0.79(\text{syst}) \text{ nb} \tag{4.18}$$

The total cross sections predicted by the RapGap Monte Carlo program and the HVQDIS calculation are given in Table 4.3.1. The prediction for the total cross section is lower than the measured cross section.

Prediction	Cross Section (nb)
RapGap Direct	7.47
RapGap Resolved	4.31
Total	**11.78**
HVQDIS	9.07

Table 4.7: Total cross section predictions in the visible phase space.

4.3.2. Single Differential Cross Sections

Single differential cross sections are measured as a function of kinematical variables Q^2, x, y and as a function of D^* kinematics p_T and η. The measured cross sections are compared to a leading order Monte Carlo prediction and the results are shown in Figures 4.13, 4.15, 4.17, 4.19 and 4.21. The experimental values obtained for the cross section as a function of Q^2, x, y and as a function of D^* kinematics p_T and η is given in Tables 4.8, 4.9, 4.10, 4.11 and 4.12 together with the breakdown of the total uncertainty in statistical and systematical uncertainties.

The differential cross section as a function of Q^2 shows a good agreement between the measurement and the prediction within the uncertainties of the measurement. The shape and the normalization are well described.

The predicted differential cross section as a function of x shows a small deficit at very low x, which doesn't look significant when considering the cross section at high y. Overall, the description of the measured cross sections is reasonable, with no significant deviations.

The shape of the cross section as a function of D^* kinematics, p_T and η, are in agreement with the Monte Carlo prediction. There is some undershooting of the data in the forward direction and at high p_T, effect also seen in an analysis [A$^+$11] with higher statistics performed on the HERA 2 data (between 2004 and 2007).

The measured cross sections are compared to the next-to-leading order calculation HVQDIS and the results are shown in Figures 4.14, 4.16, 4.18, 4.20 and 4.22. The HVQDIS calculation is described in Chapter 1, Section 1.5. The calculation gives a reasonable description of the shape of the cross section in most cases, but the normalization is lower. The underestimation of the cross section at large $\eta(D^*)$ is present also in the HVQDIS calculation.

Q^2 range [GeV^2]	$\frac{d\sigma}{dQ^2}$ ($\frac{nb}{GeV^2}$)	δ_{stat} (%)	δ^+_{syst} (%)	δ^-_{syst} (%)
2.0, 4.22	1.859	4.93	7.97	5.31
4.22, 10.0	0.681	5.04	5.18	5.26
10.0, 17.8	0.261	6.22	5.18	5.22
17.8, 31.7	0.0896	7.35	5.17	5.21
31.7, 100.0	0.022	9.49	5.17	5.22

Table 4.8: Single differential cross section as a function of Q^2. The cross section is given in nb/GeV^2 and the uncertainties are given in percents.

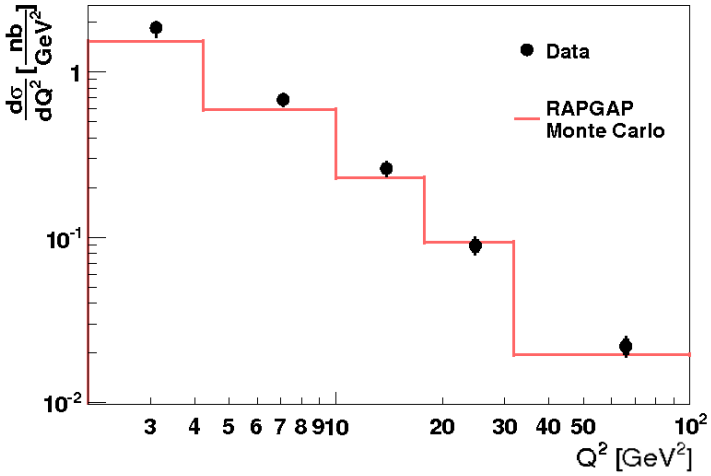

Figure 4.13: Single differential cross section as a function Q^2. The black points represent the experimental cross section and the red line is the theoretical cross section. The vertical error bars represent the total uncertainty on the measurement and the inner bars represent the statistical uncertainty.

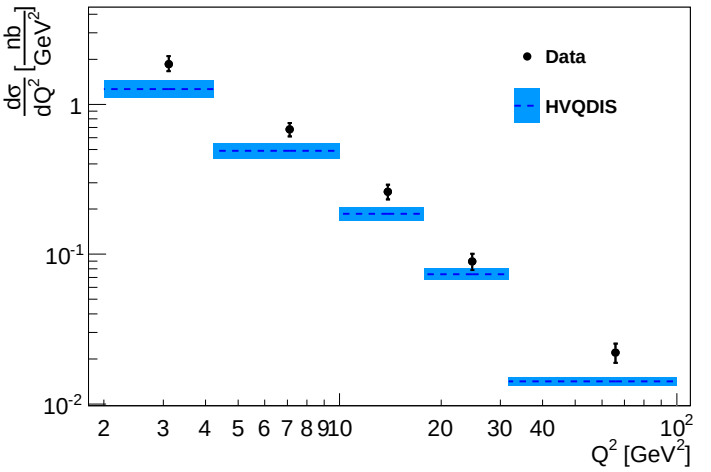

Figure 4.14: Single differential cross section as a function Q^2. The black points represent the experimental cross section and the blue dashed line is the theoretical cross section. The vertical error bars represent the total uncertainty on the measurement and the shaded area represents the theoretical uncertainty.

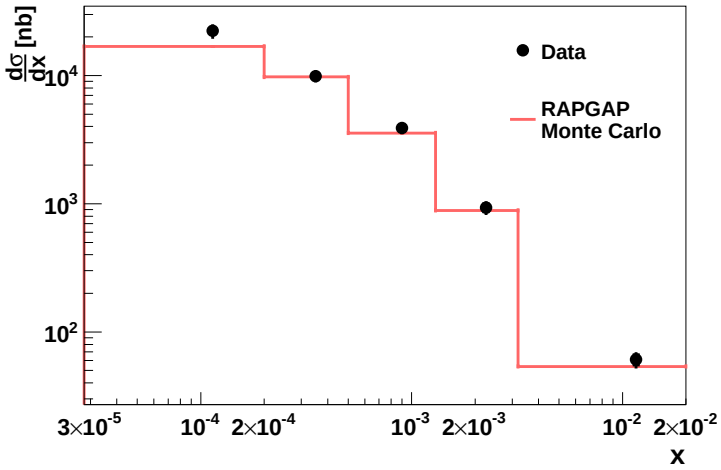

Figure 4.15: Single differential cross section as a function of x. The black dots represent the experimental cross section and the red line is the theoretical cross section. The vertical error bars represent the total uncertainty on the measurement and the inner bars represent the statistical uncertainty.

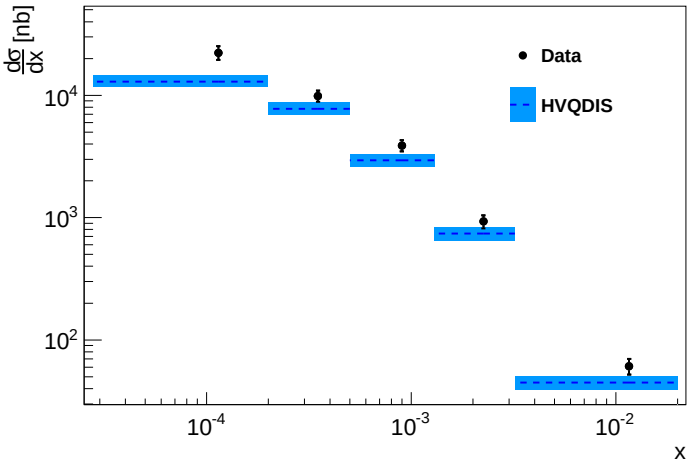

Figure 4.16: Single differential cross section as a function of x. The black dots represent the experimental cross section and the blue dashed line is the theoretical cross section. The vertical error bars represent the total uncertainty on the measurement and the shaded area represents the total theoretical uncertainty.

x range	$\frac{d\sigma}{dx}$ (nb)	δ_{stat} (%)	δ^{+}_{syst} (%)	δ^{-}_{syst} (%)
$2.8{\cdot}10^{-5}$, $2{\cdot}10^{-4}$	22270.7	5.48	7.71	6.95
$2{\cdot}10^{-4}$, $5{\cdot}10^{-4}$	9879.25	5.36	5.13	5.23
$5{\cdot}10^{-4}$, $1.3{\cdot}10^{-3}$	3886.31	5.16	5.15	5.27
$1.3{\cdot}10^{-3}$, $3.2{\cdot}10^{-3}$	931.71	7.12	5.22	5.27
$3.2{\cdot}10^{-3}$, 0.02	60.87	9.15	5.77	5.39

Table 4.9: Single differential cross section as a function of x. The cross section is given in nb and the uncertainties are given in percents.

y range	$\frac{d\sigma}{dy}$ (nb)	δ_{stat} (%)	δ^{+}_{syst} (%)	δ^{-}_{syst} (%)
0.02, 0.1	46.40	4.68	5.74	5.44
0.1, 0.17	31.31	6.29	5.28	5.19
0.17, 0.25	26.93	5.91	5.45	5.40
0.25, 0.37	16.57	9.30	5.61	5.63
0.37, 0.7	8.63	7.86	5.59	5.57

Table 4.10: Single differential cross section as a function of y. The cross section is given in nb and the uncertainties are given in percents.

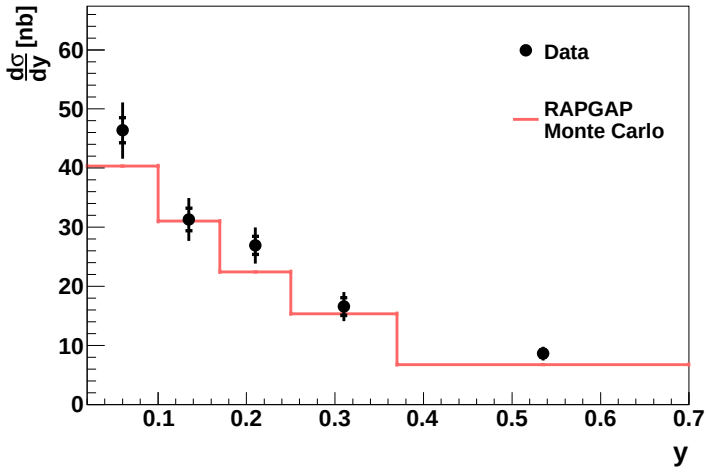

Figure 4.17: Single differential cross section as a function of y. The black dots represent the experimental cross section, the red line is the theoretical cross section. The vertical error bars represent the total uncertainty on the measurement and the inner bars represent the statistical uncertainty.

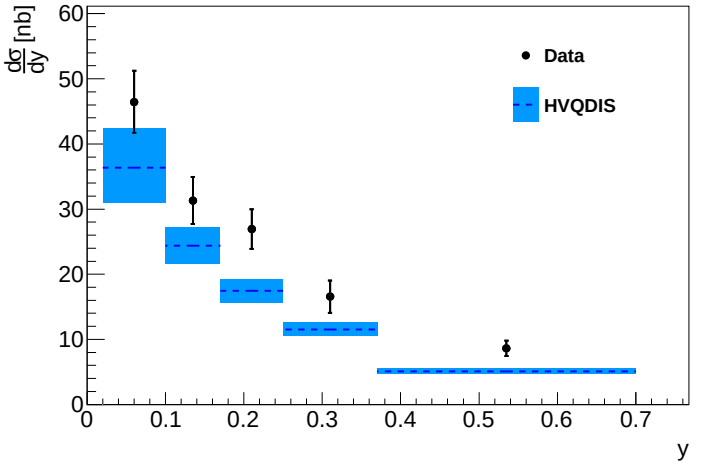

Figure 4.18: Single differential cross section as a function of y. The black dots represent the experimental cross section, the blue dashed line is the theoretical cross section. The vertical error bars represent the total uncertainty on the measurement and the shaded area represents the total theoretical uncertainty.

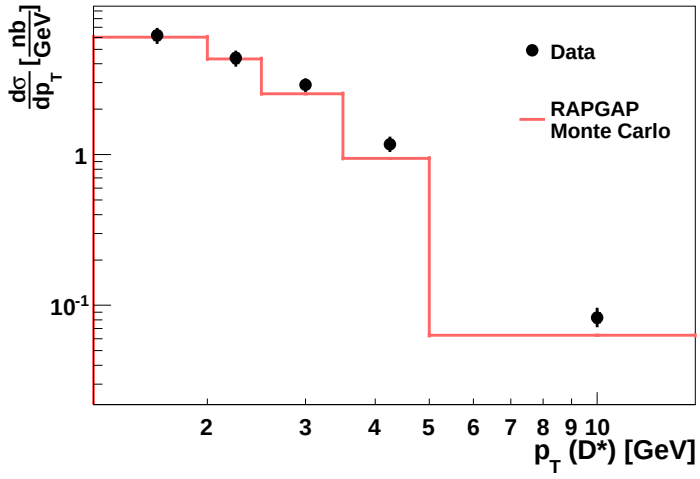

Figure 4.19: Single differential cross section as a function of $p_T(D*)$. The black dots represent the experimental cross section and the red line is the theoretical cross section. The vertical error bars represent the total uncertainty on the measurement and the inner bars represent the statistical uncertainty.

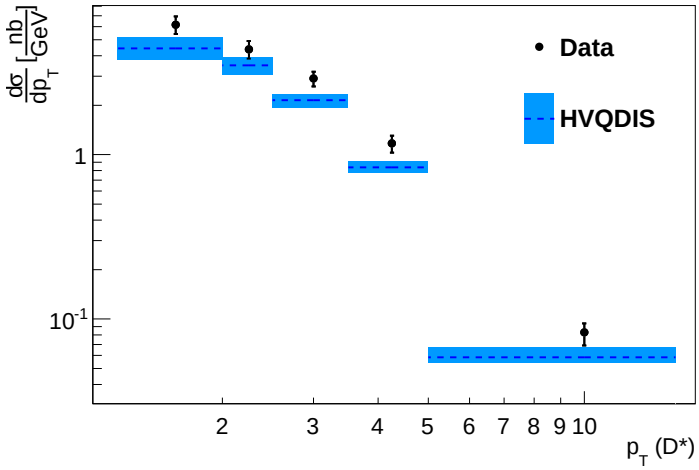

Figure 4.20: Single differential cross section as a function of $p_T(D*)$. The black dots represent the experimental cross section and the blue dashed line is the theoretical cross section. The vertical error bars represent the total uncertainty on the measurement and the shaded area represents the total theoretical uncertainty.

p_T range	$\frac{d\sigma}{dp_T}$ $(\frac{nb}{GeV})$	δ_{stat} (%)	δ^+_{syst} (%)	δ^-_{syst} (%)
1.25, 2.0	6.18	6.51	5.78	5.80
2.0, 2.5	4.37	6.78	5.44	5.29
2.5, 3.5	2.90	4.60	5.58	5.69
3.5, 5.0	1.17	4.81	6.32	7.39
5.0, 15.0	0.082	6.48	7.18	10.16

Table 4.11: Single differential cross section as a function of $p_T(D^*)$. The cross section is given in nb/GeV and the uncertainties are given in percents.

η range	$\frac{d\sigma}{d\eta}$ (nb)	δ_{stat} (%)	δ^+_{syst} (%)	δ^-_{syst} (%)
-1.8, -1.2	2.89	8.40	5.67	6.01
-1.2, -0.6	3.20	5.70	5.50	5.59
-0.6, 0.0	3.49	5.33	5.37	5.41
0.0, 0.6	3.78	6.10	5.34	5.31
0.6, 1.2	4.26	6.06	5.18	5.22
1.2, 1.8	4.00	10.37	8.37	5.24

Table 4.12: Single differential cross section as a function of $\eta(D^*)$. The cross section is given in nb and the uncertainties are given in percents.

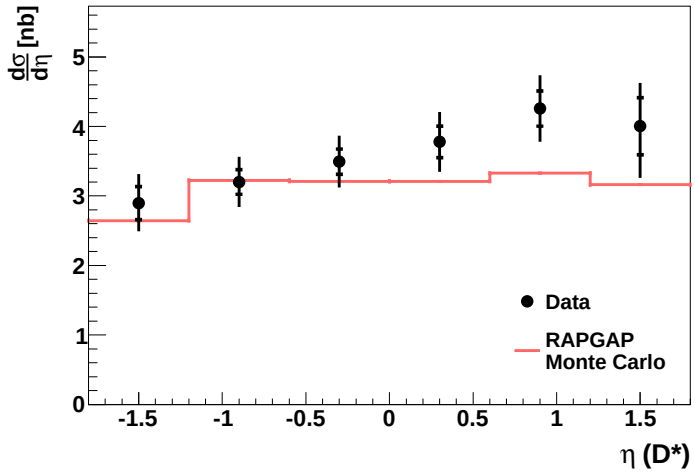

Figure 4.21: Single differential cross section as a function $\eta(D*)$. The black dots represent the experimental cross section and the red line is the theoretical cross section. The vertical error bars represent the total uncertainty on the measurement and the inner bars represent the statistical uncertainty.

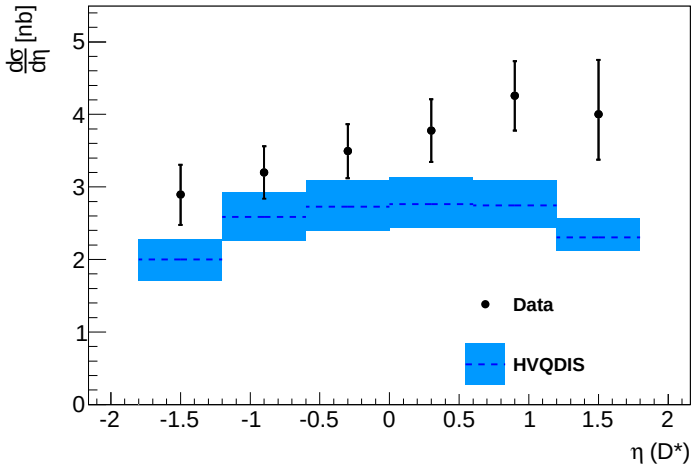

Figure 4.22: Single differential cross section as a function $\eta(D*)$. The black dots represent the experimental cross section and the blue dashed line is the theoretical cross section. The vertical error bars represent the total uncertainty on the measurement and the shaded area represents the total theoretical uncertainty.

4.3.3. Double Differential Cross Sections

Two sets of double differential cross sections are shown: the cross section as a function of the D^* kinematics p_T and η in Figure 4.24 (compared to the leading order Monte Carlo prediction) and in Figure 4.25 (compared to the next-to-leading order calculation), and the cross section as a function of Q^2 and y in Figure 4.26 (compared to the leading order Monte Carlo prediction) and in Figure 4.27 (compared to the next-to-leading order calculation).

The first set of cross sections was determined in order to investigate if the undershooting of the data in the forward direction depends on the p_T of the D^*. The results are shown in Figure 4.24 and in Figure 4.25. When comparing to the leading order prediction, no significant excess is observed, though the prediction undershoots the data points in the higher p_T region.

The second set of cross sections was determined in order to allow the extraction of the charm contribution, $F_2^{c\bar{c}}$, to the proton structure function F_2. For this purpose, the variables Q^2 and y were chosen instead of Q^2 and x, the distribution being more uniform in $Q^2 - y$ than in $Q^2 - x$, as it can be seen in Figure 4.23. The agreement between data and the Monte Carlo prediction is good, with no significant deviations.

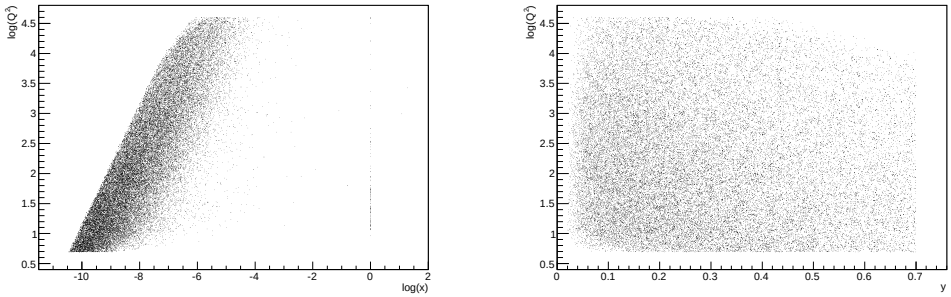

Figure 4.23: Phase space coverage within the visibility cuts as a function of Q^2 and x (left) and as a function of Q^2 and y (right).

p_T range [GeV^2]	η range	$\frac{d\sigma}{dp_T d\eta}$ ($\frac{nb}{GeV}$)	δ_{stat} (%)	δ^+_{syst} (%)	δ^-_{syst} (%)
1.25, 2.0	-1.8, -0.6	1.55	10.17	5.89	6.06
	-0.6, 0.6	1.71	13.50	5.86	5.85
	0.6, 1.8	2.06	12.23	6.47	5.93
2.0, 2.5	-1.8, -0.6	1.06	11.74	5.75	5.68
	-0.6, 0.6	1.14	10.79	5.44	5.34
	0.6, 1.8	1.41	12.11	5.91	5.26
2.5, 3.5	-1.8, -0.6	0.62	7.84	5.92	6.29
	-0.6, 0.6	0.85	6.88	5.58	5.68
	0.6, 1.8	0.86	8.45	5.81	5.51
3.5, 5.0	-1.8, 0.6	0.24	8.86	7.00	8.66
	-0.6, 0.6	0.36	6.57	6.22	7.13
	0.6, 1.8	0.38	10.18	6.33	7.02
5.0, 15.0	-1.8, -0.6	0.012	13.98	8.29	12.42
	-0.6, 0.6	0.028	9.27	7.15	9.91
	0.6, 1.8	0.030	11.86	7.06	9.50

Table 4.13: Cross sections as a function of $p_T(D^*)$ and $\eta(D^*)$. The cross section is given in nb/GeV and the uncertainties are given in percents.

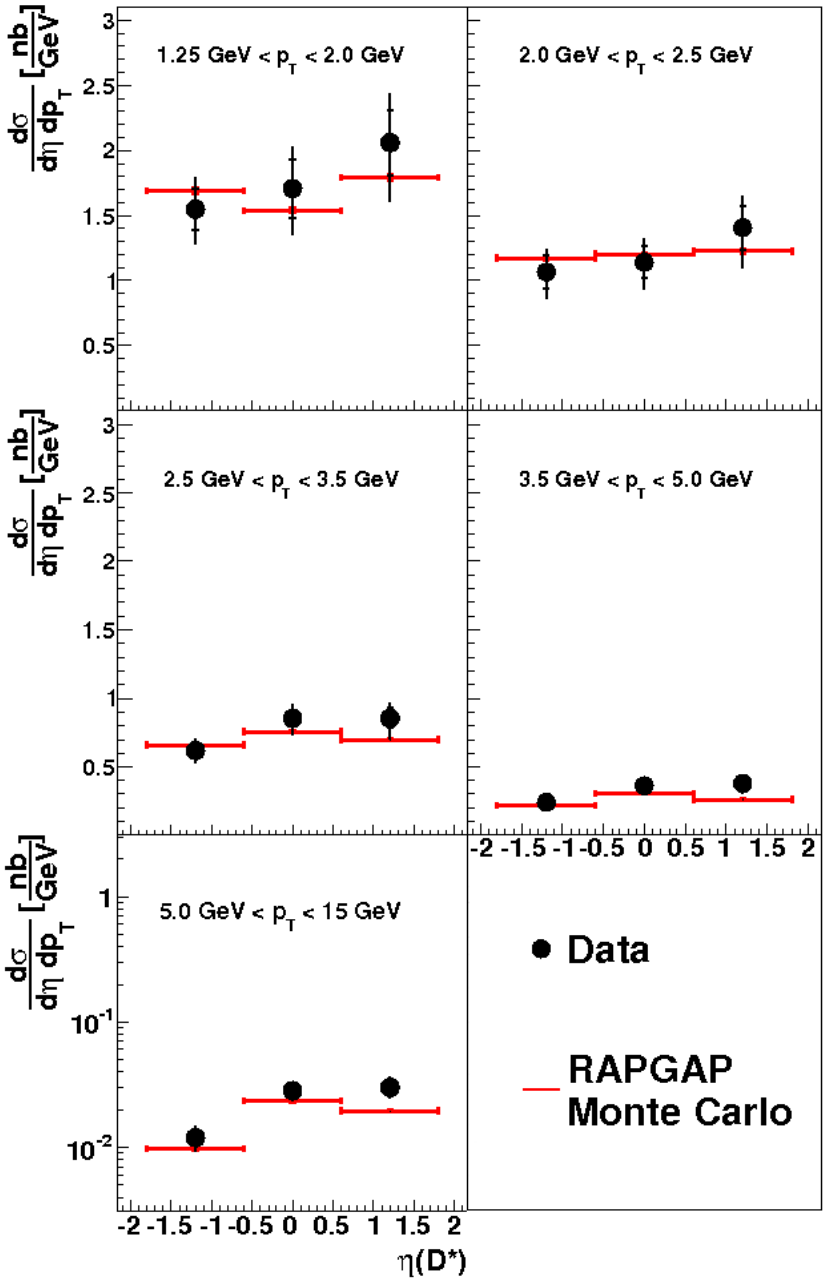

Figure 4.24: Double differential cross sections in $p_T - \eta$. The black dots represent the experimental cross section and the red line is the theoretical cross section. The vertical error bars represent the total uncertainty on the measurement and the inner bars represent the statistical uncertainty.

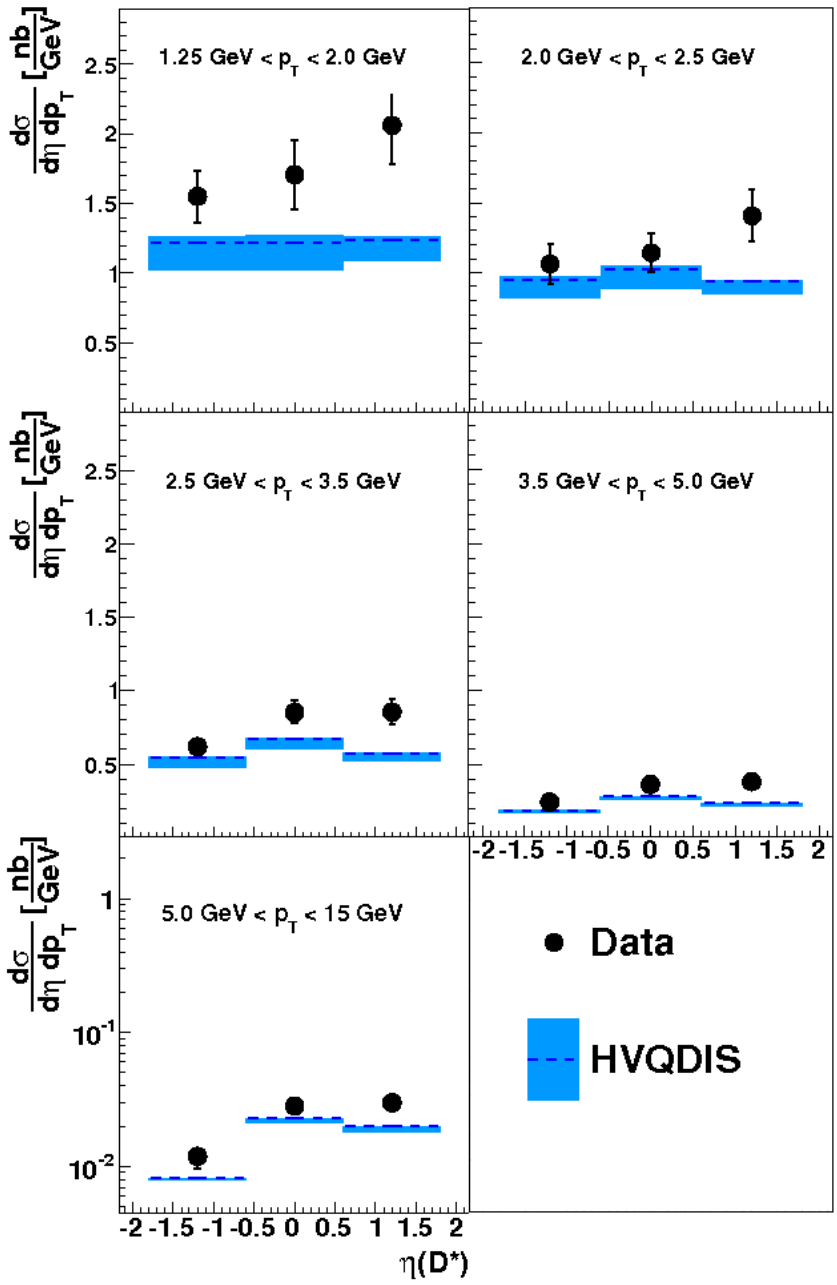

Figure 4.25: Double differential cross sections in $p_T - \eta$. The black dots represent the experimental cross section and the blue dashed line is the theoretical cross section. The vertical error bars represent the total uncertainty on the measurement and the shaded area represents the theoretical uncertainty.

Q^2 range [GeV^2]	y range	$\frac{d\sigma}{dQ^2dy}$ ($\frac{nb}{GeV^2}$)	δ_{stat} (%)	δ^+_{syst} (%)	δ^-_{syst} (%)
2.0, 4.22	0.02, 0.1	6.71	9.08	6.46	5.93
	0.1, 0.2	5.39	6.72	7.89	5.54
	0.2, 0.4	3.00	12.14	10.26	5.46
	0.4, 0.7	1.58	14.58	9.22	5.45
4.22, 10.0	0.02, 0.1	2.51	8.31	6.04	5.78
	0.1, 0.2	1.83	11.82	5.31	5.41
	0.2, 0.4	1.19	15.62	5.19	5.27
	0.4, 0.7	0.403	15.32	5.39	5.40
10.0, 17.8	0.02, 0.1	1.19	10.12	5.99	5.67
	0.1, 0.25	0.619	10.23	5.36	5.46
	0.25, 0.7	0.226	10.79	5.26	5.33
17.8, 31.6	0.02, 0.15	0.318	10.53	5.54	5.50
	0.15, 0.7	0.105	9.57	5.25	5.31
31.6, 100.0	0.02, 0.15	0.070	13.17	5.52	5.51
	0.15, 0.7	0.028	13.95	5.24	5.31

Table 4.14: Cross Sections as a function of Q^2 and y. The cross section is given in nb/GeV^2 and the uncertainties are given in percents.

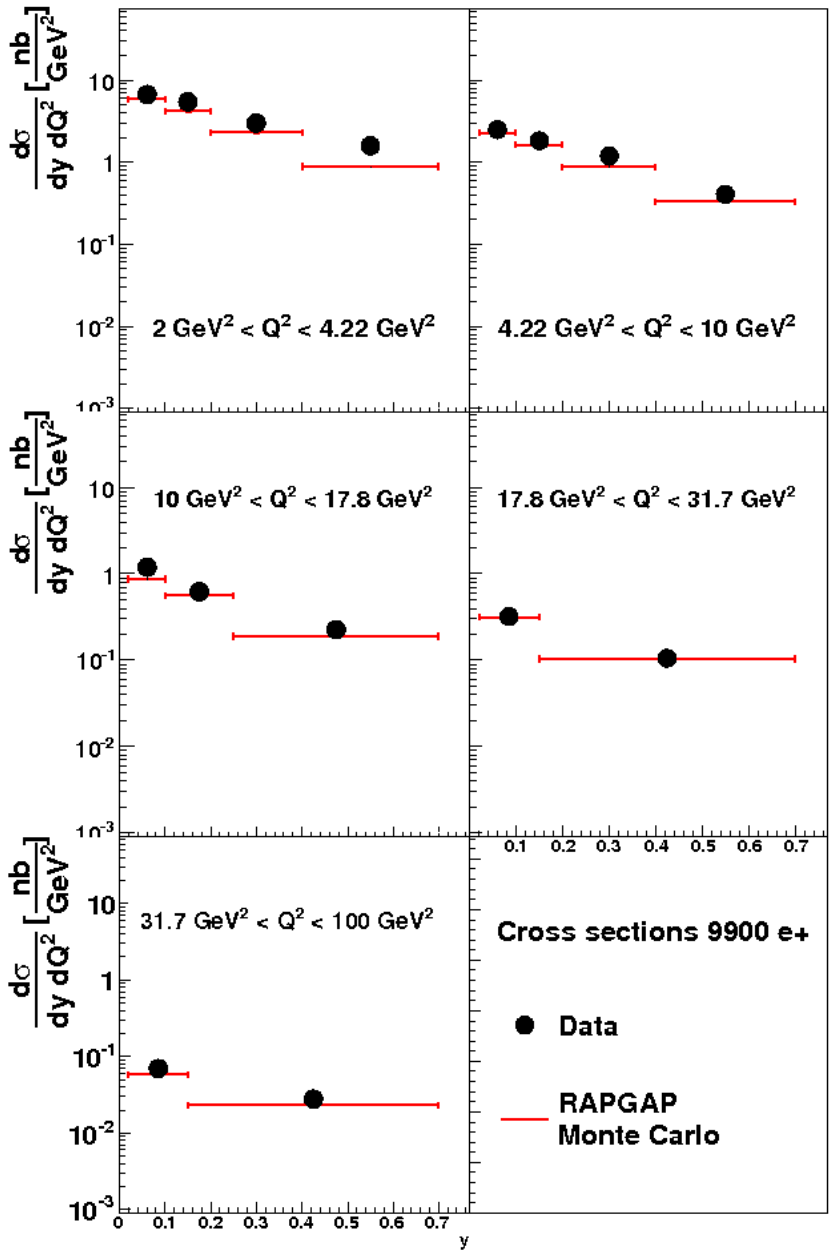

Figure 4.26: Double differential cross sections in $Q^2 - y$. The black dots represent the experimental cross section and the red line is the theoretical cross section. The vertical error bars represent the total uncertainty on the measurement and the inner bars represent the statistical uncertainty.

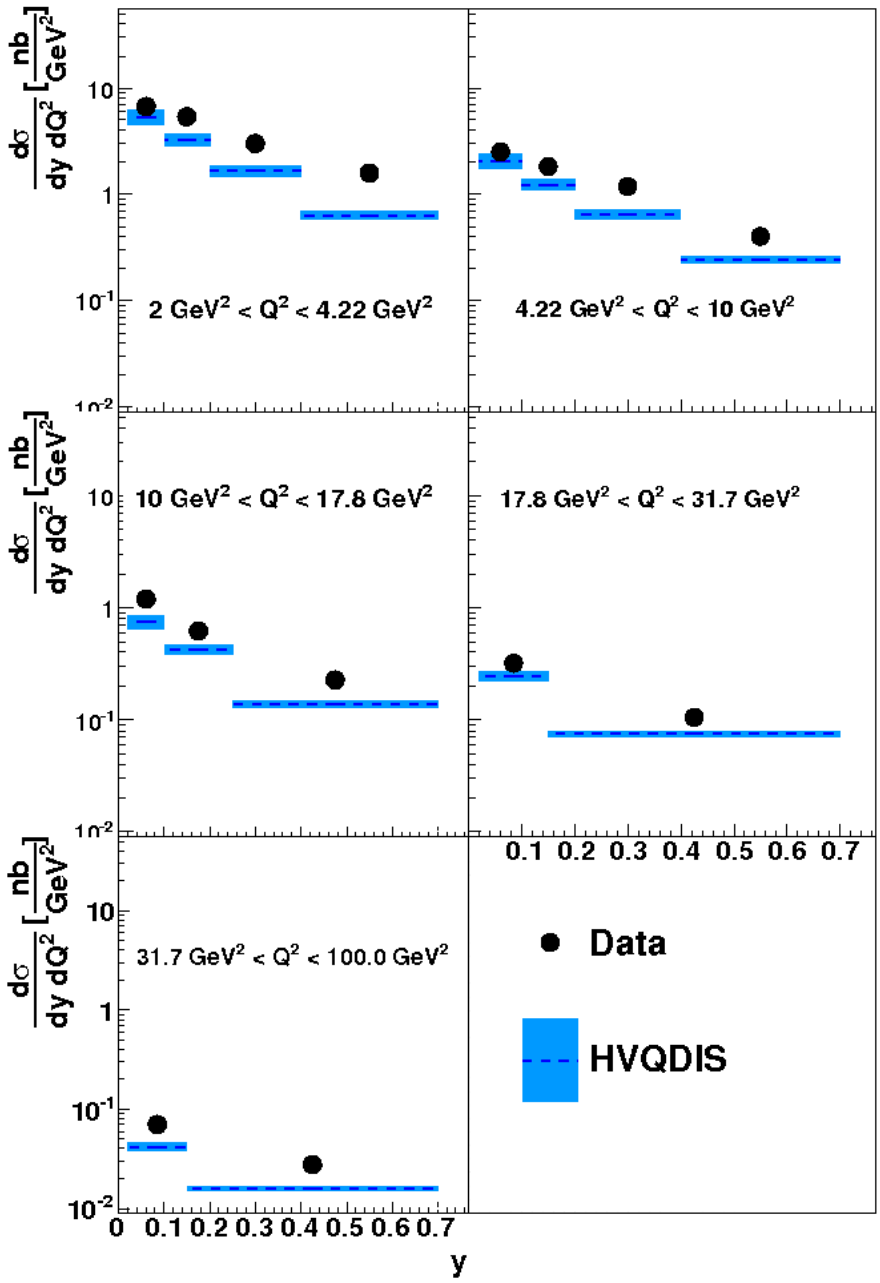

Figure 4.27: Double differential cross sections in $Q^2 - y$. The black dots represent the experimental cross section and the blue dashed line is the theoretical cross section. The vertical error bars represent the total uncertainty on the measurement and the shaded area represents thetheoretical uncertainty.

4.4. Comparison with Other Measurements

The analysis was previously performed on the same data set, but in a phase space restricted in y and D^* observables:

Observable	Range
Q^2	2.0, 100.0 GeV^2
y	0.05, 0.7
$p_T(D^*)$	> 1.5 GeV
$\eta(D^*)$	-1.5, 1.5

Table 4.15: The phase space of the analysis published in [A$^+$07].

The analysis was repeated in this phase space, using the Gauss function for fitting the signal. The total cross section in this phase space is found to be 7.03 $\pm$ 0.19 nb with this analysis, whereas the published cross section is 6.99 $\pm$ 0.20 nb. Only the statistical uncertainty was computed. The cross sections as a function of Q^2, x, $p_T(D^*)$ and $\eta(D^*)$ were also compared to the published values. Agreement is reached within statistical uncertainty in the differential distributions. Shown are the single differential cross sections as a function of $p_T(D^*)$ in Figure 4.28, as a function of $\eta(D^*)$ in Figure 4.29 and as a function of Q^2 in Figure 4.30.

The most recent analysis of the D^* production in DIS was published in 2011 [A$^+$11] and it was performed on a different data set with an increase of one order of magnitude in statistics, but on a phase space restricted in Q^2 to the range 5-100 GeV^2. The signal was fitted with a Crystal Ball function and the total cross section obtained in this phase space is found to be 6.00 $\pm$ 0.20 nb, whereas the published cross section for the same phase space is 6.44 $\pm$ 0.09 nb. Agreement is reached within statistical uncertainty in the differential distributions. Shown are the single differential cross sections as a function of $p_T(D^*)$ in Figure 4.31, as a function of $\eta(D^*)$ in Figure 4.32 and as a function of Q^2 in Figure 4.33.

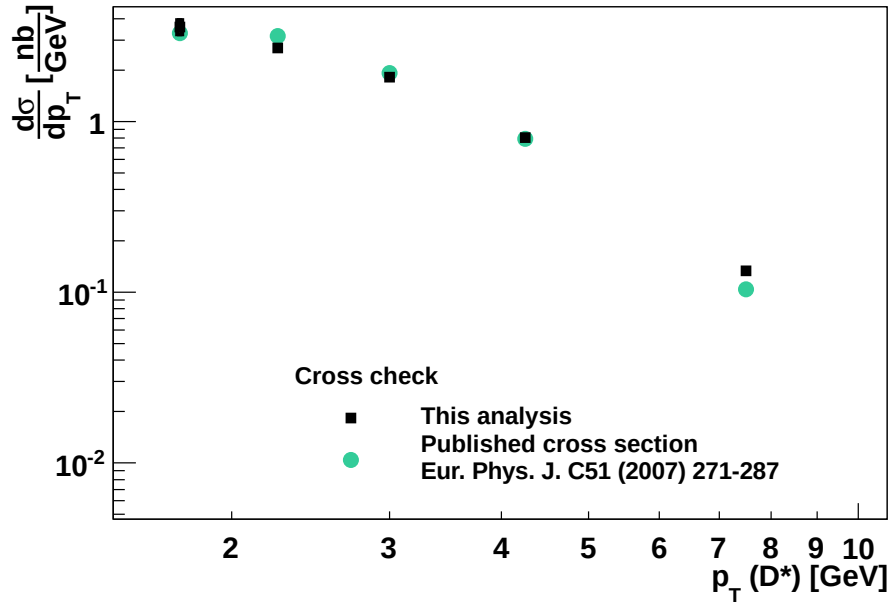

Figure 4.28: Cross section as a function of $p_T(D^*)$. Black squares are the values obtained with this analysis, green points are the values published. Vertical error bars represent the statistical uncertainty. Agreement is achieved within statistical uncertainty.

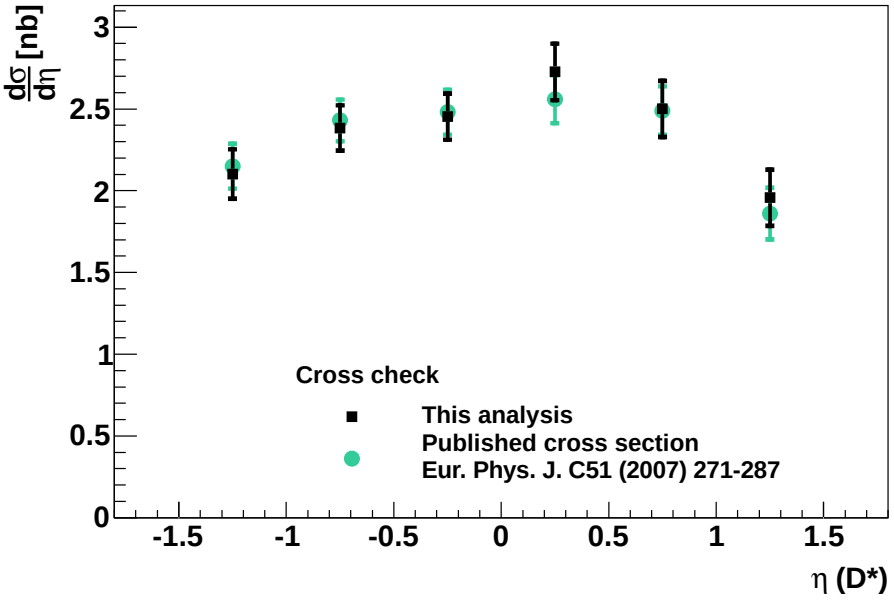

Figure 4.29: Cross section as a function of $\eta(D^*)$. Black squares are the values obtained with this analysis, green points are the values published. Vertical error bars represent the statistical uncertainty. Agreement is achieved within statistical uncertainty.

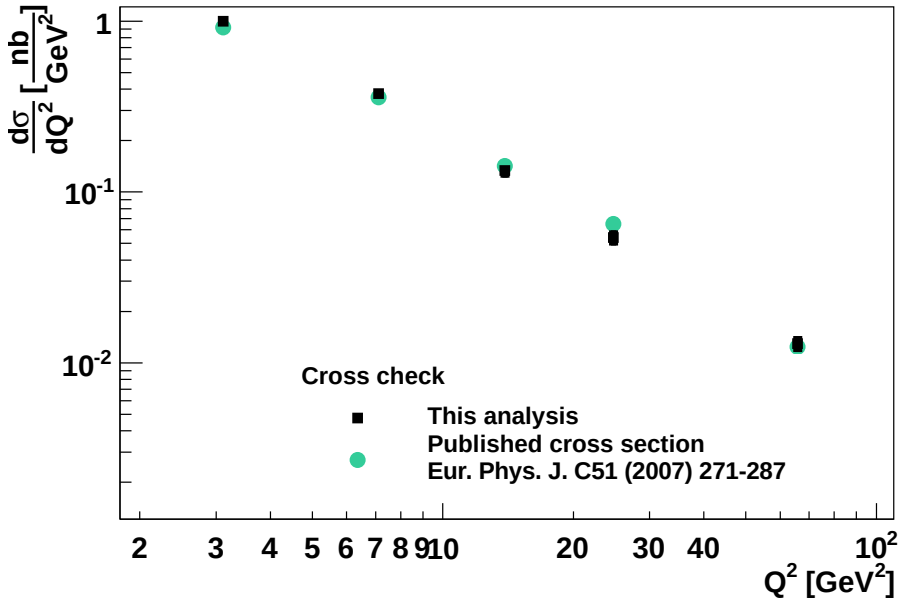

Figure 4.30: Cross section as a function of Q_e^2. Black squares are the values obtained with this analysis, green points are the values published. Vertical error bars represent the statistical uncertainty. Agreement is achieved within statistical uncertainty.

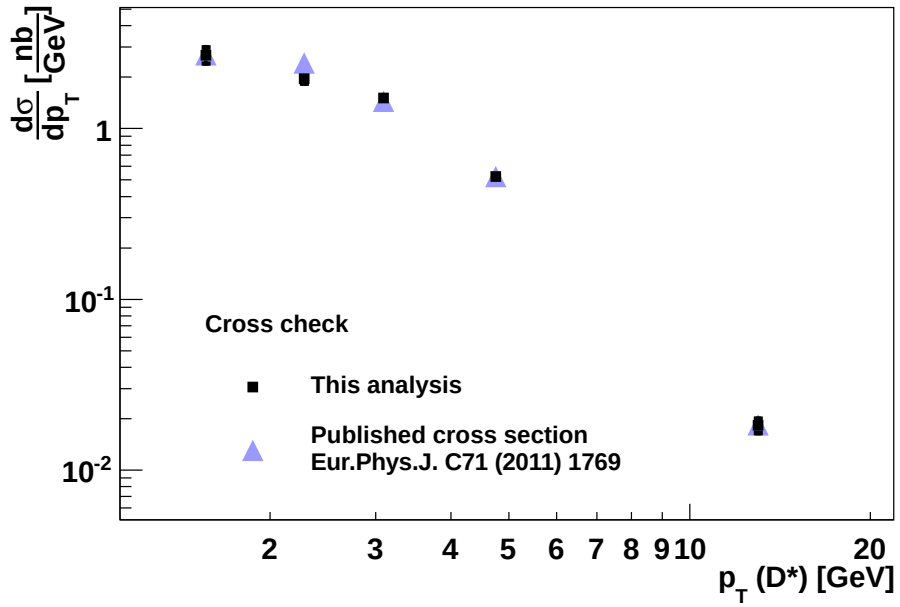

Figure 4.31: Cross section as a function of $p_T(D^*)$. Black squares are the values obtained with this analysis, blue triangles are the values published. Vertical error bars represent the statistical uncertainty. Agreement is achieved within statistical uncertainty.

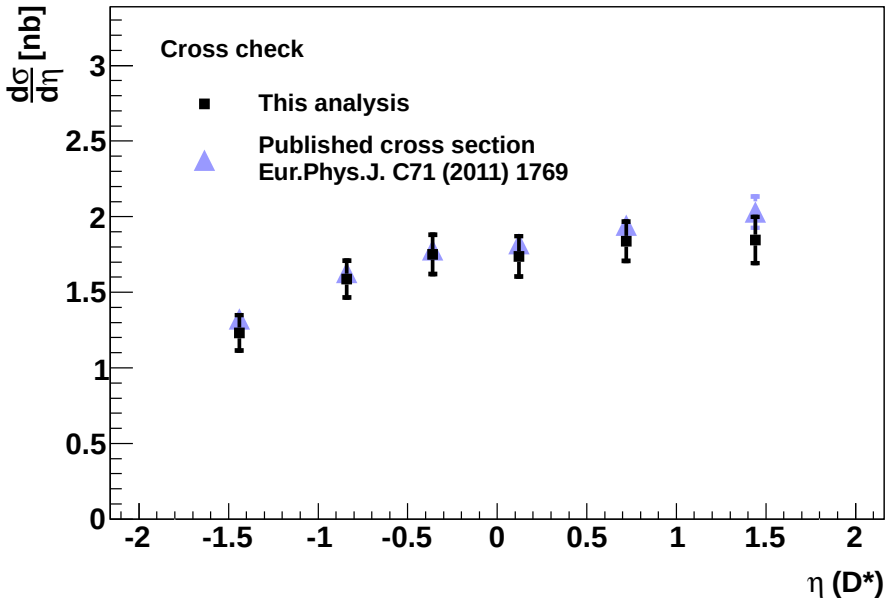

Figure 4.32: Cross section as a function of $\eta(D^*)$. Black squares are the values obtained with this analysis, blue triangles are the values published. Vertical error bars represent the statistical uncertainty. Agreement is achieved within statistical uncertainty.

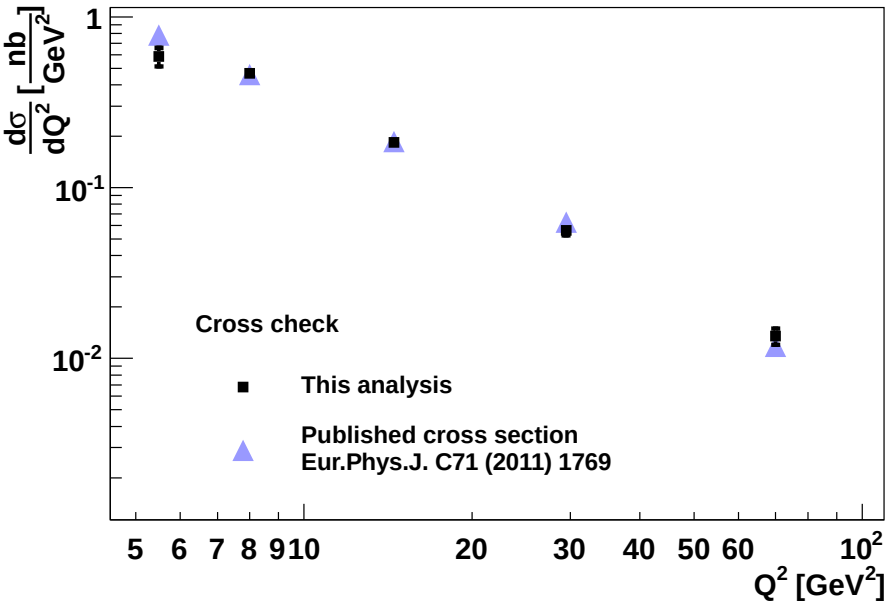

Figure 4.33: Cross section as a function of Q_e^2. Black squares are the values obtained with this analysis, blue triangles are the values published. Vertical error bars represent the statistical uncertainty. Agreement is achieved within statistical uncertainty.

Conclusions

The cross section of the D^* production in ep collisions in deep inelastic scattering at a center of mass energy $\sqrt{s} = 318$ GeV is measured in the kinematic region of the photon virtuality $2 < Q^2 < 100$ GeV^2 and inelasticity $0.02 < y < 0.7$.

This measurement is based on a subset of the HERA 1 data taking period corresponding to an integrated luminosity of 47.66 pb^{-1}. In total, 3493 ± 97 events are reconstructed in the phase space defined by the photon virtuality Q^2, inelasticity y and the D^* meson kinematics, transverse momentum $p_T > 1.25$ GeV and psudorapidity $|\eta(D^*)| < 1.8$. The number of reconstructed events in data has increased by approximately 30% with respect to the previous measurement [A$^+$07] through extensions of the phase space in inelasticity y and the kinematics of the D^* meson, p_T and η. The measurement covers about 60% of the total phase space of the charm production.

For the reconstruction of DIS events the scattered electron is detected in the SpaCal calorimeter, located in the backward region. The D^* mesons are reconstructed in the decay channel $D^{*\pm} \to D^0\pi^{\pm}_{\text{slow}} \to (K^{\mp}\pi^{\pm})\,\pi^{\pm}_{\text{slow}}$. The tracks of the charged decay particles, measured with the central tracking detector, are used for the reconstruction of the (D^*) meson. The calorimeter information is used for the selection of good quality DIS events. Improved offline reconstruction, smaller uncertainties in the electromagnetic energy scale and in the tracking had as a result a reduction in the systematic uncertainties.

Single and double differential cross sections have been measured. These are compared to a leading order prediction in quantum chromodynamics and an NLO calculation. The LO prediction is given by the Monte Carlo simulation RapGap. The cross sections are well described by the LO prediction both in shape and normalisation, proving a good detector knowledge. The NLO calculation HVQDIS provides a reasonable shape description of the cross sections, though the normalisation is lower than expected from the previous measurements. The results obtained were compared to two previous measurements, the first one [A$^+$11] having a narrower Q^2 range, and the second one [A$^+$07] having the same Q^2 range as the analysis in this work, but more restricted ranges in inelasticity y and in the D^* meson kinematics. Agreement with these two measurements was found within statistical uncertainty.

Performing the analysis in the extended phase space was possible due to the good knowledge of the detector. For the first time, it gives access to the region defined by high x, low Q^2 and low $p_T(D^*)$. The good description of the

cross sections in the low Q^2 region demonstrates the validity of the leading order perturbative QCD calculations for the charm production in this region.

Acknowledgements

The work presented in this thesis was funded by the Helmholtz Association in the framework of the Young Investigator Group VH-NG-401 'Physics of gluons and heavy quarks from HERA to the LHC', led by Dr. Katerina Lipka. For the duration of the doctoral studies, I was on leave from the National Institute for Physics and Nuclear Engineering Horia Hulubei in Măgurele, Romania.

I am grateful to Dr. Katerina Lipka for supervising my work, offering suggestions and correcting my thesis. She offered me the unique chance to work in a very motivating environment and trusted me to develop beyond my expectations. Many thanks go to PD Dr. Karin Daum for spending countless hours explaining me particle physics and trying to bring me on the right path. Also, I thank Prof. Robert Klanner for his patience in correcting my thesis and offering useful suggestions for improving its quality.

There are many people who helped me in many ways during the time of my Ph.D. and I am certain that, if I start writing all their names, I will forget involuntarily some of them. But it's worth trying to remember my office colleagues - Maria, Martin, Ringaile, Krzysztof, Jan, Sebastian, Andrea, people from the H1 Heavy Flavour Working Group - Katja, Eva, Florian, Michel, Mira, Andreas, other postdocs and Ph.D. students from H1 and not only - Hayk, Nastja, Richard, Ivan, Carmen, Nicoleta, Madalina, Roxana, Angela, Roman, Michael, Dave... And my friends from Hamburg and elsewhere - Mara, Sorina, Roxana and Keshav, Ella, Nikolas, Renata, Tobias, Mottakin, Sasha, Anca, Amina... I've learned many things from you - physics (and not just particle physics), computing, German, Spanish, spotting bugs in the code just by looking at a plot, riding a bike, enjoying different kinds of food and music, baking cakes, protecting spiders, playing with children and the list is far from ending. I've been lucky to be your colleague and friend and the time spent in Hamburg is unforgettable because of you.

I am very grateful to Călin Alexa, for offering me the chance to work in this field, for his patience and for his constant support.

Sunt recunoscătoare familiei mele pentru sprijinul constant şi necondiţionat pe care mi l-au asigurat, pentru răbdarea lor infinită şi pentru că au fost şi sunt mereu alături de mine. De asemenea, îi mulţumesc fratelui meu ca nu m-a lăsat să pierd legătura cu ceea ce înseamnă 'acasă'.

Acasă la Tina şi Dan am fost mereu primită ca un membru al familiei. Vă mulţumesc!

Alex, îţi mulţumesc pentru răbdarea din serile cu conexiune slabă la internet, pentru nenumăratele călătorii la Hamburg, pentru corecturile la teză şi pentru toate lucrurile frumoase care le-ai făcut să se întâmple.

Erklärung

Hiermit erkläre ich, Monica Dobre, die vorliegende Arbeit selbstständig verfasst und nur die angegebenen Quellen als Hilfsmittel verwendet zu haben. Desweiteren erkläre ich mich mit dem Verleih und der Veröffentlichung der Arbeit einverstanden.

Hamburg, November 20, 2012

Bibliography

[A+93] B. Andrieu et al., *The H1 liquid argon calorimeter system*, Nucl. Instrum. Meth. **A336** (1993), 460–498.

[A+97a] I. Abt et al., *The H1 detector at HERA*, Nucl. Instrum. Meth. **A386** (1997), 310–347.

[A+97b] ———, *The Tracking, calorimeter and muon detectors of the H1 experiment at HERA* , Nucl. Instrum. Meth. **A386** (1997), 348–396.

[A+97c] R. D. Appuhn et al., *The H1 lead/scintillating-fibre calorimeter*, Nucl. Instrum. Meth. **A386** (1997), 397–408.

[A+07] A. Aktas et al., *Production of $D^{*\pm}$ Mesons with Dijets in Deep-Inelastic Scattering at HERA*, Eur.Phys.J. **C51** (2007), 271–287.

[A+09] F.D. Aaron et al., *Study of Charm Fragmentation into $D^{*\pm}$ Mesons in Deep-Inelastic Scattering at HERA*, Eur.Phys.J. **C59** (2009), 589–606, 33 pages, submitted to EPJC.

[A+10] ———, *Combined Measurement and QCD Analysis of the Inclusive $e^{\pm}p$ Scattering Cross Sections at HERA*, JHEP **1001** (2010), 109.

[A+11] ———, *Measurement of $D^{*\pm}$ Meson Production and Determination of F_2^{ccbar} at low Q2 in Deep-Inelastic Scattering at HERA*, Eur.Phys.J. **C71** (2011), 1769.

[AAA+09] F.D. Aaron, C. Alexa, V. Andreev, B. Antunovic, S. Aplin, et al., *Measurement of the Inclusive ep Scattering Cross Section at Low Q^2 and x at HERA*, Eur.Phys.J. **C63** (2009), 625–678.

[AC99] H. Abramowicz and A. Caldwell, *HERA collider physics*, Rev.Mod.Phys. **71** (1999), 1275–1410.

[AP77] G. Altarelli and G. Parisi, *Asymptotic Freedom in Parton Language*, Nucl.Phys. **B126** (1977), 298.

[BB95] Ursula Bassler and Gregorio Bernardi, *On the kinematic reconstruction of deep inelastic scattering at HERA: The Sigma method*, Nucl.Instrum.Meth. **A361** (1995), 197–208.

[BBD+79] A. Bodek, Martin Breidenbach, D.L. Dubin, J.E. Elias, Jerome I. Friedman, et al., *Experimental Studies of the Neutron and Proton Electromagnetic Structure Functions*, Phys.Rev. **D20** (1979), 1471–1552.

[BBM+87] R. Brun, F. Bruyant, M. Maire, A.C. McPherson, and P. Zanarini, *GEANT3*.

[BCD+69] E. D. Bloom, D. H. Coward, H. DeStaebler, J. Drees, G. Miller, L. W. Mo, R. E. Taylor, M. Breidenbach, J. I. Friedman, G. C. Hartmann, and H. W. Kendall, *High-Energy Inelastic $e-p$ Scattering at 6^o and 10^o*, Phys. Rev. Lett. **23** (1969), 930–934.

[Beh05] O. Behnke, *Tracking Efficiency studies with K_s^0*, 2005, H1 Internal Communication.

[BFK+69] M. Breidenbach, J. I. Friedman, H. W. Kendall, E. D. Bloom, D. H. Coward, H. DeStaebler, J. Drees, L. W. Mo, and R. E. Taylor, *Observed Behavior of Highly Inelastic Electron-Proton Scattering*, Phys. Rev. Lett. **23** (1969), 935–939.

[BH34] H. Bethe and W. Heitler, *On the stopping of fast particles and on the creation of positive electrons*, Proc. Roy. Soc. Lond. **A146** (1934), 83–112.

[BL78] I.I. Balitsky and L.N. Lipatov, *The Pomeranchuk Singularity in Quantum Chromodynamics*, Sov.J.Nucl.Phys. **28** (1978), 822–829.

[Blo] V. Blobel, *Fast track-fit algorithm based on broken lines*, available at https://www.desy.de/ blobel/brline.html.

[Boe07] M. O. Boenig, *Messung des D^*-Meson-Produktionsquerschnitts in tieinelastischer Streuung mit dem H1-Experiment.*, Ph.D. thesis, Universität Dortmund, Germany, 2007.

[Bow81] M.G. Bowler, *e+ e- Production of Heavy Quarks in the String Model*, Z.Phys. **C11** (1981), 169.

[BR97] R. Brun and F. Rademakers, *ROOT: An object oriented data analysis framework*, Nucl.Instrum.Meth. **A389** (1997), 81–86.

[Bri10] M. Brinkmann, *Measurement of the $D^{*\pm}$ Meson Production Cross Section and $F_2^{c\bar{c}}$ at High Q^2 in ep Scattering at HERA*, Ph.D. thesis, Universität Hamburg, 2010.

[CFM90a] S. Catani, F. Fiorani, and G. Marchesini, *QCD Coherence in Initial State Radiation*, Phys.Lett. **B234** (1990), 339.

[CFM90b] ———, *Small x Behavior of Initial State Radiation in Perturbative QCD*, Nucl.Phys. **B336** (1990), 18.

[CG69] Jr. Callan, Curtis G. and David J. Gross, *High-energy electroproduction and the constitution of the electric current*, Phys.Rev.Lett. **22** (1969), 156–159.

[Cia88] Marcello Ciafaloni, *Coherence Effects in Initial Jets at Small q**2 / s*, Nucl.Phys. **B296** (1988), 49.

[Col] H1 Collaboration, *Technical proposal for the upgrade of the backward region of the H1 detector, DESY internal report PRC-93/02.*

[Col08] ———, *H1REC documentation webpage*, available at https://www-h1.desy.de/icas/imanuals/h1rec/h1rec9/h1rec.html, 2008.

[Dau10] K. Daum, *Track efficiency studies*, 2010, Internal Communication.

[DCS04] R. Devenish and A. Cooper-Sarkar, *Deep inelastic scattering*, 2004.

[Dok77] Yuri L. Dokshitzer, *Calculation of the Structure Functions for Deep Inelastic Scattering and e+ e- Annihilation by Perturbation Theory in Quantum Chromodynamics.*, Sov.Phys.JETP **46** (1977), 641–653.

[eaHC] S. Aid et. al [H1 Collaboration], *Proceedings of the 28th International Conference on High Energy Physics, ICHEP'96, Warsaw, Poland, p. 17026.*

[eaHSG] R.D. Appuhn et al. [H1 SpaCal Group], *DESY Red Report 96-013.*

[Eck02] D. Eckstein, *Messung der Longitudinalen Strukturfunktion $F_L(x, Q^2)$ mit dem HERA Experiment H1*, Ph.D. thesis, Berlin, 2002.

[Erd96] W. Erdmann, *Untersuchung der Photoproduktion von D∗-Mesonen am ep-Speicherring HERA*, Ph.D. thesis, Eidgenössischen Technischen Hochschule Zürich, 1996.

[F+77] G. J. Feldman et al., *Observation of the Decay D*+ → D0 pi+*, Phys. Rev. Lett. **38** (1977), 1313.

[Fav] L. Favart, *H1 Internal Note H1-06/94-366.*

[Fel10] J. Feltesse, *Introduction to Parton Distribution Functions*, Scholarpedia **5** (2010), no. 11, page 10160.

[Fey72] R.P. Feynman, *Photon-hadron interactions*, Benjamin, New York, 1972.

[G+78] P. Granet et al., *Inclusive Production Cross-Sections of Resonances in 32-GeV/c K+ p Interactions*, Nucl.Phys. **B140** (1978), 389.

[Gai82] J. E. Gaiser, *Charmonium Spectroscopy From Radiative Decays of the J/Ψ and Ψ'^**, Ph.D. thesis, Stanford University, 1982.

[GL72] V.N. Gribov and L.N. Lipatov, *Deep inelastic e p scattering in perturbation theory*, Sov.J.Nucl.Phys. **15** (1972), 438–450.

[Gla98] A. A. Glazov, *Measurement of the Proton Structure Functions $F_2(x, Q^2)$ and $F_L(x, Q^2)$ with the H1 Detector at HERA*, Ph.D. thesis, Humboldt-Universität Berlin, 1998.

[Gre64] O.W. Greenberg, *Spin and Unitary Spin Independence in a Paraquark Model of Baryons and Mesons*, Phys.Rev.Lett. **13** (1964), 598–602.

[H+02] Kaoru Hagiwara et al., *Review of particle physics. Particle Data Group*, Phys.Rev. **D66** (2002), 010001.

[HS95] B.W. Harris and J. Smith, *Heavy quark correlations in deep inelastic electroproduction*, Nucl.Phys. **B452** (1995), 109–160.

[HS98] ———, *Charm quark and D*+- cross-sections in deeply inelastic scattering at HERA*, Phys.Rev. **D57** (1998), 2806–2812.

[Jam] F. James, *MINUIT, Function Minimization and Error Analysis*, Computing and Network Division, CERN Geneva, Switzerland.

[Jun95] Hannes Jung, *Hard diffractive scattering in high-energy e p collisions and the Monte Carlo generator RAPGAP*, Comput.Phys.Commun. **86** (1995), 147–161.

[Jun09] A. W. Jung, *Measurement of the $D^{*\pm}$ Meson Cross Section and Extraction of the Charm Contribution ($F_2^C(x, Q^2)$) to the Proton Structure*

in Deep Inelastic ep Scattering with the H1 Detector at HERA, Ph.D. thesis, Ruprecht-Karls-Universität Heidelberg, 2009.

[KLF77] E.A. Kuraev, L.N. Lipatov, and Victor S. Fadin, *The Pomeranchuk Singularity in Nonabelian Gauge Theories*, Sov.Phys.JETP **45** (1977), 199–204.

[KLP78] V.G. Kartvelishvili, A.K. Likhoded, and V.A. Petrov, *On the Fragmentation Functions of Heavy Quarks Into Hadrons*, Phys.Lett. **B78** (1978), 615.

[Kog10] R. Kogler, *Measurement of Jet Production in Deep Inelastic ep Scattering at HERA*, DESY Thesis, 2010.

[Kog12] ———, *Hadronic Calibration for HERA 1*, 2012, H1 Internal Communication.

[KSM92] A. Kwiatkowski, H. Spiesberger, and H.J. Mohring, *HERACLES: An Event Generator for ep Interactions at HERA Energies Including Radiative Processes: VERSION 1.0*, Comput.Phys.Commun. **69** (1992), 155–172.

[Loh11] E. Lohrmann, *A Summary of Charm Hadron Production Fractions*, [arXiv:hep-ex/1112.3757], 2011.

[Mar95] Giuseppe Marchesini, *QCD coherence in the structure function and associated distributions at small x*, Nucl.Phys. **B445** (1995), 49–80.

[Mey89] J. Meyer, *Guide for the H1 simulation program H1SIM.*, Internal Software-Note 03-11/89, DESY, 1989.

[Mor89] Duncan A. Morris, *HEAVY QUARK FRAGMENTATION FUNCTIONS IN A SIMPLE STRING MODEL*, Nucl.Phys. **B313** (1989), 634.

[N+96] T. Nicholls et al., *Performance of an electromagnetic lead / scintillating fiber calorimeter for the H1 detector*, Nucl. Instrum. Meth. **A374** (1996), 149–156.

[N+10] K. Nakamura et al., *Review of particle physics*, J.Phys.G **G37** (2010), 075021.

[Pet11] A. Petrukhin, *SpaCal Calibration for HERA 1*, 2011, H1 Internal Communication.

[PSSZ83] C. Peterson, D. Schlatter, I. Schmitt, and Peter M. Zerwas, *Scaling Violations in Inclusive e+ e- Annihilation Spectra*, Phys.Rev. **D27** (1983), 105.

[Sch] S. Schmitt, *Correction of detector effects: bin-by-bin and unfolding*, H1 Internal Note H1-IN-633(03/2011).

[Sch96] B. Schwab, *Das Rückwärtsdriftkammersystem des H1-Experiments*, Ph.D. thesis, Heidelberg, 1996.

[Sch04] S. Schmidt, *Messung charminduzierter Zweijetereignisse in tief inelastischer ep-Streuung mit dem H1-Detektor bei HERA*, Ph.D. thesis, Technishe Universität München, 2004.

[Ste99] J. Steinhart, *Die Messung des Totalen $c\bar{c}$-Photoproduktions-Wirkungsquerschnittes durch die Rekonstruktion von Λ_c-Baryonen unter Verwendung der verbesserten dE/dx-Teilchenidentifikation am H1 Experiment bei HERA*, Ph.D. thesis, Universität Hamburg, 1999.

[TKS02] Wu-Ki Tung, Stefan Kretzer, and Carl Schmidt, *Open heavy flavor production in QCD: Conceptual framework and implementation issues*, J.Phys.G **G28** (2002), 983–996.

[TT08] R.S. Thorne and W.K. Tung, *PQCD Formulations with Heavy Quark Masses and Global Analysis*.

[VK05] W. Verkerke and D. Kirkby, *The RooFit Toolkit for Data Modelling*, available at arXiv:physics/0306116, 2005.

[Web00] B.R. Webber, *Fragmentation and hadronization*, Int.J.Mod.Phys. **A15S1** (2000), 577–606.

[Wol] G. Wolf, *HERA physics*, Lectures given at 42nd Scottish Universities Summer School in Physics (SUSSP 93): High Energy Phenomenology (NATO Advanced Study Institute), St. Andrews, Scotland, 1-21 Aug 1993.